Biophysics of naked mole-rat derived lipid bilayers and their complex behaviour

Matthew Davies

Thesis submitted for the degree of
Doctor of Philosophy

School of Engineering
Newcastle University
Newcastle upon Tyne
United Kingdom

March 2022

Abstract

The naked mole-rat (NMR) is an exceptionally long lived rodent, living significantly longer than other similarly sized rodents. In this thesis the lipid component of the NMR cell membrane was assessed to determine the role it plays in this longevity at the molecular/membrane level. Atomic force microscopy reveals that supported lipid bilayers formed from NMR lipids exhibit a high degree of phase separation compared with mouse lipids. This phase behaviour is unique when compared with commercially available lipid extracts derived from other animals. Such phase separation does not provide protection from the damage induced by exposure to amyloid beta, a key player thought to be involved in Alzheimer's disease. Compared with mouse derived supported lipid bilayers there is increased damage. Key compositional differences between the NMR and mouse lipids were identified in cholesterol and sphingomyelin, both of which are linked with lipid bilayer phase separation. Sphingomyelin was focused on further due to its relation with Alzheimer's disease, phase separation and the difference in tail length distributions between the two animals, with NMR having much shorter chain lipids, whereas mouse had more highly asymmetric, longer chain lipids. At the temperature studied, sphingomyelin, at any chain length/asymmetry, was found in the ripple phase, rather than the commonly studied fluid phase. At large tail asymmetries, there was a high degree of variability in the lipid tail conformations, with the tails bending to accommodate the unbalanced lipid shapes. A new technique for quantifying the ripple phase in molecular dynamics simulations was developed utilising a three-body correlation function to measure local structure and unsupervised machine learning. This was able to identify four unique lipid conformations in the ripple phase of the widely simulated DPPC lipid bilayer. This technique has the potential to be applied to more complex systems, like the NMR composition lipids.

Acknowledgements

I would like to thank Daniel Frankel for his supervision, guidance and patience through the project. Ewan st John Smith, Yavuz Kulaberoglu and Paulina Urriola-Munoz for supplying me with naked mole-rat and mouse lipid extracts. Janet Kumita for her expertise and use of the lab and equipment for the ThT assay and for synthesising the naked mole-rat sequence amyloid beta. Nicolas Cenac for performing mass spectroscopy and lipidomic quantification on the brain lipid extracts and processing and assisting me in understanding the resulting data. Mikko Karttunen and Angel Reyes-Figueroa for providing computational resources, and expertise in molecular dynamics, and extensive thoughtful discussion on lipids, their structure and their phase behaviour.

Finally, my family and Ailsa.

Publications arising from this work

Work in this thesis has resulted in the following publications:

1. D. Frankel, M. Davies, B. Bhushan, Y. Kulaberoglu, P. Urriola-Munoz, J. Bertrand-Michel, M. R. Pergande, A. A. Smith, S. Preet, T. J. Park, M. Vendruscolo, K. S. Rankin, S. M. Cologna, J. R. Kumita, N. Cenac, and E. St John Smith (2020). "Cholesterol-rich naked mole-rat brain lipid membranes are susceptible to amyloid beta-induced damage in vitro". *Aging* 12.21, pp. 22266–22290. DOI: 10.18632/aging.202138

2. M. Davies, A. Reyes-Figueroa, A. A. Gurtovenko, D. Frankel, and M. Karttunen (2022). "Elucidating lipid conformations in the ripple phase: Machine learning reveals four lipid populations". *Biophysical Journal*. DOI: 10.1016/j.bpj.2022.11.024

Contents

List of Figures

List of Tables

List of Abbreviations

Aβ	amyloid beta.
AD	Alzheimer's disease.
AFM	atomic force microscopy.
APP	amyloid precursor protein.
DBSCAN	density-based spatial clustering of applications with noise.
DOPC	dioleoylphosphatidylcholine.
DPPC	dipalmitoylphosphatidylcholine.
FAD	familial Alzheimer's disease.
g_3	radial-angular, three particle correlation function.
GMM	Gaussian mixture modelling.
L_d	fluid-like phase.
L_o	gel-like phase.
LPP	lipid peroxidation products.
MD	molecular dynamics.
MSD	mean squared displacements.
NMR	naked mole-rat.
P'_β	ripple phase.
PCA	principle component analysis.

RDF	radial distribution function.
SAD	sporadic Alzheimer's disease.
S_{CD}	deuterium order parameter.
SLB	supported lipid bilayer.
SM	sphingomyelin.
SSIM	structural similarity index metric.
t-SNE	t-distributed stochastic neighbour embedding.
ThT	thioflavin T.

Chapter 1. Introduction

The naked mole-rat, *Hetrocephalus glaber*, does not succumb to neurodegenerative diseases, such as Alzheimer's disease, despite having a maximum lifespan of greater than 30 years (the similar sized mouse has a maximum life an order of magnitude lower). Thus, the question arises, how does an animal that lives so long, resist neurodegenerative diseases associated with ageing? The molecular basis of Alzheimer's disease in humans is poorly understood with a multitude of drugs, based on the current state of molecular knowledge, failing at the clinical trials stage. It is in this context that looking at an animal which is resistant to Alzheimer's disease can help us develop a better understanding of the disease in humans.

1.1 Aims and Objectives

The main aim of this thesis is to explore the molecular interactions between the key players in Alzheimer's disease, in the Alzheimer's disease resistant naked mole-rat. Focus is on the role of brain lipids and their interactions with amyloid beta peptide, a molecule thought to play a key role in the development of Alzheimer's disease. A soft matter approach will be used to determine any unique properties of these molecular components that might explain the disease resistance of the naked mole-rat.

The research objectives are as follows:

1. To prepare and validate supported lipid bilayer comprising of naked mole-rat total lipid extract on mica for atomic force microscopy experiments.

2. To examine the composition, phase behaviour, and morphology of supported lipid bilayers derived from the total lipid extract of naked mole-rats. Comparison will be made with the total lipid extract derived from mouse.

3. To quantify the mechanical properties of brain derived lipids using atomic force microscopy based nanoindentation.

4. To examine the interactions between amyloid beta and brain derived lipids using atomic force microscopy.

5. To perform molecular dynamics simulations to examine lipid bilayers composed of key naked mole-rat lipids.

6. To quantify the effect of various lipid alterations on the properties of bilayers comprising of key naked mole-rat lipids.

7. To develop a workflow to analyse and extract conformational details about the phase behaviour of molecular dynamics simulations of lipid bilayers.

1.2 Literature Review

1.2.1 What is neurodegenerative disease?

Neurodegenerative disease covers a range of diseases effecting the neurons in the brain, causing neuronal degeneration and death (Przedborski, Vila, and Jackson-Lewis 2003). It is an umbrella term that covers a range of diseases but the most influential category within this are dementias, the most common of which is Alzheimer's disease (Mayeux and Stern 2012). There are currently approximately 6 million sufferers in the United States of America according to multiple estimates (Mayeux and Stern 2012; Hebert et al. 2013; Brookmeyer et al. 2018). Alzheimer's disease is characterised by the loss of mental capacities. Often expressing as mild memory impairment initially, it ultimately can lead to complete loss of independence requiring assistance with even basic daily tasks until eventual premature death (Mayeux and Stern 2012). Following a diagnosis of Alzheimer's disease the average life expectancy is estimated at 3.2-6.6 years (Todd et al. 2013); however diagnosis comes later in the disease progression with over 7.5 times as many people living in America with 'preclinical' Alzheimer's disease signs (amyloidosis and/or neurodegeneration) (Brookmeyer et al. 2018) often suffering neurodegeneration for decades before clinical diagnosis (Blennow, Leon, and Zetterberg 2006). Alzheimer's disease and other dementia patients put a large drain on society and healthcare systems, the cost of the final 5 years of life of an Alzheimer's patient is significantly greater than that of heart disease and cancer patients (Kelley et al. 2015).

1.2.2 Ageing and neurodegenerative disease

There are a range of factors which increase the likelihood of Alzheimer's disease: genetics, smoking, traumatic head injury, and weight (both obesity and low body weight) (Mayeux and Stern 2012). However, one of the main factors is age (Mayeux and Stern 2012). While there are genetic cases of early onset cases of Alzheimer's disease, most cases involve aged patients. The number of Alzheimer's patients increases exponentially in people over 65 (Mayeux and Stern 2012). This age dependency is a feature of the second most common neurodegenerative disease, Parkinson's disease (Alves et al. 2008). Age has been suggested as the most consistent risk factor in Alzheimer's and Parkinson's disease (Przedborski, Vila, and Jackson-Lewis 2003). Populations worldwide are ageing (Powell 2010). With the clear trend of heightened neurodegenerative disease risk with age and the ever growing population global, estimates of dementia cases predict a doubling of cases every 20 years. Although not geographically uniform, the developing world is expected to face three times the increase by 2050 (Ferri et al. 2005).

1.2.3 The molecular basis of Alzheimer's disease and the hallmarks of Alzheimer's disease

The hallmarks of Alzheimer's disease, that is the characteristic pathology of an Alzheimer's brain, are plaques and tangles (Blennow, Leon, and Zetterberg 2006). These were seen in the first reported cases at the turn of the 20th century (Möller and Graeber 1998) and have remained a key hallmark of the disease. Plaques, comprising of amyloid beta (Aβ) peptide, are extracellular aggregates whereas tangles are intracellular aggregates comprising of Tau protein (Blennow, Leon, and Zetterberg 2006). The role and nature of harm introduced by plaques and tangles is still undetermined (Wolfe and Cyr 2011; Cowan and Mudher 2013). The lack of understanding of the molecular mechanism of the molecular pathways is attributed to the failure of potential treatments (Castro, Hadziselimovic, and Sanders 2019). The involvement of peptide and protein aggregates in disease is not exclusive to Alzheimer's disease either. The mechanism is shared by the class of protein conformational diseases. This includes neurodegenerative diseases such as Parkinson's disease and Huntington's disease; and also none-neurodegenerative diseases such as type 2 diabetes and cataracts (Chiti and Dobson 2006). It has been suggested that more effective treatment might involve targeting the secondary structures formed along the pathway rather than focusing on the sequence of single molecules (Sivanesam and N. Andersen 2019). This would

indicate that a further understanding of the disease progression would be beneficial to future attempts at treatment development. Another key hallmark of Alzheimer's disease is a greatly increased level of oxidative stress in the brain (Butterfield and Lauderback 2002; Z. Chen and C. Zhong 2014). Although much research focuses on the oxidative damage caused by the classical hallmarks of the Alzheimer's, the plaques and tangle, it has been noted that the onset of oxidation occurs before these (Nunomura et al. 2001).

1.2.4 The amyloid cascade hypothesis

The amyloid cascade hypothesis states simply that Alzheimer's disease pathogenesis and neurodegeneration are a result of the aggregating of the peptide amyloid beta (Aβ) into plaques in the brain. All other signs such as Tau tangles are a result of the plaque formation and increases and decreases to Aβ production and removal in the brain(Selkoe 1991; J. A. Hardy and Higgins 1992; J. Hardy and Selkoe 2002). The key premise is that the root cause of all Alzheimer's disease is the Aβ peptide. It is not a universally accepted hypothesis, with alternatives each suggesting alternative root causes. A key question is raised when considering familial Alzheimer's disease (FAD) compared to sporadic Alzheimer's disease (SAD). The first, FAD, is much earlier onset, and heavily genetically linked. The seconds, SAD, is more common and shows little specific genetic link. When associating Alzheimer's disease pathogenesis with ageing, how to account for FAD given that both it and SAD express identically and are indistinguishable (Lippa et al. 1996). The mitochondria cascade hypothesis places the root cause as mitochondria dysfunction, with age related damage to the mitochondria altering their function acting as the root driving cause of the pathogenesis (Swerdlow and Khan 2004; Swerdlow, Burns, and Khan 2014), a key issue with this is the evidence that FAD is heavily related to point mutation to the amyloid precursor protein (APP) gene, just by the Aβ cleavage point (Goate 2006). The dual pathway hypothesis states there is an unknown factor upstream of both Aβ and Tau, initiating the disease pathogenesis, acting simultaneously on each. It does not disagree with the amyloid cascade hypothesis but merely attempts to explain the high amount of failed drug trials based on amyloid research. This has some weight particularly when some trials have successfully removed Aβ plaques in the brain without stopping the cognitive decline Alzheimer's disease brings (C. Holmes et al. 2008), although this was not a study on primary intervention, using patients with suspected Alzheimer's disease. The vascular hypothesis posits that ineffective clearance of molecules due to inadequate

vasculature is the base cause of Alzheimer's disease (Torre 2004), this relies on evidence that plaques form localised near blood vessels (Kumar-Singh et al. 2005), and that the brain of an Alzheimer's patient has a significantly different vascular arrangement (Fischer, Siddiqi, and Yusufaly 1990). It attempts to explain the oxidation stress before amyloid plaque deposition (Torre 2008). The studies into this however cannot resolve the time ordering; is this a result of plaques or are plaques a result of vascular issues? As with the mitochondria cascade hypothesis, this also struggles to reconcile FAD and its link to APP mutation. The amyloid cascade hypothesis, while the most prolific and developed, also has key issues. Firstly, a third of healthy control subjects show increased amyloid plaque levels but no signs of cognitive impairment that might indicate early onset Alzheimer's disease (Villemagne et al. 2011). If Aβ initiates the cascade leading to Alzheimer's disease why do they show no signs of impairment; although on the timescales for the preclinical Alzheimer's disease, this population may be included in that group. A second issue arises with the oxidative stress. While it is well reported that Aβ is able to propagate and cause oxidative damage (Butterfield and Lauderback 2002), it is still conflicting with the reports that oxidative damage precedes elevated Aβ levels and plaques, however this was studied with induced oxidative damage or already diagnosed Alzheimer's disease patients (Nunomura et al. 2001; Arimon et al. 2015). Thirdly, a great number of drug trials based on the hypothesis have failed (Cummings, Morstorf, and K. Zhong 2014; Castellani, Plascencia-Villa, and Perry 2019), indicating either an error or lack of complete understanding in the amyloid cascade hypothesis.

The alternative hypotheses offer differing root causes, leading to the same outcome. They do not refute the role of Aβ in the disease progression and each attempts to explain the involvement of Aβ within their framework, summarised in table 1.1. No hypothesis discussed here claims that Aβ is not a key step of the process of pathogenesis and while the exact involvement of Aβ is not completely understood, the current scientific consensus is that it has a key involvement in Alzheimer's disease.

Regardless of the issues with the amyloid cascade hypothesis, it remains the dominant forces in Alzheimer's disease research. Evolving and adapting to try and encompass the increasing volume of data. One such adaptation is that of the amyloid oligomer hypothesis (Walsh and Selkoe 2007). This hypothesis posits that the intermediate stages of oligomerisation have the neurotoxic effects, and that plaques exist merely as the end state of the process, mediate by molecular chaperones to neutralise and minimise damage and are themselves not harmful (Wolfe and Cyr 2011). A schematic

Hypothesis	Summary of link to Aβ
Amyloid Cascade	Aβ is the root cause of pathogenesis (Selkoe 1991; J. A. Hardy and Higgins 1992)
Mitochondria Cascade	Mitochondrial dysfunction leads to oxidative stress causing abnormal processing of APP (Swerdlow and Khan 2004; Swerdlow, Burns, and Khan 2014)
Dual Pathway	Factor upstream of both Aβ and Tau causes pathogenesis (Small and Duff 2008)
Vascular	Vascular issues cause oxidative stress causing abnormal processing of APP (Torre 2008)
Amyloid-oligomer	Aβ oligomers are the root cause of pathogenesis (Walsh and Selkoe 2007)

Table 1.1: Summary of the link each hypothesis has with Aβ in the pathogenesis of Alzheimer's disease.

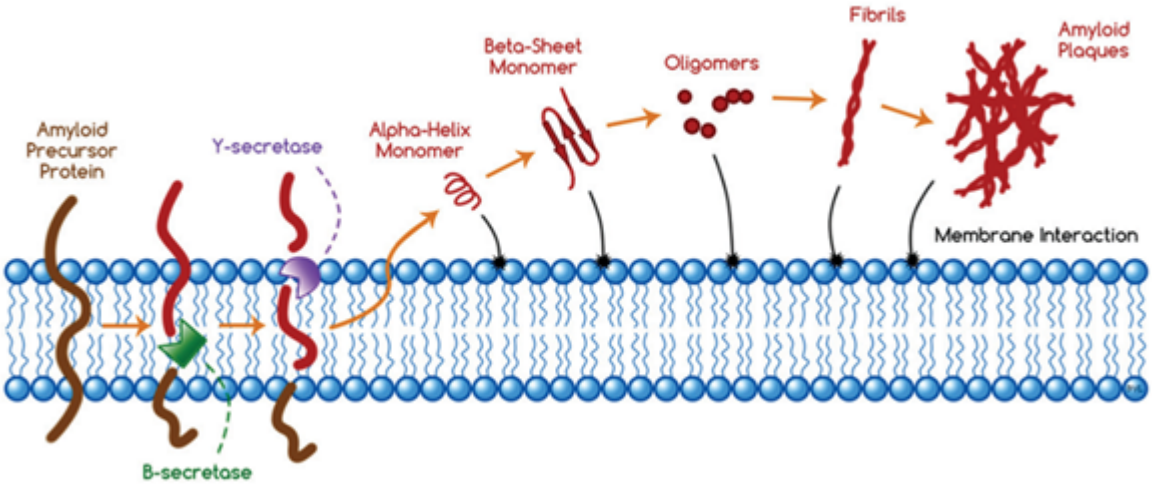

Figure 1.1: Schematic showing the stages of formation of an amyloid plaque, initiating from the integral amyloid precursor protein. It is then cleaved, yielding a monomer which undergoes a conformational change and begins to aggregate. First into oligomers, then into fibrils and finally into plaques (Drolle et al. 2014)

view of the stages of amyloid aggregation from its initial uncleaved state as part of APP until its eventual formation to an amyloid plaque is shown in Figure 1.1 (Drolle et al. 2014). At each stage of the aggregation there is potential for amyloid membrane interactions to occur.

The Aβ peptide itself takes a range of forms, shown in Figure 1.1. In the monomeric state Aβ can exist in an alpha-helical or beta-sheet conformation depending on the chemical environment. The peptide in each of these states has been shown in Figure 1.2. The helical state occurs in apolar environments, such as within the cell membrane (Crescenzi et al. 2002). The beta sheet structure occurs in aqueous environments, similar to outside the cell membrane, where plaques are observed (Lührs et al. 2005).

1.2.5 The role of the cell membrane in the amyloid hypothesis

Amyloid plaques are extracellular, found outside the cell. In the interstitial fluid around the cells the concentration of Aβ is not high enough for spontaneous aggregation (Karran and De Strooper 2016). It has been proposed that at these physiological levels without the involvement of lipids, the aggregation kinetics are not feasible (Habchi et al. 2018). The membrane can act as a surface to facilitate aggregation and initiate the templating process of secondary nucleation (Zhang et al. 2012).The nature of the interaction

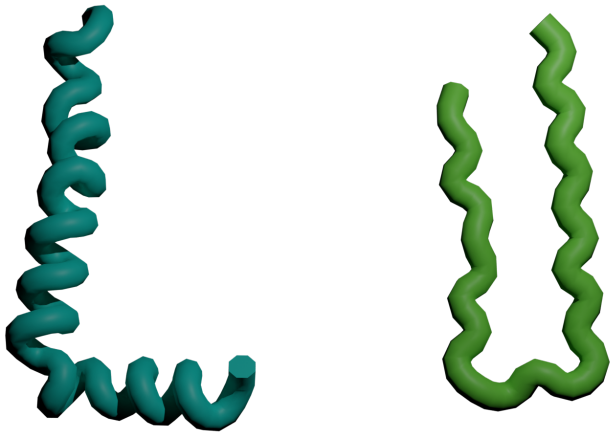

Figure 1.2: Two states of human Aβ. 3D structures, derived from solution nuclear magnetic resonance spectroscopy, for an alpha-helical Aβ peptide (left) (Crescenzi et al. 2002) and a beta-sheet Aβ peptide (right) (Lührs et al. 2005). Both visualised in a ribbon style.

between lipids and Aβ is still ongoing research, much has been undertaken into specific lipid components to measure their effects. As depicted in Figure 1.1, the lipid bilayer has interactions potentially at each stage of the aggregation. Aggregation does still occur without the involvement of lipids, however, they have a complex nature. The source of Aβ, APP, is a transmembrane integral protein (permanently attached to a lipid membrane, a schematic is shown in Figure 1.1) (O'Brien and Wong 2011). Aβ is cleaved in the local environment of lipid membranes so the interactions should not be discounted. It is suggested that the interaction of Aβ with neuronal cells is via perturbation of the cell membrane. Altering the homeostasis of cholesterol by inhibiting cholesterol synthesis (Gong et al. 2002), the alterations in cholesterol metabolism cause the tau phosphorylation which leads to tangle formation. This process may be a protective mechanism, as rodent lifespan has been shown to increase with reduced cholesterol synthesis with little change to amyloid itself (Halford and Russell 2009). Although no difference in tau levels was noted, tangles were not quantified. Aβ interacts with the cellular processing of oxidised lipoproteins, inducing an increase in lipid peroxidation in the cell (Kunjathoor et al. 2004), causing oxidative stress.The lipoprotein ApoE is one of the highest genetic risk factors in Alzheimer's disease (Puglielli, Tanzi, and Kovacs 2003). ApoE determines the homeostasis of brain lipids and cholesterol (Leoni,

Solomon, and Kivipelto 2010; Zhu et al. 2015). It is involved in the early stages of Aβ degradation and in the formation of fibrils. ApoE has 4 isoforms, ApoE4 is associated most with Alzheimer's disease, and encourages aggregation and decreases Aβ clearance (Fagan et al. 2002).

1.2.6 The structure of lipids and cholesterol

Lipids are are a diverse group of amphiphilic molecules that, along with a variety of proteins, form the cell membrane. They consist of a hydrophilic headgroup and hydrophobic hydrocarbon tails. Three lipids are shown in Figure 1.3. The three lipids, dioleoylphosphatidylcholine (DOPC), dipalmitoylphosphatidylcholine (DPPC) and sphingomyelin (SM) all have the same phosphocholine headgroup and differ in their tails. DPPC is fully saturated where DOPC features a single double bond midway down each tail. SM differs from DPPC in a more complex way, comprising of a sphingosine and fatty acid where DPPC consist of two fatty acids, specifically palmitic acid. These differences in the lipids allow for a range of different properties. The unsaturated tails of a lipids encourage a much more disordered bilayer, which will lead to a reduced main phase transition temperature (J. H. Davis, Clair, and Juhasz 2009; Biltonen and Lichtenberg 1993).

The amphiphilic nature of lipids allow them to self assemble into structures such as micelles or bilayers. This self assembly depends on the molecular geometry of the lipids (Israelachvili, D. Mitchell, and Ninham 1977) and the chemical environment (Gupta, Muralidhara, and H. T. Davis 2001). A bilayer is formed of two leaflets of lipids with their hydrophobic tails facing inwards, away from any water, and their headgroups facing outwards, this can be seen in Figure 1.1. The cell membrane is a bilayer formed of a complex mixture of lipids and proteins (Harayama and Riezman 2018). Another component in the cell membrane is cholesterol, shown in Figure 1.3. Cholesterol resides within the lipid bilayer and can alter the properties of the bilayer in a range of ways. It can alter the fluidity, encouraging a more ordered bilayer and shifting the phase transition temperature and in certain mixed lipid bilayers it also induces phase separation, allow the formation of more ordered regions of lipid, called rafts, within the disordered lipids (Smondyrev and Berkowitz 1999; Chong and Choate 1989; Schmidt and J. H. Davis 2017). It also alters the bilayers thickness and permeability (Pencer et al. 2005; Raffy and Teissié 1999).

Lipid peroxidation is a free radical reaction (Ayala, Muñoz, and Argüelles 2014). It

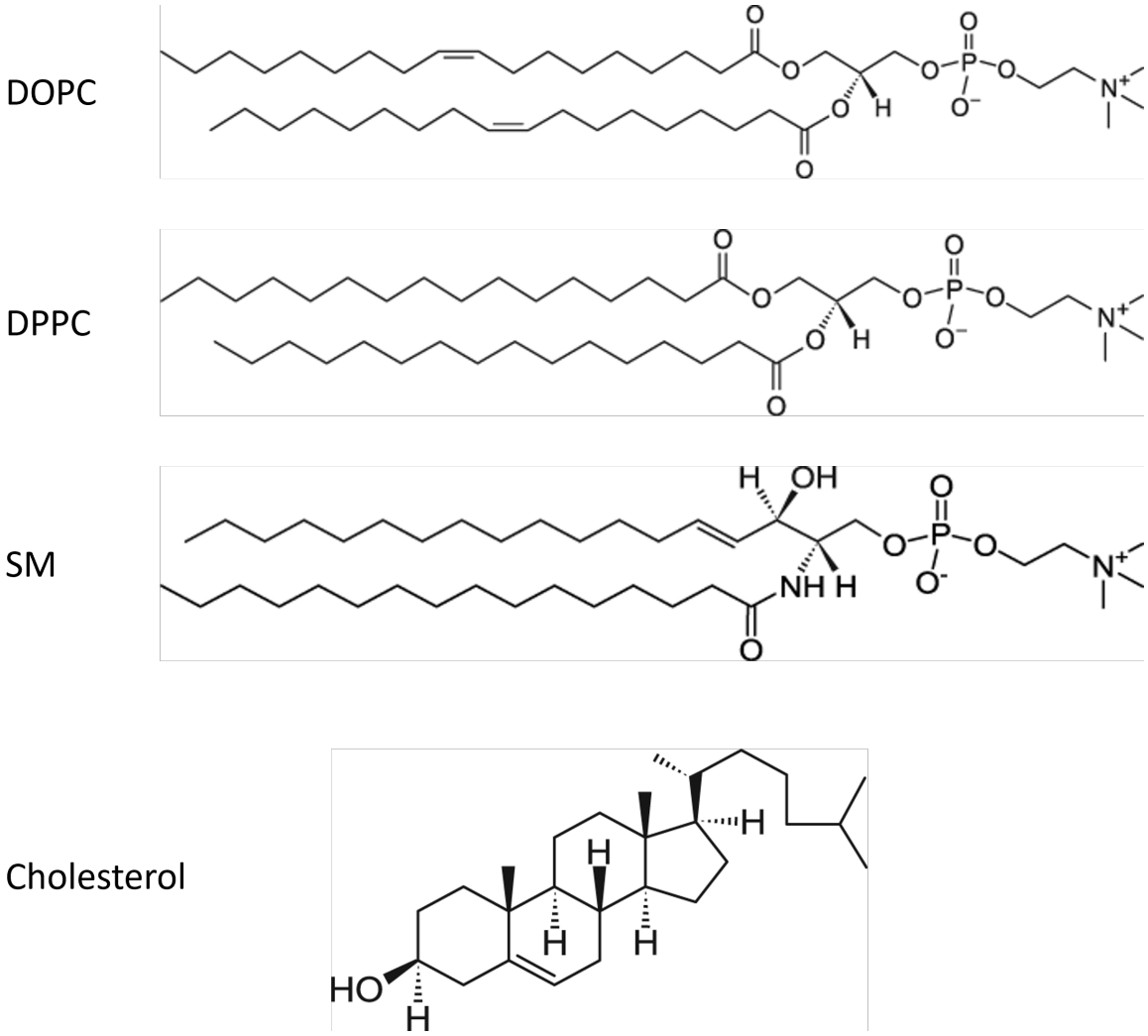

Figure 1.3: Chemical structures of DOPC, DPPC, SM and Cholesterol. DOPC, DPPC and SM all share the same headgroup and differ in their tails, this leads to differing properties.

has three main steps: initiation, propagation and termination. In the initiation step the lipid fatty acid tail reacts with a reactive oxygen species to generate a fatty acid radical. The fatty acid radical then react with oxygen to create an intermediate radical which is able to react further with another lipid fatty acid tail, converting that into a fatty acid radical and propagating the reaction. If two fatty acid radicals react and do not form a radical species this terminates the chain reaction. This termination can also be facilitated by antioxidant molecules in the cell membrane such as vitamin E.

The peroxidation of lipids, especially in complex composition membranes, leads to many lipid peroxidation products (LPP), molecules from the various stages of the lipid peroxidation free radical reaction. The ultimate effect on the lipid tail itself is either a chemically altered lipid hydroperoxides, a lipid with an OOH added to the tail which contains all original carbons. The other tail peroxidation effect is truncation of the lipid tail, where the tail is cleaved by the process leaving a lipid without all the original carbons (S. Davies and Guo 2014). Cholesterol is also capable of peroxidation with a range of hydroperoxide forms (Girotti and Korytowski 2019).

1.2.7 Experimental methods for examining amyloid-membrane interactions

The Aβ aggregation kinetics and mechanism can be assessed using techniques such as thioflavin T (ThT) fluorescence and quartz crystal microbalance. ThT kinetics rely on the fluorescence of a dye when in the presence of amyloid fibrils (Malmos et al. 2017). Extensive work has been accomplished with this technique to show cholesterol accelerating primary nucleation pathway of Aβ aggregation (Habchi et al. 2018) and the possible role of lipid mixture complexity in tempering aggregation (Sanguanini et al. 2020). It has also revealed slower aggregation when Aβ is initially incorporated into lipids (Qiang, Yau, and Schulte 2015) and that the aggregation of amyloid fibrils has a monomer dependant secondary nucleation pathway (Cohen et al. 2013). It was also found that DOPC does not interact with the primary nucleation pathway, instead accelerating this secondary nucleation (Lindberg et al. 2017). Quartz crystal microbalance experiments have corroborated this, with results showing the lipid binding of aggregated but not monomeric Aβ in the lipid mediate amyloid aggregation mechanism (Kotarek and Moss 2010). The ThT assay is not without flaws, it is highly susceptible to differences in agitation and preparation of samples and replication has proved difficult between research groups (Batzli and Love 2015). Despite this the ThT assay remains a

useful technique for characterising amyloid aggregation and has provided much useful insight in the effect of lipids at altering the aggregation kinetics and mechanism of Aβ formation. Piecing together kinetics data can suggest the basis of a mechanism for aggregation involving lipids. Aβ monomers undergo a primary nucleation, catalysed by certain lipids such as cholesterol, forming a fibril. Fibrils can elongate and act by a secondary nucleation mechanism, catalysed again by lipids such as DOPC. The interaction of lipids and Aβ and its effect on the mechanism and kinetics is complex and currently not completely understood. Estimates of aggregation timescales, without the involvement of cholesterol, at physiological cellular levels are on the order of decades-centuries, the involvement of cholesterol catalysis decreases this to months-decades (Habchi et al. 2018). Secondary structure determination of Aβ in lipid systems can be measured using techniques such as circular dichroism spectroscopy and Fourier transform infrared spectroscopy. This has been used to explore the conformational changes during the aggregation process, from alpha-helical to beta-sheet rich conformations before aggregating. Fourier transform infrared spectroscopy can show increased amounts of beta-sheet conformation Aβ when exposed to lipids with oxidative damage accelerating the conformational change required for aggregation (Koppaka and Axelsen 2000). This could explain an autocatalytic mechanism. Aβ is able to oxidise lipids, oxidised lipids increase Aβ levels and make the aggregating conformation more favourable (Koppaka and Axelsen 2000; Arimon et al. 2015; Grimm et al. 2016; Gunn et al. 2016). Fibrils can be imaged using techniques such as atomic force microscopy and transmission electron microscopy. Cholesterol has been shown to increase the degree of twist in amyloid fibrils, without altering the thickness or length (Habchi et al. 2018; Liu, Tian, and Shen 2020).

1.2.8 Atomic force microscopy in amyloid research

Atomic force microscopy (AFM) allows for probing of the surface of a supported lipid bilayer (SLB) whilst allowing simultaneous probing of membrane mechanics. It can be used to image surface topography at nanometer resolution and through tip indentations can be used to probe mechanical and structural properties including Young's modulus and thin film thickness. As with previously mentioned transmission electron microscopy, atomic force microscopy (AFM) allows the imaging of formed amyloid fibres. Aβ does not spontaneously form fibrils on mica surfaces, instead samples must be dried to visualise them (Drolle et al. 2014; Relini, Marano, and Gliozzi 2014; Habchi et al. 2018). However unlike transmission electron microscopy, the bilayer-peptide systems can

be interrogated under liquid conditions, and important consideration in biomolecular interactions. AFM has enabled study of the formation of pore structures in porcine brain lipid extracts which act as ion channels (J. Lee, Kim, et al. 2017). This was seen to be dependant on the initial state of amyloid, with lower initial molecular weight Aβ being much more destructive and pore forming. At higher molecular weights fibrils formed (Mrdenovic et al. 2019). Mechanical properties of porcine brain total lipid extract bilayers show that, regardless of the initial Aβ state, the stiffness (Young's modulus) of the bilayer Aβ reduces similarly and significantly by 45%. The fibrils, although not visually damaging the bilayer are still effecting integrity of the bilayer (Mrdenovic et al. 2019). The formation of fibrils in liquid as seen on the brain lipid extract is not seen on bare mica, the fibrils remain soluble. A reduction in stiffness is also seen in model system of comprising of DOPC, DPPC, and cholesterol when exposed to Aβ (Gao, Wu, and Lai 2020), and is not just a phenomena seen in complex extract based systems. The complexity of lipid interaction is still not completely understood, and Aβ-membrane interactions differ depending on composition. Much experimentation is done at much higher (micromolar) than at physiological concentrations (picomolar-nanomolar), AFM surface imaging at low concentrations has shown oligomer association and dissociation from the model lipid bilayers in a surface catalytic manner (Banerjee et al. 2020). Phase separation occurs in SLBs. In more physiologically relevant, complex systems, such as the cell, this is debated (S. Munro 2003). The phase separation has been shown to alter the behaviour of inserting Aβ, inserting preferentially with the liquid disordered phase. They saw little interaction with Aβ in single phase liquid disordered bilayer however to induce phase separation cholesterol was added which as previously discussed interacts complexly with Aβ (Azouz et al. 2019). This differing behaviour based on single component disordered bilayers or mixed phase-separated bilayers indicates that the interaction of Aβ is not just dependant on lipid order but that the existence of interfaces in the bilayer might be key such as providing adsorption and nucleation sites for the Aβ. While model systems prove incredibly useful for probing the involvement of a single lipid on Aβ, due to the composition dependency and compositional complexity of lipid membranes there has been a drive towards more physiologically relevant systems; however in all current brain total lipid extract AFM experiments, the source is porcine. Despite having a complex composition porcine brain total lipid extract SLBs form a single phase (Canale et al. 2018).

1.2.9 Molecular dynamics simulations of amyloid-membrane interactions

Computational work can go hand in hand to assist with the understanding of experimental results and develop deeper understanding of the systems involved. Molecular dynamics (MD) aims to approximate the atomic motion of molecules to measure the complex interactions on the nanoscale. There are current limitations regarding simulation length and size. When trying to measure amyloid aggregation, which experimentally acts on a timescale of hours, this can prove problematic. The use of steered MD and coarse-graining techniques can help alleviate this. Simulations are only approximations, relying on the quality of parameters they use, in the case of MD this is the forcefield. They should not be looked at in isolation, instead used as a tool with experiments, to confirm results and provide further understanding into the behaviour that cannot be measured experimentally. Forcefields need to be carefully selected and validated to avoid spurious claims (Krupa, Quoc Huy, and M. S. Li 2019). Simulations show how Aβ can stabilise pores in bilayers, decreasing the free energy of maintaining a pore in the DPPC bilayer and increase lipid order both with and without a pore formed (Pobandt and Knecht 2014). Explaining why AFM images of pore formation, the stabilisation reduces the equilibrium drive of the lipids back to complete bilayer. Studying the thermodynamic cycle of dimerisation involving DOPS and DPPC showed differing interactions further confirming the complex nature of the interactions between Aβ and lipids, it also noted the importance of the charge of the N-terminal half of Aβ in the process (C. H. Davis and Berkowitz 2010). Large coarse-grained simulations have shown the mechanical stress aggregating Aβ can put lipid bilayers under, inducing curvature, without any conformational change (a shortcoming of the MARTINI coarse-grained forcefield is the fixed peptide secondary structure) (Pannuzzo et al. 2013). The structure of ion-channels formed in the lipid bilayers has been studied, allowing further understanding of the surface changes in AFM topography maps, comparing similarities with 18-mer barrel ion-channels with experimental results (Connelly et al. 2012; J. Lee, Kim, et al. 2017). A single point mutation was shown to collapse the pore, further corroborating the validity by confirming experimental conductance results (Capone et al. 2012). This pore collapse was not measurable with AFM due to size constraints of the radius of curvature of the AFM tip. The effect of different animal Aβ sequence (human and rat) have been compared with a variety of bilayers. Importance of the lipid rather than the sequence was shown, with similar results for both sequences varying based on the lipid composition (Brown and Bevan 2017). Mutation studies are

not uncommon, and variants to represent oxidised Aβ (Fatafta et al. 2020), familial human mutated Aβs (from Sweden, Taiwan and the Netherlands), showing differences in conformation with less beta-sheet, explaining reduced aggregation (Huet and Derreumaux 2006; Lam et al. 2008; Truong et al. 2014), and even a single simulation of naked mole-rat (NMR) Aβ (Vahed et al. 2019). Regardless of the oxidisation state, Aβ preferentially bound with the ganglioside lipid GM1 (Fatafta et al. 2020). The involvement of GM1 with Aβ aggregation is conflicting, often associated with phase separation, encouraging aggregation, and providing the highest potential to act as a 'seed' for secondary nucleation (Yuyama and Yanagisawa 2010; Hong et al. 2014). GM1 has also been shown to hinder aggregation by another lipid, sphingomyelin (Amaro et al. 2016). Alone sphingomyelin increases the conformational change of Aβ, where GM1 does not (M. C. Owen et al. 2018). Increased levels of sphingomyelin have been observed in Alzheimer's patients brains (Varma et al. 2018). With these conflicting results the understanding of these lipids is clearly not complete. NMR sequence Aβ had less conformational flexibility compared to human sequence Aβ and also had less sites for iron interaction. It is suggested iron provides an alternate aggregation path as metal imbalances have been noted in Alzheimer's disease (Greenough, Camakaris, and Bush 2013; Vahed et al. 2019).

1.2.10 Molecular dynamics simulations of membrane phase behaviour

Even in simulations of single component lipid bilayers there exists interesting phase behaviour, particularly in the case of lipids with large phosphatidylcholine headgroups such as DPPC. The main phase transition is characterised by the melting of the acyl chains with increasing temperature (Tardieu, Luzzati, and Reman 1973). Although the chains are hydrocarbon chains, the melting is more complex than the simple model due to the anchoring of the chains to the lipid headgroups (Nagle 1980).

Most MD simulations are undertaken in fluid phase, above the main transition temperature, however depending on the lipid this might not be the most relevant temperature range to use. Simulations containing lipids from the previous section related to Aβ-bilayer interactions include the work of Pobandt and Knecht (2014) and C. H. Davis and Berkowitz (2010) at 323 K, or were unclear as to the temperature used such as the work by Connelly et al. (2012), J. Lee, Kim, et al. (2017), and Capone et al. (2012). While there is a case for running increased temperature simulations to accelerate dynamics and overcome energy barriers, conclusions drawn from these higher

temperature simulations might not be valid at the more realistic temperature if there is a phase transition.

In the case of certain lipids, such as DPPC, there exists and intermediate phase below the main phase transition, the ripple phase, discovered experimentally 50 years ago (Tardieu, Luzzati, and Reman 1973). The ripple was observed using MD simulations much later (Vries et al. 2005). In contrast with the experimental findings that the ripple consisted of a gel-like and fluid-like coexistence in a saw-tooth structure (W. J. Sun et al. 1996), the early simulations instead found a splayed-gel region and extensively interdigitated region (Vries et al. 2005). Similar conclusions have been drawn from coarse-grained models (Lenz and Schmid 2007). More recent simulations continue to report to two phase coexistence as well (Walter, Ruscher, Benzerara, et al. 2020; Khakbaz and Klauda 2018).

The ripple phase in single component systems has not yet been explained (Walter, Ruscher, Gola, et al. 2021) with research ongoing even experimentally (Akabori and Nagle 2015).

At even lower temperatures below the ripple phase there also seem to be issues, with the tilted gel phase shown to be highly dependant on its thermal history and suffering from finite size effects at commonly simulated bilayer sizes (Walter, Ruscher, Gola, et al. 2021).

Lipid bilayers with more complex mixed compositions are also simulated, with the phase behaviour guided by the composition. Cholesterol for example has a complex interaction with lipid phases depending on the lipid species and phase (Sodt, Pastor, and Lyman 2015). Preferentially interacting with the lipid tails via its rough/smooth surface depending on the lipid it interacts with.

Phase separation in complex lipid bilayers within atomistic MD simulations does not occur on the timescales of common simulations, instead coarse-grained simulations or careful system building are required to express phase separation (Sodt, Pastor, and Lyman 2015; Fowler et al. 2016; Weiner and Feigenson 2019; Oliveira et al. 2021).

1.2.11 The naked mole-rat as a model in ageing research

NMRs show a surprising longevity. They are the longest living rodent (Buffenstein and J. U. M. Jarvis 2002), and retain many neotenic features (Orr et al. 2015; Buffenstein, Lewis, et al. 2020). The current oldest animal, a 37 year old male, is still living consequently the maximal lifespan has yet to be determined. Regardless, this is an order

of magnitude longer than that of a mouse (Buffenstein 2008). It has been shown that the maximum life-span of an animal is correlated with its mass (Magalhães, Costa, and Church 2007). Despite mice and NMRs having a comparable mass, there is a significant difference in maximum life span (Buffenstein 2008). This longevity relative to size has led to the NMR being suggested as a model for ageing, as ageing in short-lived animals can act much differently (D. J. Holmes 2004). The NMR seems to break many conventions associated with ageing. They show increased oxidative stress from a young age (Andziak and Buffenstein 2006) which is more constant across age than in mice (Andziak, O'Connor, et al. 2006). With this high level of oxidative damage NMRs do not seem to have an antioxidant defence mechanism, and as with the oxidative damage the levels of antioxidants are constant with age (Andziak, O'Connor, and Buffenstein 2005). The oxidative stress experienced by the NMR does not seem to cause issues with protein structure, function or stability (Pérez et al. 2009; De Waal et al. 2013). The NMR is long lived and resistant to many of the indicators associated with ageing in other species such as humans. This is exemplified by the NMR mortality rate in that it does not follow a Gompertzian rate (Ruby, M. Smith, and Buffenstein 2019). Most species, humans included, follow a Gompertzian mortality rate; the probability of death in a given year increases with the animal age (Gompertz 1825). These has been some dispute over this finding in NMRs, specifically the oldest animals (Dammann et al. 2019) but even disregarding those data it is a testament to the longevity of the NMR. It has been suggested that this longevity and oxidation resistance is a result of many factors: lipid composition (A. J. Hulbert, Faulks, and Buffenstein 2006; T. W. Mitchell, Buffenstein, and A. Hulbert 2007), metabolism (Sherman and J. U. Jarvis 2002; Lewis, Rubinstein, and Buffenstein 2018), and maintained gene splicing regulation (B. P. Lee, M. Smith, et al. 2020). The lipid composition of the NMR would suggest it is highly resistant to oxidative damage. The lipid composition contains much less oxidation prone polyunsaturated fatty acids, such as docosahexaenoic acid; the most polyunsaturated fatty acid in mammalian membranes (A. J. Hulbert, Faulks, and Buffenstein 2006; T. W. Mitchell, Buffenstein, and A. Hulbert 2007). Despite this resistant lipid composition, the NMR does still encounter a high degree of oxidative stress. The metabolomic signature of the NMR has been studied to give insight into their longevity. NMRs have shown decreased markers for the methionine pathway, something seen in animals in torpor hibernating (Lewis, Rubinstein, and Buffenstein 2018). Methionine restricted diets have been shown to extend lifespan in mice and humans (J. E. Johnson and F. B. Johnson

2014; Bárcena et al. 2018), even reversing signs of ageing when applied later in life to rats (Sanchez-Roman et al. 2012). In humans, splicing factors and isoform expression alter with age. In NMRs this is not the case (B. P. Lee, M. Smith, et al. 2020). Splicing factor expression has been linked with lifespan of mice (B. P. Lee, Pilling, et al. 2016). Much of the research into NMRs, particularly on a biomolecular level, has all been conducted on the same colony of NMRs. This is a flaw in a rarer animal models such as this, that do not have the same widespread usage of the more common models such as with mice or rats.

1.2.12 The naked mole-rat and neurodegeneration

Along with general longevity, the NMRs do not show signs of many neurodegenerative diseases with this age. Instead, they remain generally healthy across their lifespan in general. Specifically for Alzheimer's disease, they show little cognitive impairment during life or plaque formation post mortem, despite having incredibly high concentrations of Aβ (Edrey, Medina, et al. 2013). The levels are equivalent to that of the 3xTg-AD mouse model; a model used for Alzheimer's research. Rodents not expressing plaques is not unique to the NMR but also expressing the high Aβ concentration as well as not expressing plaques is (Chishti et al. 2001; Oddo et al. 2003). Alongside this, NMRs also have a greatly elevated concentration of Tau; which similarly to Aβ is equivalent to the 3xTg-AD mouse yet does not express as tangles (Orr et al. 2015). Given such high concentrations of the hallmark molecules of Alzheimer's disease and no expression of damage or aggregates that would be expected there must be some protective mechanism. The difference between human and NMR Aβ is a single amino acid. The thirteenth amino acid, histidine in humans, is an arginine in NMRs. Both variants have a similar neurotoxicity, but have shown a different aggregation propensity on surfaces with AFM when dried and with a kinetic ThT assay in solution (Edrey, Medina, et al. 2013). The kinetic assay results they provide are steady state (maximal) fluorescence values, and not the more commonly reported kinetic parameters of lag-time or maximal growth rate (or coupled half-maximal time) (Knowles, Vendruscolo, and Dobson 2014). This change in amino acid does not explain the resistance to Alzheimer's disease as the degu, another rodent, shares the NMR Aβ peptide amino acid sequence and does exhibit plaque formation (Inestrosa et al. 2005). The sequence alone does not determine the propensity of causing Alzheimer's disease pathology, instead the cellular response is also key (Roychaudhuri et al. 2015). High levels of Aβ in the NMR brain are not uniformly

distributed, with increased concentration in the hippocampus, a region of the brain Aβ has been suggested to initial accumulates in human cases of Alzheimer's disease (Gosche et al. 2002). Compared with mice and taking into account the amyloid cascade hypothesis, there is no increase in degradation, or decrease in production seen in the NMR brain (Edrey, Oddo, et al. 2014). NMRs reduced level of the ubiquitin-proteasome pathway (involved in Aβ degradation) is similar to that of human brains of Alzheimer's sufferers attributed to high oxidative damage (Keller, Hanni, and Markesbery 2000), which the NMR brain is under. The NMR offers an interesting and unique perspective with unanswered questions. How is the brain of the NMR able to survive with such high concentrations of Aβ and Tau without developing the hallmark plaques and tangles of Alzheimer's disease?

Chapter 2. Theory

2.1 Atomic Force Microscopy

Atomic force microscopy (AFM) is a technique to measure surface topography at the subnanometer scale and measure forces between the AFM tip and sample of interest (Eaton and West 2010, chapter 1)A laser in bounced off the back of a cantilever which contains a sharp tip. The position of the reflected laser is measured on a quadrant photo-detector to measure movement in the AFM tip, caused by forces of interaction between tip and sample, a schematic of this is shown in Figure 2.1. The cantilever is attached to a small piezo scanner and fine motors which can accurately move the cantilever and tip around the surface of the sample (Eaton and West 2010, chapter 2). AFM is able to operate at atmospheric pressures and in an aqueous environment enabling results to be more representative of physiological conditions, as opposed to a technique such as scanning electron microscopy, which would also reveal the topography, however conventionally requires the sample to be dried and under a vacuum. Moreover AFM allows the interrogation and measurement of features at the nano scale in three dimensions, as well as being able to probe local mechanical properties (Eaton and West 2010, chapter 2).

2.1.1 Contact mode topography imaging

In the above description, the AFM holds the cantilever at a fixed position (the right hand side of the cantilever in Figure 2.1), with the tip in contact with the surface, then the deflection of the cantilever can be measured and fed back with the piezo adjusting the position of the cantilever to maintain a constant force. This results in a topographical map of the surface as the tip scans the surface altering it's height in order to maintain constant force. This is known as contact mode imaging (Eaton and West 2010, chapter 3).

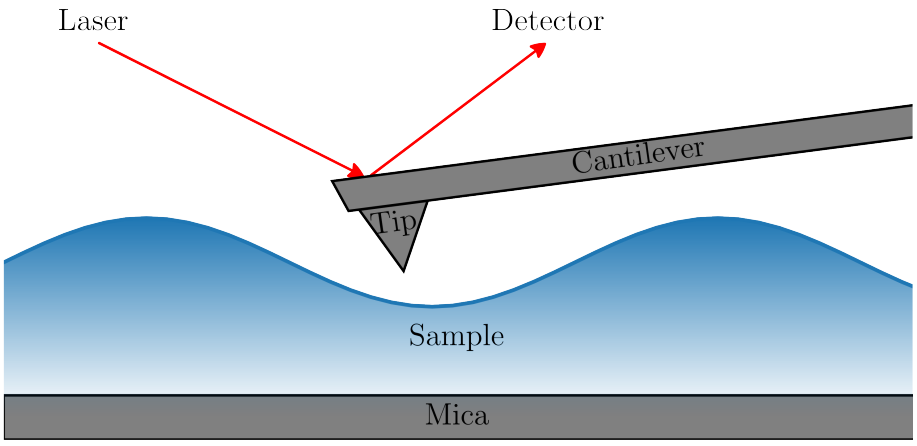

Figure 2.1: Diagram showing the basis of AFM tip interaction with a sample surface on a mica substrate. A laser is reflected off the back of the cantilever, above the tip, and onto a detector

2.1.2 *Tapping mode*

During tapping mode, the AFM tip is oscillated at it's resonance frequency by the peizo at a constant amplitude, resulting in intermittent contact with the surface. Tip-surface interactions will dampen this amplitude so the cantilever position is altered to return a predetermined constant amplitude value. This change in cantilever height is measured to give the topographical image of the surface. This can provide a gentler interaction with the surface minimising lateral forces and causing less damage to the sample (Eaton and West 2010, chapter 3).

2.1.3 *Nano indentation*

A tip used for contact mode is also capable of measuring indention forces into the sample (Eaton and West 2010, chapter 3; Cappella and Dietler 1999). This is a direct measurement of the tip-sample force across a range of tip-sample separations. The tip is brought towards the sample surface at a constant rate. Although this can only measure the cantilever position, z through Hooke's law the detected deflection voltage, V, can be converted to force, F, measurement

$$F(V) = -kx = -k\frac{V}{c} \tag{2.1}$$

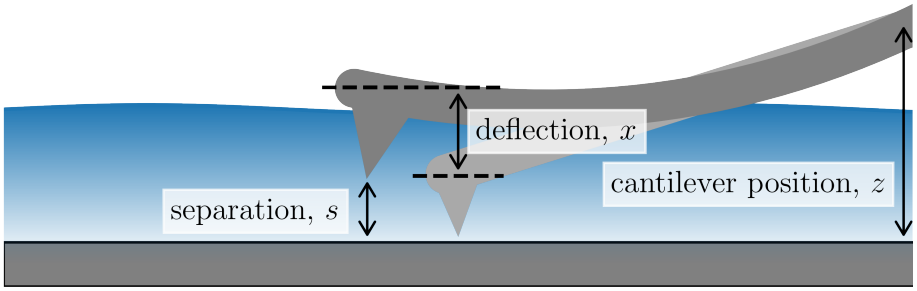

Figure 2.2: Diagram showing the indentation of an AFM tip into a sample for force spectroscopy. A deflected tip (dark grey) and undeflected, equilibrium position, tip (light grey) are shown.

where x is the cantilever deflection, k is the spring constant of the cantilever, calculated using the Thermal K method, which fits the value from the power spectral density of the thermal fluctuations of a simple harmonic oscillator model. The calculation of the spring constant of a contact mode tip is undertaken in air, before any sample has been introduced to mica.

The sensitivity correction, c, is taken against a hard sample, usually the underlying substrate of the sample and is given by

$$c = \frac{\Delta V_{mica}}{\Delta z_{mica}} \tag{2.2}$$

which can be recalculated for each indentation provided the tip was allowed to indent into the underlying mica enough to get sufficient data to effectively perform a linear fit to this region.

The tip-sample separation, s, can finally be calculated to account for the deflection, x, of the cantilever from the equilibrium position

$$s = z - x \tag{2.3}$$

The spatial terms of this are shown in Figure 2.2.

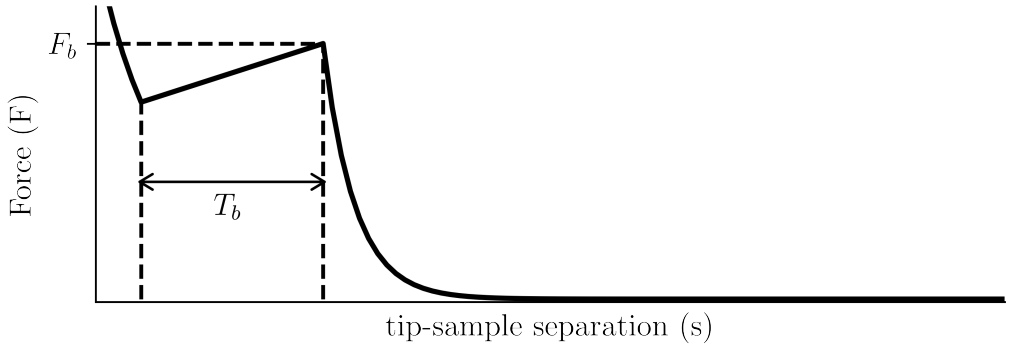

Figure 2.3: A force-separation curve showing an example of a lipid bilayer breakthrough event during a force spectroscopy indentation. The breakthrough force, F_b, and thickness, T_b, are indicated.

2.1.4 Breakthrough Events

Indentation of supported lipid bilayers (SLBs) can lead to breakthrough events of the lipids (Schneider et al. 2000). Two features of a breakthrough event, the breakthrough force and thickness are shown in Figure 2.3. Shown in Figure 2.4 are three key stages of the interaction between lipid bilayer and AFM tip. Firstly the AFM tip approaches the lipid surface, once it gets nearby short range interactions start to interact with the tip (panel A). Once the tip reaches the lipid bilayer surface, the AFM continues to approach the sample, but the cantilever deflects and the tip remains on the lipid surface (panel B). Once a critical breakthrough force, F_b, is reached the tip is able to overcome the surface tension of the lipid bilayer and 'jumps' breaking through the surface of the lipid bilayer (panel C). The approximate position on a force-separation curve of each of these stages are shown in panels D-F which show that away from the surface the applied force is zero, there is a sharp increase in force until the lipid bilayer is broken through. The separation of zero is set to the underlying mica, rather than the sample itself, based on the elastic (linear) indentation required for equation 2.2. The interaction of the tip and mica has not been shown.

2.1.5 High-throughput breakthrough detection

While breakthrough events can be manually measured, yielding the breakthrough force and thickness as shown in Figure 2.3, the automation of this process allows for a more reproducible, and high throughput analysis (J. K. Li, Sullan, and Zou 2011).

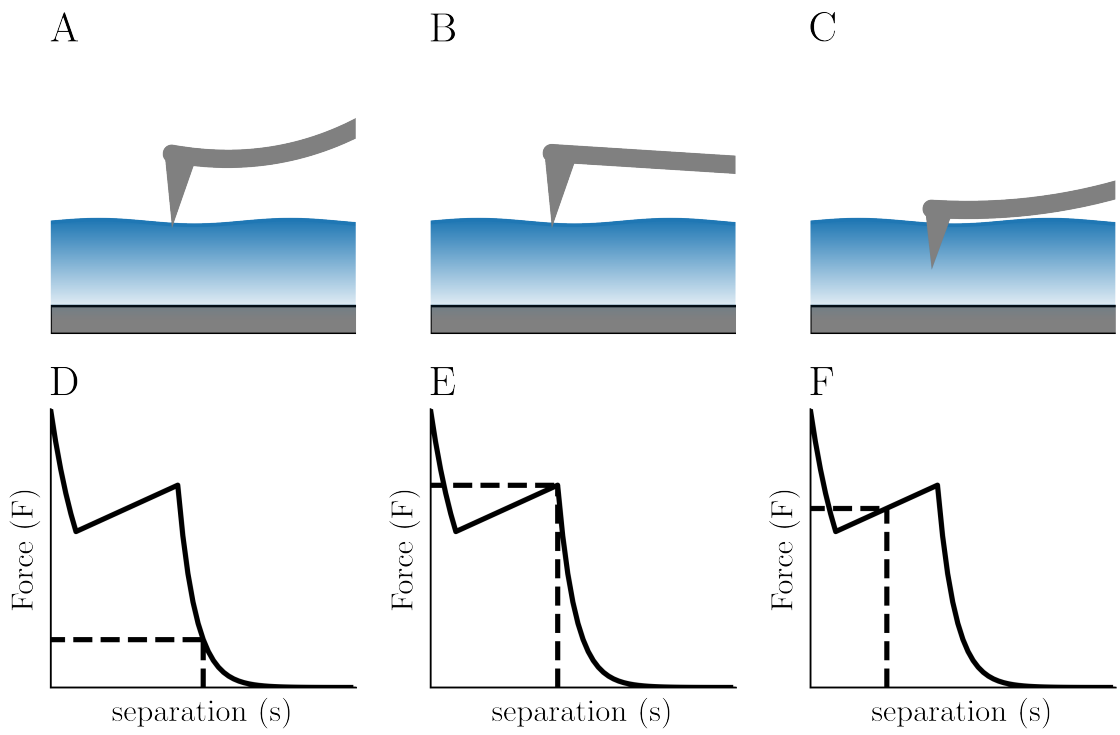

Figure 2.4: Stages of a lipid bilayer breakthrough event. The tip reaches the bilayer surface (A), the cantilever position continues lowering but is deflected by the sample surface so the tip doesn't move while the force increases (B), once the force applied exceeds the critical breakthrough force, F_b and the tip is able to push through the bilayer (C). The approximate position of each of these stages on the indentation curve is shown in panels D-F, with the black dashed line indicating the force and separation.

For each indentation in the set the raw voltage-distance curves are smoothed using a windowed moving average filter. The smoothed curves are then transformed into force separation curves using equations 2.1 and 2.3. This curve is differentiated and a sigmoidal background curve is fit and subsequently subtracted from this. The background corrected curve contains a prominent peak, which corresponds to the breakthrough event. The peak is present in the none corrected curve however due to the nature of the differentiated curve, detection of the peak without correction can be erroneous. An example of this processing can be seen in Figure 2.5.

2.1.6 Preparing supported lipid bilayers by vesicle fusion

Preparing lipid bilayers as a sample for AFM analysis can be accomplished using vesicle fusion (G. J. Hardy, Nayak, and Zauscher 2013). A mica substrate is cleaved to provide a flat substrate surface and gently heated to above the lipid transition temperature, T_m. A solution of unilamellar vesicles is deposited onto the mica and annealed gently causing the absorption then rupture of the vesicle into a single mica-supported bilayer, a single vesicle undergoing this process is shown in Figure 2.6.

2.2 Molecular Dynamics

Molecular dynamics (MD) is a computational tool to study the properties of atomistic systems (Frenkel and Smit 2002, chapter 4). Essentially, MD simulations are the numerical solution to Newton's Second law for systems of N interacting atoms. When $i = 1, 2, ..., N$ the force acting on atom i, F_i can be expressed as a function of the atom mass, m_i and acceleration, a_i using Newton's Second Law

$$F_i = m_i a_i \tag{2.4}$$

The force is equivalent to the negative derivative of the potential, V, with respect to position, r,

$$F_i = -\frac{\partial V_i}{\partial r_i} \tag{2.5}$$

A system is prepared with initial conditions, coordinates and interaction parameters. The forces on each atom is calculated, the new positions are updated and save, then this is repeated. This gives a trajectory of the atoms. Through the analysis of these coordinates, system properties can be extracted. This process has been shown in Figure 2.7.

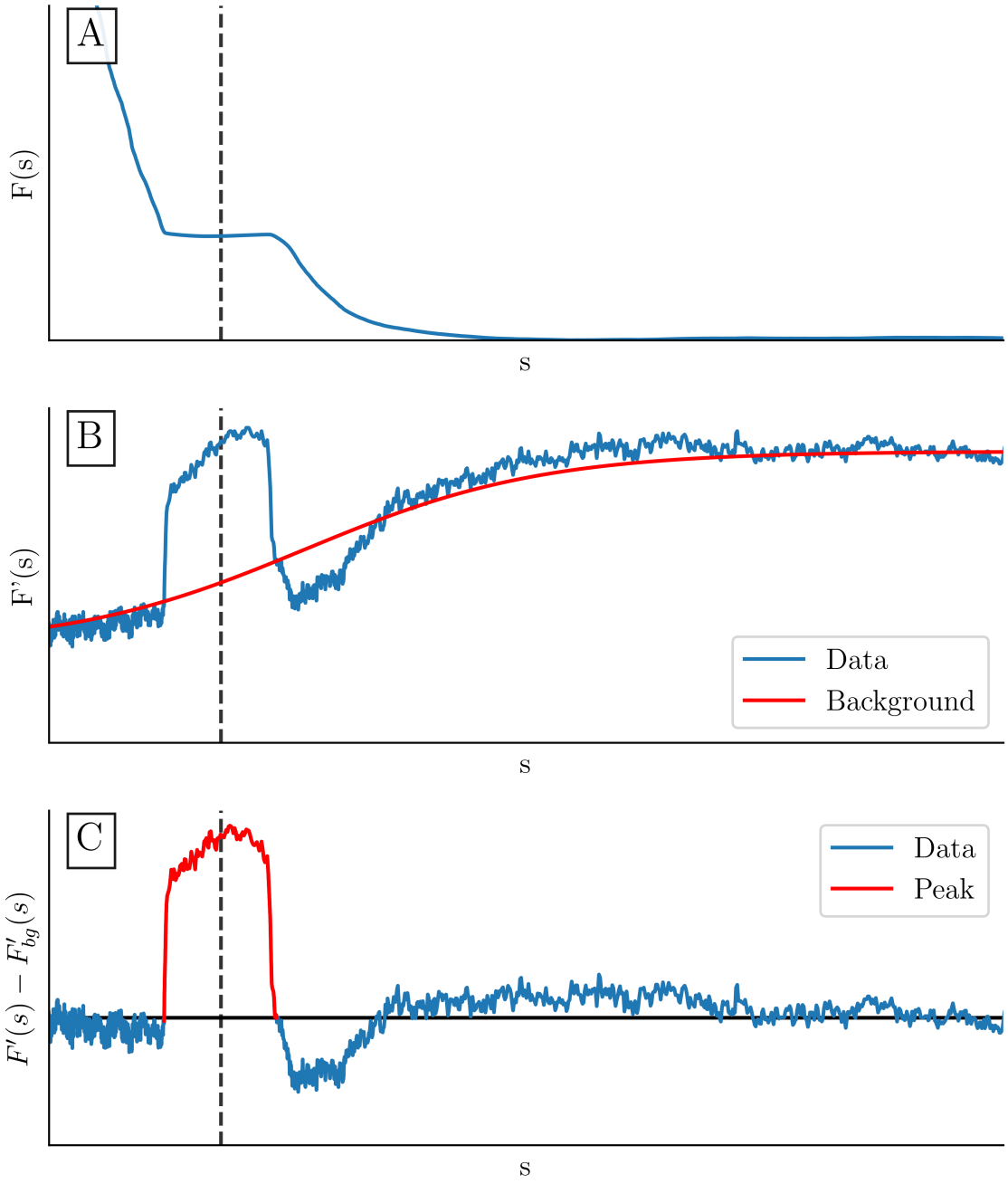

Figure 2.5: Annotated curves from various stages in the breakthrough identification algorithm. The force separation curve (A), differentiated force separation curve and fitted sigmoidal background (B) and background corrected curve showing prominent peak (C). The black dashed line has been added at the middle of the breakthrough event.

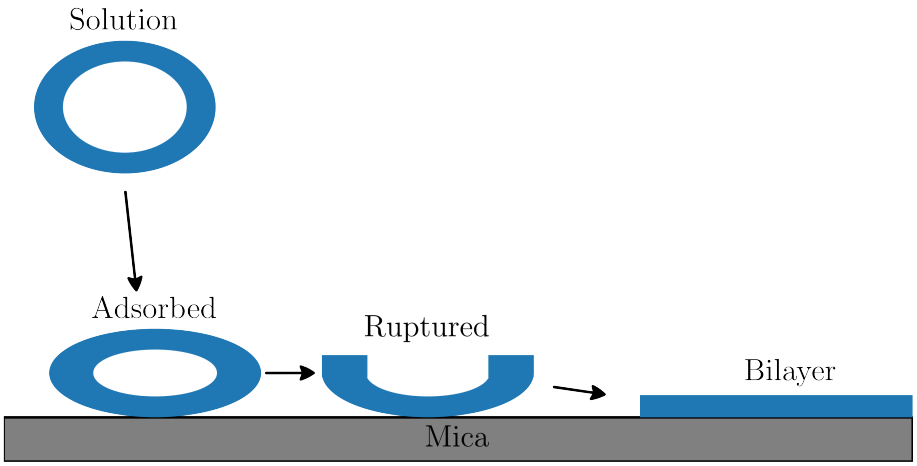

Figure 2.6: Diagram showing a schematic of the preparation of a SLB by vesicle fusion, only a single vesicle is shown, in the various states of fusion

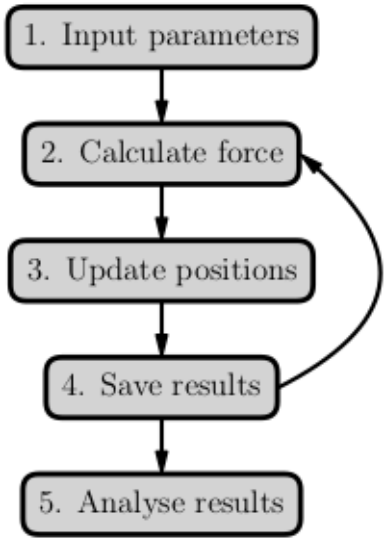

Figure 2.7: A basic overview of the steps in a simple MD simulation. Step 1 involves the forcefield and initial configuration of atoms. Steps 2-4 are repeated until enough simulation in completed for sufficient analysis.

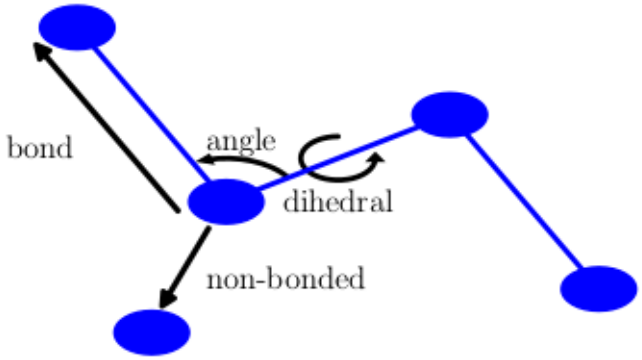

Figure 2.8: A diagram showing the forcefield component terms acting on an atom in a simple bonded chain interacting within the molecule (bond, angle and dihedral potentials), and with a nearby atom (non-bonded potential, which includes both Lennard-Jones and Coulombic interactions)

2.2.1 Forcefield

The interaction parameters between the different atoms is called a forcefield. This defines the potentials acting on the system, used to calculate the force term in equation 2.4. Typically the potentials acting on the system are categorised as bonded and non-bonded potentials. A forcefield approximates the system in question and is generated by fitting experimental data, or lower level quantum mechanical data. The form of the forcefield can vary but a general form often consists of sum of bonded and non-bonded terms. The bonded terms; the bond, angle and dihedral potentials are given by

$$V_{bonded} = \underbrace{\frac{1}{2}K^b_{ij}(r_{ij} - b_{ij})^2}_{\text{bond}} + \underbrace{\frac{1}{2}K^\theta_{ijk}(\theta_{ijk} - \theta^0_{ijk})^2}_{\text{angle}} + \underbrace{\sum_{n=0}^{5} C_n(\cos(\phi))^n}_{\text{dihedral}} \tag{2.6}$$

where K, b, θ^0 and C_n are all forcefield parameters. θ_{ijk} is the angle formed by the atoms i, j and k. ϕ is the angle formed by the dihedral, between the two planes formed by the 4 atoms involved. These terms represent the 2, 3 and 4 body interactions of nearby bonded atoms as shown in Figure 2.8. The non-bonded potentials; Lennard-Jones and Coulombic potentials are given by

$$V_{non-bonded} = \underbrace{4\epsilon_{ij}\left[\left(\frac{\sigma_{ij}}{r_{ij}}\right)^{12} - \left(\frac{\sigma_{ij}}{r_{ij}}\right)^{6}\right]}_{\text{Lennard-Jones}} + \underbrace{f\frac{q_i q_j}{\epsilon_r r_{ij}}}_{\text{Coulombic}} \tag{2.7}$$

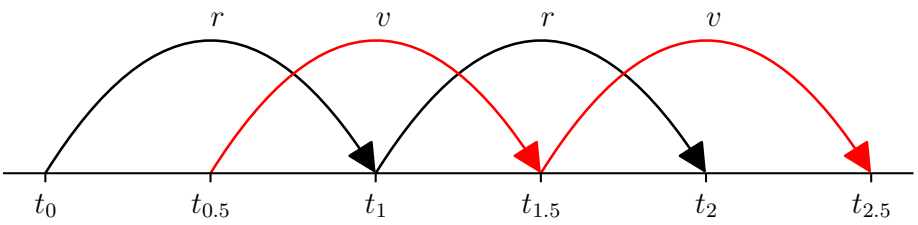

Figure 2.9: Schematic of the leapfrog integrator, showing the interleaving of the calculation of velocity and position on alternating half timesteps.

where ϵ is the potential well depth, σ is the Van der Waals radius, q_i is the charge of atom i, ϵ_r is the relative dielectric constant and f is the electric conversion factor, a constant ($\approx 138.9\,\mathrm{kJ\ mol^{-1}\,nm\,e^{-2}}$) (Bauer, Hess, and Lindahl 2022, chapter 5).

2.2.2 Integrator

Solving equation 2.4 is done by numeric integration. The integrator is key to MD. Two key features of the algorithm chosen are symplecticity and time-reversibility. The Verlet integrator family meets these requirements. In particular the leapfrog integrator (Frenkel and Smit 2002, chapter 4). The leapfrog algorithm is equivalent to other members of the family and named because the calculation of position, r, and velocity, v, do not occur at the same timestep, instead they are interleaved 'leapfrogging' over one another. Mathematically the leapfrog integrator can be formulated as

$$v\left(t + \frac{1}{2}\Delta t\right) = v\left(t - \frac{1}{2}\Delta t\right) + \frac{\Delta t}{m}F(t) \tag{2.8}$$

$$r(t + \Delta t) = r(t) + \Delta t v\left(t + \frac{1}{2}\Delta t\right) \tag{2.9}$$

where the velocity at step $t_{0.5}$ feeds forward to calculate the updated positions at t_1. The updated positions in turn alter the force term, F, which changes the velocities.

2.2.3 Temperature and Pressure coupling

A simulation run without accounting for the temperature and pressure coupling would be run in the microcanonical ensemble (NVE), that is the number of atoms (N), volume

(V) and total energy (E) are conserved quantities. This fully isolated system is not always representative of the system being simulated so the introduction of a thermostat to control the temperature (T) allows the simulation to be run in the canonical ensemble (NVT) (Frenkel and Smit 2002, chapter 6). A simple example of a thermostat is the Andersen thermostat, in which atoms are randomly reassigned a velocity from the correct temperature Boltzmann distribution (H. C. Andersen 1980). A more deterministic form of thermostat comes in the form of the Berendsen thermostat (Berendsen et al. 1984) in which the velocity of that atoms are scaled by a time, t, dependent scaling factor, λ so the system will converge to a desired temperature, T_0 controlled by a coupling constant, τ

$$\lambda^2 = 1 + \frac{\Delta t}{\tau}\left(\frac{T_0}{T(t - \frac{\Delta t}{2})} - 1\right) \tag{2.10}$$

Similarly to how the velocities are rescaled to control temperature the simulation, the box vectors, and relative position of the atoms within the box, can also be scaled by scaling factor, μ. Rescaling the simulation box is done to converge the system pressure, P, to a desired pressure, P_0. Controlling the pressure like this switches from NVT ensemble to the isothermal-isobaric ensemble (NPT). For an isotropic cubic box, the rescaling factor is given by

$$\mu = 1 - \frac{\kappa \Delta t}{3\tau}(P_0 - P) \tag{2.11}$$

where κ is the isotropic compressibility and τ is a coupling constant (Berendsen et al. 1984).

2.2.4 Periodic boundary Conditions

The systems simulated in MD are finite in size. This introduces boundaries into the system which in most cases are unnatural and problematic when attempting to simulate a bulk system. Periodic boundary conditions are applied to remove interface effects due to the boundary on the system. To achieve this the simulation box is wrapped, essentially duplicated with the left face of the box connecting to the right face, the top face to the bottom and the front face to the back which creates a representation of an infinitely large system provided the initial box is large enough that this doesn't introduce artefacts, for example via a molecule interacting with itself, or another single molecule multiple times, across the periodic boundaries (Frenkel and Smit 2002, chapter 3).

2.2.5 Analysis of molecular dynamics results

MD outputs large series of positional information about the atoms. A macroscopic property that is able to be experimentally measured can be calculated from a statistical ensemble of microscopic systems. The power of MD is in predicting and gaining insight into macroscopic properties by generating trajectories which sample many microscopic states. A macroscopic property, $\langle A \rangle$, can be approximated as the time average of the time series of a microscopic measurement of the instantaneous property, $A(t)$,

$$\langle A \rangle_{time} = \frac{1}{N_t} \sum_{t=1}^{N_t} A(t) \tag{2.12}$$

Assuming the system is ergodic then

$$\langle A \rangle_{ensemble} = \langle A \rangle_{time} \tag{2.13}$$

In practice this means simulations are required for a sufficiently long time to accurately sample the system (Frenkel and Smit 2002, chapter 1). Through the use of MD though additional information can be extracted from the trajectory, beyond the scope of, or more easily than experimental methods.

Analysis of lipid bilayer simulations has system specific properties which can be calculated. A convention of the simulated lipid bilayer normal being the Z axis has been used. A lipid bilayer consists of a pair of leaflets, the individual monolayers of lipids which combine to make the bilayer. Bilayer leaflets are often analysed separately.

A standard metric used to quantify the order in a lipid is the deuterium order parameter, S_{CD}. This measures the temporal and molecular ensemble average orientation of the C-H bond vector with the bilayer normal, θ

$$S_{CD} = \frac{\langle 3\cos^2\theta - 1 \rangle}{2} \tag{2.14}$$

The deuterium order parameter corresponds to results available to experimental nuclear magnetic resonance experiments (Piggot, Allison, et al. 2017).

The surface area per lipid, A_{lipid}, is usually calculated simply using the simulation box vectors, L, and the number of lipids per bilayer leaflet, $N_{leaflet}$

$$\langle A_{lipid} \rangle = \frac{\langle A_{leaflet} \rangle}{N_{leaflet}} = \frac{\langle L_X L_Y \rangle}{N_{leaflet}} \tag{2.15}$$

More complex analysis can calculate this on a per lipid basis, by generating a Voronoi tessellation (shown in Figure 2.10) in the XY plane. The surface area occupied by a

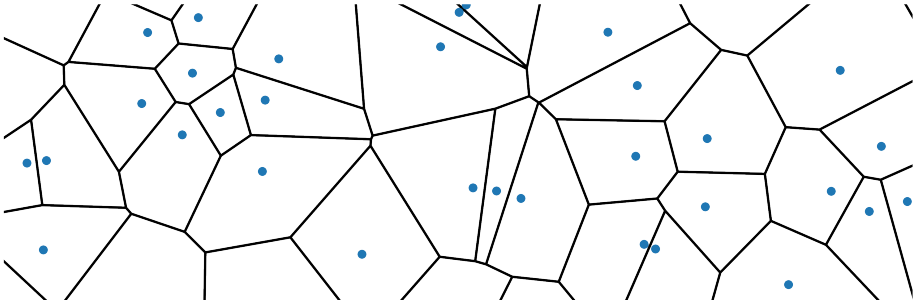

Figure 2.10: An example of a Voronoi tessellation, points representing the lipids of a single leaflet in the XY plane are shown in blue, lines indicate the boundaries of the tessellation, each polygon represents the surface area associated with the lipid it contains

single lipid can be calculated and distributions of values can be generated rather than a single, averaged value as given by equation 2.15. Each lipid is assigned a surface area value of the polygon that contains it in the Voronoi tessellation. A final further extension can be applied in the case of curved and undulating bilayers. Assuming the local area of each lipid is approximately planar, the lipids within this region can be selected. Given the points should lie approximately on a plane, the first two largest eigenvalues correspond to the estimated plane, and the final eigenvector corresponds to the plane normal at this point (Hoppe et al. 1992). By projecting nearby points onto these first two principle components a 2D representation of the lipids on the plane is calculated. Repeating this process for each lipid and its neighbours converts the 3D structure into a series of 2D planes which can be solved using Voronoi tesselation (Buchoux 2016).

The bilayer thickness, T, simply calculated as the distance in Z between the average position of the phosphate atoms, approximating the maxima in the electron density for each leaflet. A more complex analysis can extract additional information by coupling lipids across the bilayer (P. Smith, Quinn, and Lorenz 2020). By pairing each phosphate atom, i, with the nearest phosphate atom in the opposing leaflet in the XY plane, j, the thickness can be calculated for that specific lipid as

$$T_i = Z_{phosphate,i} - Z_{phosphate,j} \tag{2.16}$$

a diagram of this can been seen in Figure 2.11 where each lipid in the top leaflet (orange) is coupled with a lipid in the bottom leaflet (blue) as indicated by the solid arrows.

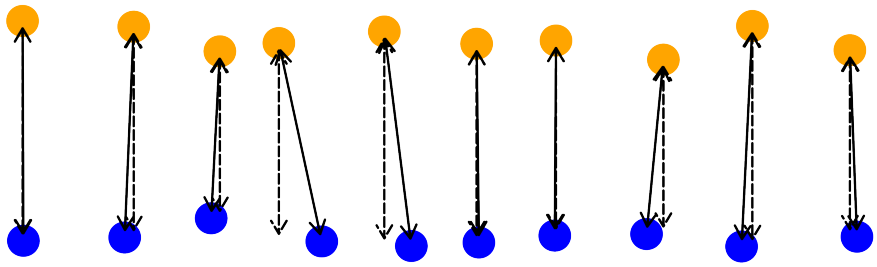

Figure 2.11: Diagram showing the phosphate atoms of a bilayer, the top leaflet (orange) is coupled with the opposing leaflet (blue), the solid arrow indicates a coupling and the dashed arrow represents the Z component of the distance.

The dashed arrow shows the thickness vector.

The advantage of these more complex analysis methods allows for distributions of the value across the bilayer, rather than just the mean bilayer value. These properties can then be tracked for a single lipid over time to track the evolution and/or switching between different states.

Currently unused in studying lipid bilayers, but able to provide a valuable local structural information, a mixed, radial, angular three-body correlation function, $g_3(r_{AB}, \theta_{ABC}) \equiv g_3$, can be seen as an extension of the radial distribution function (RDF), $g(r_{AB})$, a pair correlation function (Sukhomlinov and Müser 2020). Like an RDF, g_3 measures the density of atoms, A at a given distance from a reference atom, B, r_{AB}. Unlike the RDF, the nearest neighbour atom, C, is used to establish an axis and the angle between the atoms, θ_{ABC} is calculated. This generates a distribution which shows additional structural information about the atoms, without providing any criteria ahead of time. An example of this is shown in Figure 2.12, where the central atom, B is shown in black, its nearest neighbour, C is shown hatched and the target atoms are labelled i, j, and k. The distribution is normalised in a similar method to the RDF, whereby an ideal gas has a uniform value of 1. The angular component allows the differentiation of structural detail such as trans-gauche isomerisation.

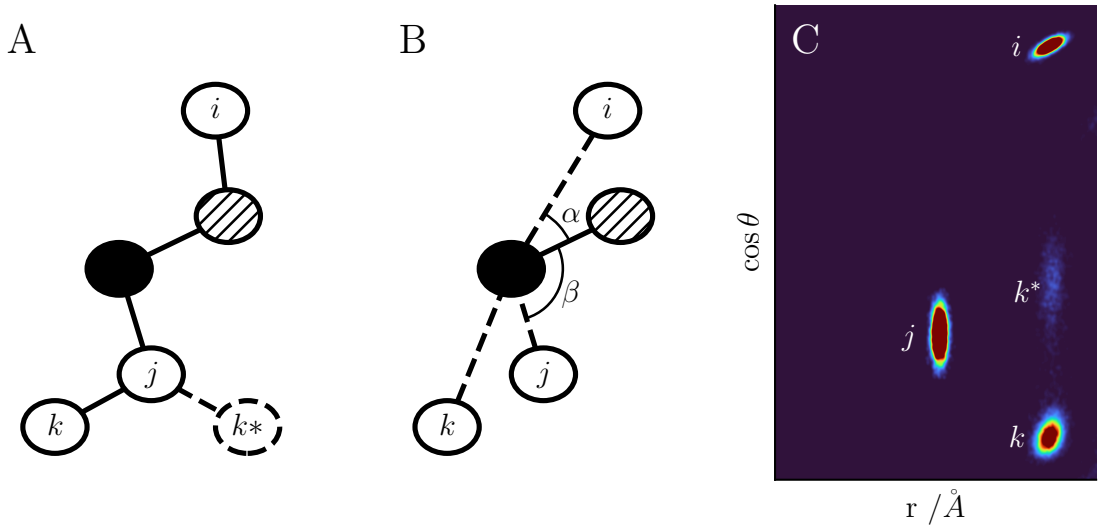

Figure 2.12: A shows a section of lipid tail centered on a single central carbon (black fill) with its nearest neighbour carbon (hatched), k has been shown twice in two possible conformations. The connecting lines represent bonds. B shows the angles between the nearest neighbour carbon, central carbon and each nearby atom. Only the angles involving i and k have been shown for simplicity. The connecting lines are not bonds but indicate a side of the triangle formed by the atom, the central atom, and the nearest neighbour atom. C shows the respective g_3 distribution with the contribution of each atom indicated. Small angles (α) formed by atoms on the nearest neighbour side of the chain, such as i, occupy the top of the distribution. Large angles (β) formed by atoms on the far side of the chain from the nearest neighbour, such as j and k, are on the bottom. Conformational changes mean a single atom can contribute to multiple peaks, $k*$ is the contribution of the atom k in a gauche conformation, shown in A as the dashed atom. The nearest neighbour does not contribute to the distribution.

Chapter 3. Phase separation of naked mole-rat lipid bilayers

3.1 Summary

The membrane pacemaker hypothesis proposes the composition of the cell membrane is a key factor in the ageing of an animal. This theory predicts the composition of lipid membranes is key to ageing by influencing the amount of peroxidation of the lipids. Longer-lived animals have less unsaturated lipids which are susceptible to peroxidation. In this chapter, atomic force microscopy was used to assess supported lipid bilayers derived from cells originating from naked mole rat organ cell lines. These were compared with DOPC/DPPC and mouse cell line supported lipid bilayers. Naked mole-rat cell line lipids exhibited a high degree of phase separation and the different phases showed different mechanical properties. Inducing peroxidation in the naked mole-rat lipids restructured the rafts or slightly fragmented the supported lipid bilayer. The naked mole-rat lipids are more susceptible to peroxidation induced damage than mouse lipids.

3.2 Introduction

The cell membrane is comprised of a complex mixture of lipids and proteins and the 2D lateral ordering and phase behaviour of such complex mixtures may vary considerably from that of simplified model systems (Harayama and Riezman 2018). It has been hypothesised that long lived animals, such as the naked mole-rat (NMR) (Buffenstein 2008), may have unique compositions of their cell membrane in terms of lipids and fatty acids, that may account for their longevity (A. J. Hulbert, Faulks, and Buffenstein 2006; T. W. Mitchell, Buffenstein, and A. Hulbert 2007).

This membrane pacemaker theory of ageing has considerable experimental verification, across a range of animals including humans, and theorises that the membrane composition of long lived species are tuned to resist lipid peroxidation, a process of damage accumulation that occurs during ageing (Calhoon, Ro, and Williams 2015). The theory predicts that the longevity in animals are a result of having less unsaturated

lipids, which are less susceptible to lipid peroxidation. These lipids are linked with raft formation and phase separation in lipid bilayers (Wassall and Stillwell 2009). NMR seem to have high resistance to the effects of peroxidation.

Young NMRs have high levels of oxidative stress markers, compared with mice, despite their increase longevity and peroxidation resistant lipid composition (De Waal et al. 2013; Edrey, Oddo, et al. 2014). It is in this context that the phase behaviour and morphology of NMR derived lipids will be investigated by atomic force microscopy (AFM), a technique that has been applied to model systems (Attwood, Choi, and Leonenko 2013; Milhiet et al. 2002; Schneider et al. 2000) and commercially available porcine derived lipid extracts (e.g. J. Lee, Kim, et al. 2017; Mrdenovic et al. 2019; Mari et al. 2018). In addition, an in vitro lipid peroxidation assay will be applied to follow the peroxidation process via AFM on supported lipid bilayers (SLBs), in order to observe whether differences exist in peroxidation resistance between the long lived NMR and the short lived mouse.

3.3 Methodology

AFM experiments were undertaken on an Agilent 5500 with a closed loop scanner, using a liquid cell to keep the SLBs hydrated. All experiments were carried out at 20 °C. Tapping and contact mode images were obtained using aluminium coated cantilevers (PPP-NCSTR and PPP-CONTR, Apex Probes, UK respectively). All contact mode cantilevers had a nominal spring constant of between 0.02 and 0.77 Nm^{-1} with a tip radius of less than 7 nm.

3.3.1 Supported lipid bilayer preparation

The two model membrane lipids, dioleoylphosphatidylcholine (DOPC) and dipalmitoylphosphatidylcholine (DPPC) (Avanti Polar Lipids), were dissolved in chloroform in a 3 to 1 molar ratio and dried under nitrogen, then re-suspended in ultrapure water to a final concentration of 1 mg/ml and vortexed. The animal organ cell-line derived lipids (mouse skin, NMR skin, NMR kidney and NMR lung) were dried down to form a film and then re-suspended in ultrapure water. Uni-lamellar vesicles were formed via ten cycles of freeze-thawing followed by extrusion ten times through a polycarbonate membrane with pores sizes of 100 nm using a mini-extruder (Avanti Polar Lipids) kept 50 °C on a hotplate. 200 μl of solution containing the extruded vesicles was pipetted onto freshly cleaved muscovite mica and this was then placed on a thin metal disk that

itself was placed on a hotplate at 50 °C and the sample was annealed for 15 minutes. The sample was rinsed thoroughly via repeated partial solution exchange, ensuring the samples always remained hydrated. The sample was then loaded into the AFM liquid cell ready for imaging. When imaged in contact mode, a confirmation indentation and successful breakthrough event were recorded to confirm the presence of bilayer before proceeding with imaging. This is not possible in tapping mode so where in doubt, after imaging, a contact mode tip was used to perform an indentation and confirm the existence of the bilayer.

3.3.2 Force spectroscopy

Indentations were made using the contact mode tips. The measured spring constant of tips used were all measured in the range 0.05-0.18 $\mathrm{N m^{-1}}$. Indentations were targeted by first imaging the area at low resolution to identify phase separated regions then taking indentations of the areas separately. The tip indentation speed was 1 $\mu\mathrm{m\,s^{-1}}$. Breakthrough events were detected and the breakthrough force was calculated using an automated method (J. K. Li, Sullan, and Zou 2011).

3.3.3 Lipid bilayer peroxidation

To induce lipid peroxidation into the SLBs $100\mu M$ of iron sulphate and ascorbic acid were introduced to the liquid cell after confirmation of the existence of a suitable bilayer via indentation and basic imaging. This was left to allow peroxidation to initiate before being removed via repeated partial solution exchange. Peroxidation levels were varied by altering this initiation stage time. The peroxidised bilayers were then left 22 hours before being rinsed again and imaged in the AFM.

3.3.4 Analysis

Images were loaded and plane corrected by fitting and subtracting a third order polynomial. For each analysis multiple images were analysed from at least 3 separate SLB preparations. Phase coverage was determined by estimating the probability density of each phase as a Gaussian curve. Fitting the sum of two Gaussian curves to the probability density, f, of height values, z,

$$f(z) = g_1(z) + g_2(z) \tag{3.1}$$

where the g_i is a single Gaussian function,

$$g_i(x) = A_i \exp\left(\frac{-(x-\mu_i)^2}{2\sigma_i^2}\right) \tag{3.2}$$

where A is the peak height, μ is the peak location and σ is the peak standard deviation of the Gaussian curve.

The coverage of each phase of lipids is then calculated as the integral of the respective terms,

$$C_i = \int g_i(z)\, dz \tag{3.3}$$

which due to being fit over probability density, and assuming a successful fit to the bimodal data of phase separated height measurements

$$C_1 + C_2 \approx 1 \tag{3.4}$$

Raft height determination was calculated by segmenting the images into smaller sections to localise the height difference measurements and the histogrammed probability density of height values was calculated. Equation 3.1 was fit to the small segmented region and the height difference of the segment was calculated as

$$\Delta z = |\mu_1 - \mu_2| \tag{3.5}$$

Breakthrough force was calculated by fitting a Gaussian distribution (equation 3.2) to the histogrammed breakthrough force values from a series of indentations.

3.4 Results

3.4.1 Extensive phase separation of naked mole-rat supported lipid bilayers

Complex SLBs display phase separation when imaged with AFM. A simple model example of this is the 3:1 molar ratio of DOPC/DPPC, Figure 3.1. This phase separation exists because localised heterogeneity in lipid concentration across the bilayer. Differences in tail packing within the lipids of each region lead to lipids with more ordered tails, standing taller and protruding slightly from the rest of more disordered lipid bilayer. Panel B shows a schematic of this, with the disordered DOPC rich region lipids at the lower height values, shown in blues, and the more ordered DPPC rich regions, shown in reds, at the higher height values. When calculated across multiple images and sample preparations the raft height was calculated as 0.96 ± 0.07 nm this is

consistent with reported DOPC/DPPC bilayers which have raft heights of 0.97 ± 0.14 nm reported (Milhiet et al. 2002) and importantly different than the expected height of an incomplete broken bilayer at 5 nm (Attwood, Choi, and Leonenko 2013). The surface coverage of rafts across the images was 28.82 ± 3.35 %, consistent with the fact the phase separation is into DPPC-rich and DOPC-rich regions with the minor component being the higher, DPPC-rich regions.

An example of the local segment of an image analysed of the DOPC/DPPC bilayer is shown in Figure 3.2. Without localisation of the analysis the height value is not representative as the plane correction is not exact so there can still exist some 'tilt' in the image data. This planar 'tilt' is not insignificant over larger distances, this can be seen in the line profile in Figure 3.1 where the profile drifts to higher z values as it goes to the right of the figure. An alternative method would be to analyse these line profiles, manually selecting points on the ordered/disordered interface.

Similarly to the DOPC/DPPC bilayer extensive phase separation is exhibited in NMR skin derived lipids, shown in Figure 3.3. The raft morphology is more complex than in the binary mixture of DOPC/DPPC with small pockets of disordered lipids within the more ordered rafts. The size of the rafts is more varied than in the binary mixture with both large and small rafts visible. These rafts have a similar raft height to the DOPC/DPPC at 0.99 ± 0.09 nm but the variation in surface coverage is much greater than the binary mixture, having a surface coverage of 43.55 ± 15.39 %. This is probably due to the more complex morphology structure compared with the more uniform rafts in DOPC/DPPC. The spatial distribution of the rafts also seems key, in the example shown the rafts are much more sparse in the bottom right corner. The difference between the binary model and the derived lipids is in the complexity of the mixture. The binary system only had two components with the same headgroup, differing in their tails, saturated DPPC and unsaturated DOPC. In cell extracts the number of lipid components is much larger, with a phospholipid composition comprising mostly of four main classes of phospholipid based on their headgroup (PC, PE, PI, PS). Alongside the bulk phospholipids in a mammalian cell also present and key are sphingolipids, like sphingomyelin, and sterols, like cholesterol (van Meer, Voelker, and Feigenson 2008). These classes each contain a distribution of tails both saturated and unsaturated and of varying lengths and asymmetries that can occur, leading to orders of magnitude more unique molecules in the final complex mixture (Brügger 2014).

In comparison to the NMR skin, mouse skin lipid supported bilayer, shown in

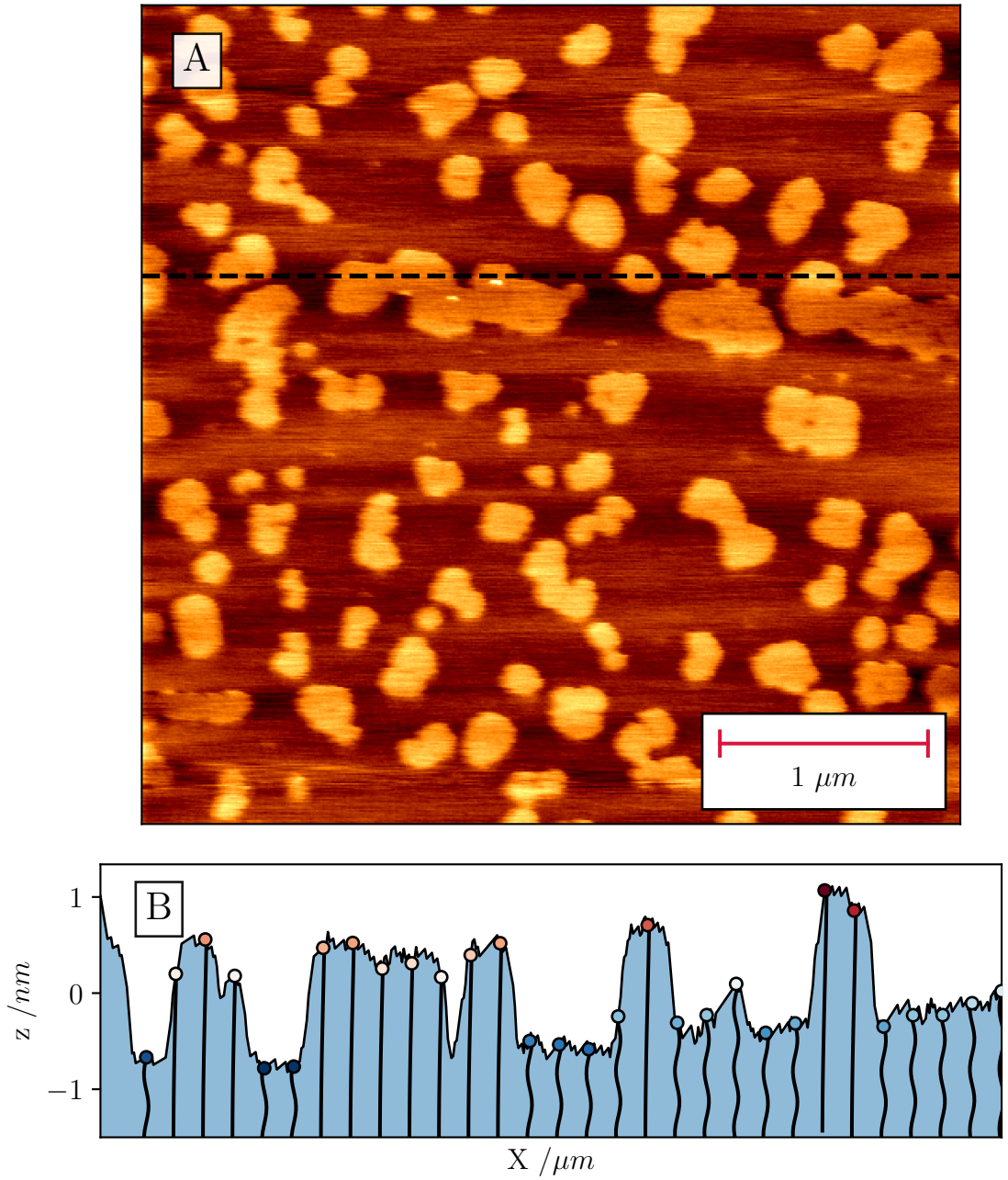

Figure 3.1: Contact mode image of a 3:1 molar ratio DOPC/DPPC SLB showing phase separation (A). A schematic of the relationship of this phase separation, tail disorder and raft height is projected onto a line height profile (B). This image has a raft coverage of 30% and a raft height of 0.98 nm.

Figure 3.2: Contact mode image of a one of the segments analysed for determining raft height in the DOPC/DPPC SLB (A) with a binary mask applied (B) based on the z value indicated in the probability density of z values (C). The two Gaussian fits have been indicated with black dashed lines. The binary mask is shown for confirmations of raft identification only and not used in calculations further.

Figure 3.3, has obvious differences. The degree of phase separation is significantly lower, while there is still a small amount of phase separation occurring but no where near to the level of that in the phase separated naked-mole rat or model DOPC/DPPC bilayers. The mouse skin has a phase separation of just $1.79 \pm 0.24\,\%$. The raft height is $0.84 \pm 0.15\,\text{nm}$.

Lipids derived from other organs in the NMR also show this high extent of phase separation. Kidney derived lipids, shown in Figure 3.4, feature a ring like structure. The average raft height was $1.18 \pm 0.21\,\text{nm}$. Like the NMR skin the kidney lipids have a high degree of phase separation with $46.1 \pm 6.0\,\%$.

Lung derived lipids have a three tiered separation, with a major phase and a minor protruding and inset phase. Although this did not occur in all samples. Excluding these 'complete' raft bilayers from the phase coverage analysis lead to the highest phase separated bilayers, with a coverage of $64.9 \pm 2.8\,\%$ and a height of $1.19 \pm 0.23\,\text{nm}$.

3.4.2 Mechanical properties of the different lipids phases

Since phase separation is shown, to varying extents, in both mouse and NMR lipid bilayers, indentations were made to attempt to quantify the differences in these domains. In the low phase coverage mouse bilayers the indentations are able to detect two characteristic breakthrough forces, shown in Figure 3.7. As reported in literature

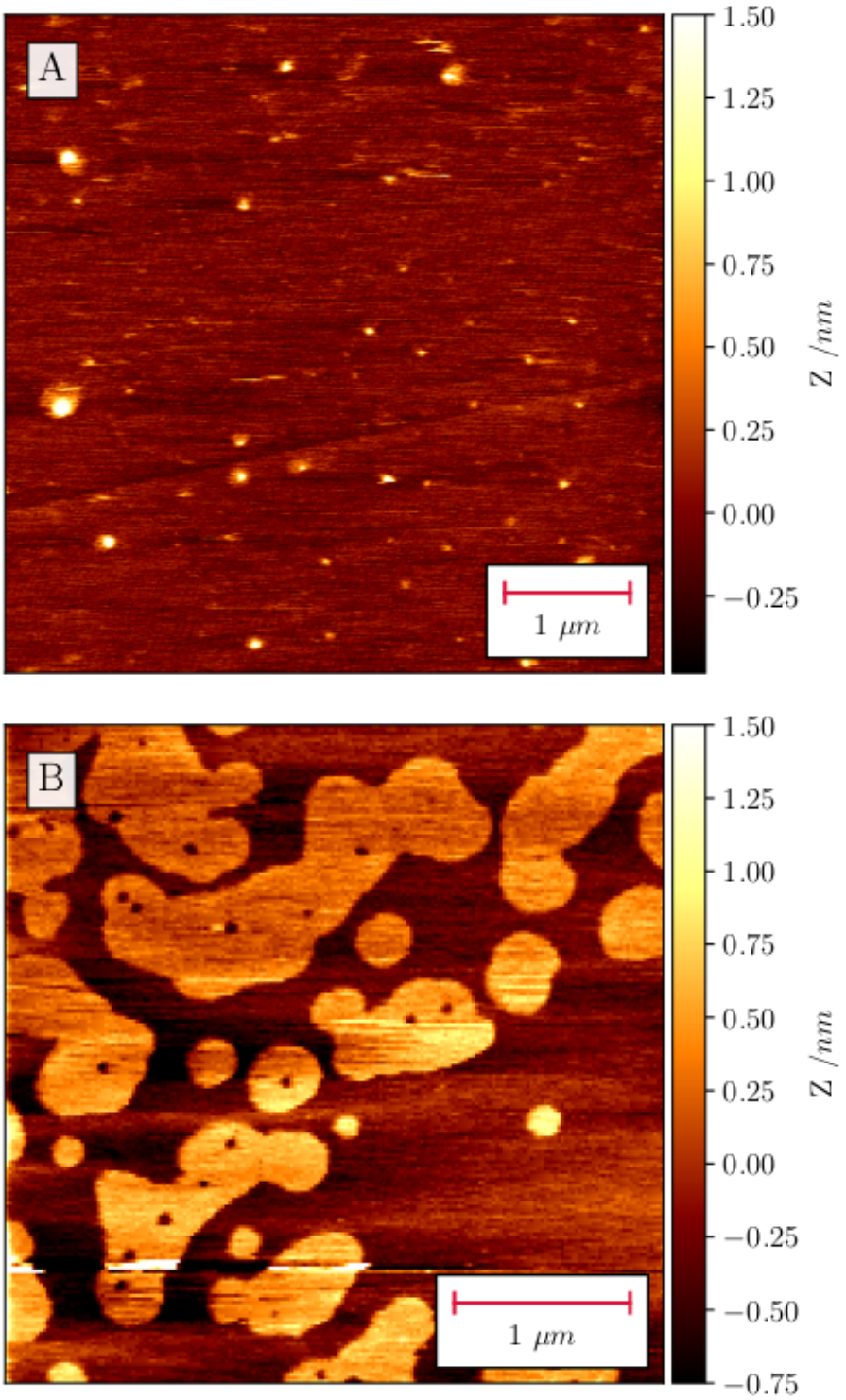

Figure 3.3: Contact mode image of a mouse (A) and NMR (B) skin lipid extracted SLBs. Extensive phase separation can be seen in the NMR bilayer which is not present in the mouse lipids.

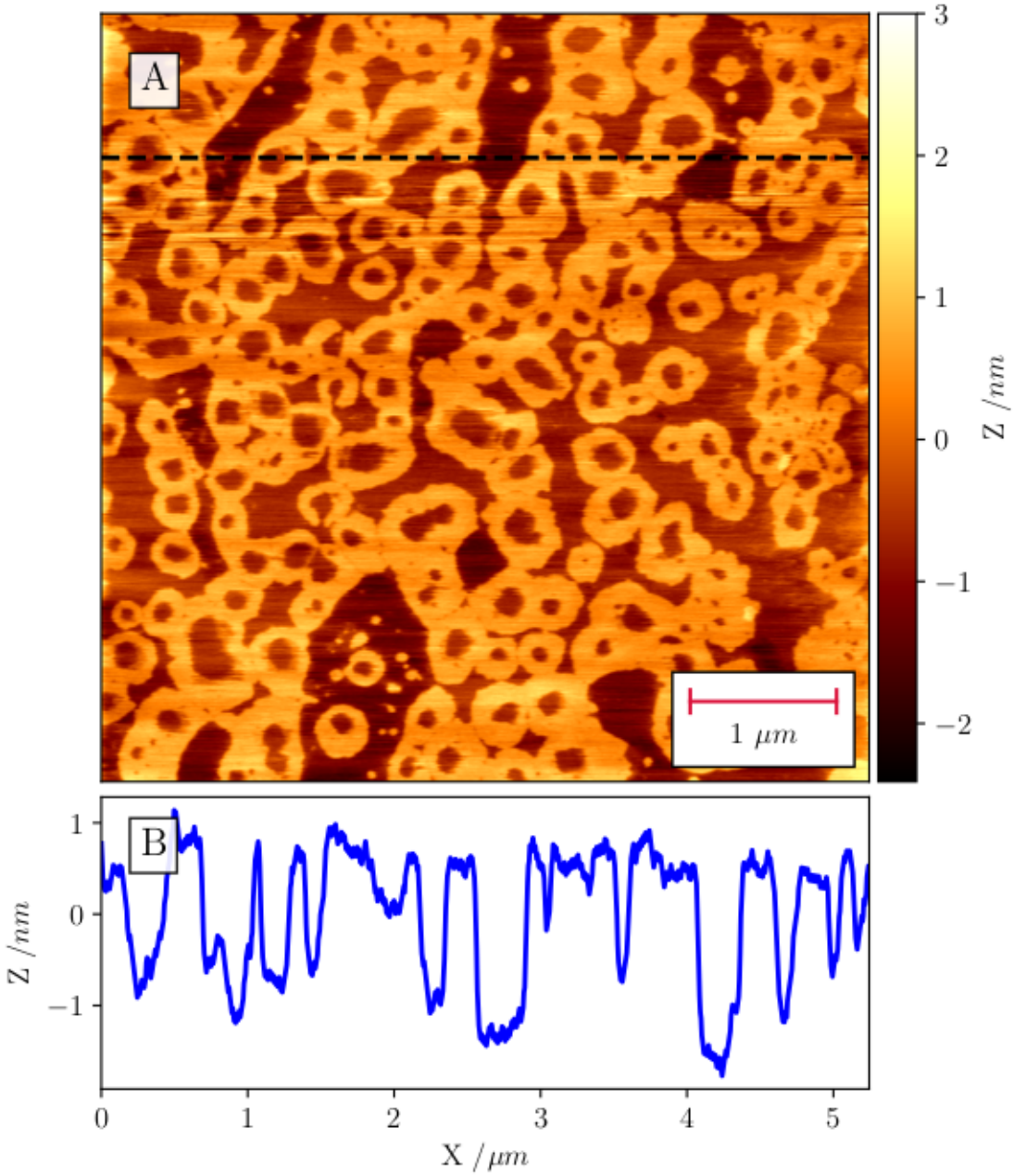

Figure 3.4: Contact mode image of a NMR kidney lipid extracted SLB (A) and a line profile of the extensive phase separation (B). A complex ring morphology can be seen with lots of pockets of disordered lipids encircled by the rafts.

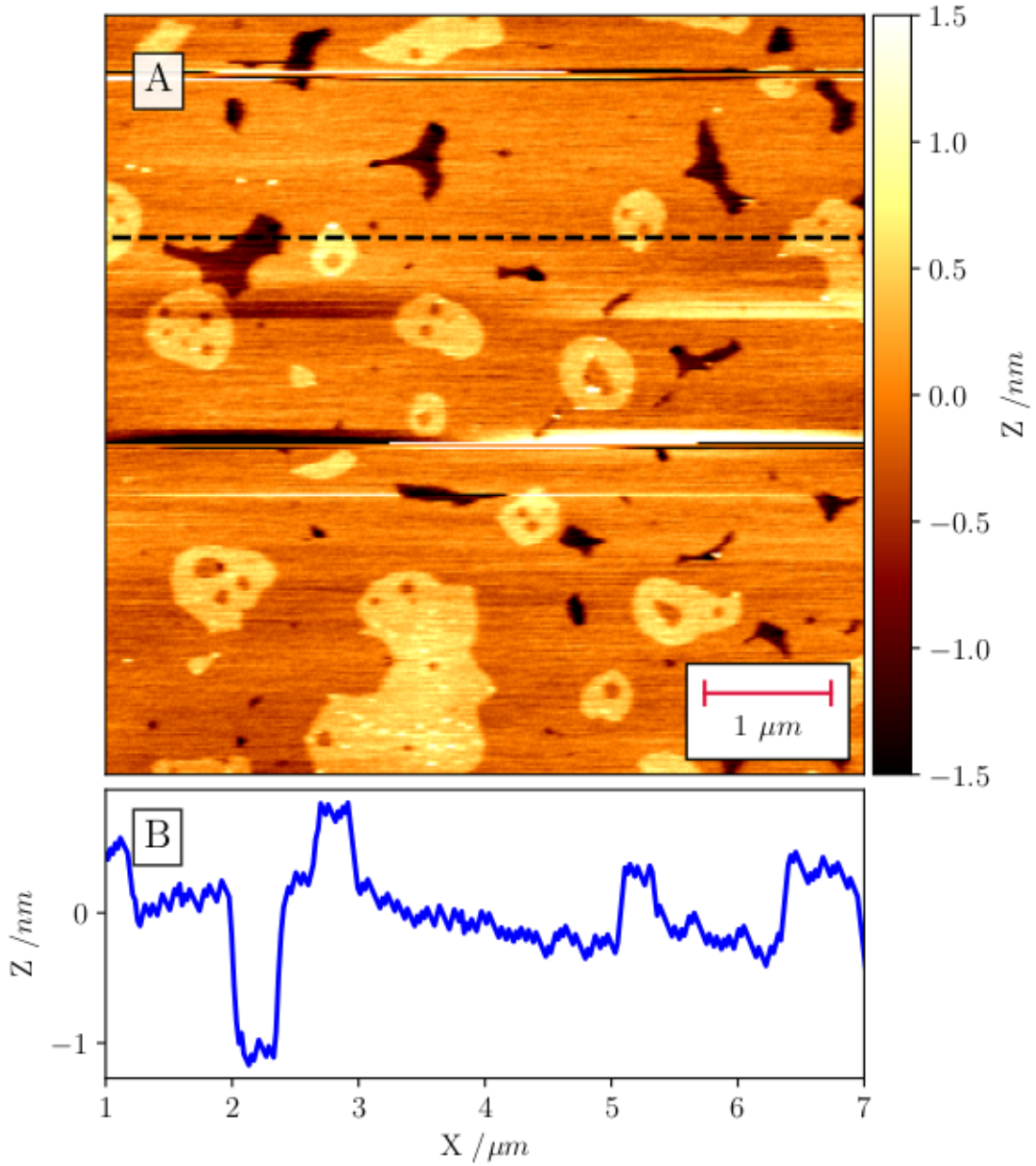

Figure 3.5: Contact mode image of a NMR lung lipid extracted SLB (A) and a line profile of the extensive phase separation (B). A three tiered phase separation can be seen with a minor component of a lower phase, with heights consistent with that of raft, a major phase of rafts and further ordered rafts within the major phase, standing 0.5 nm above that.

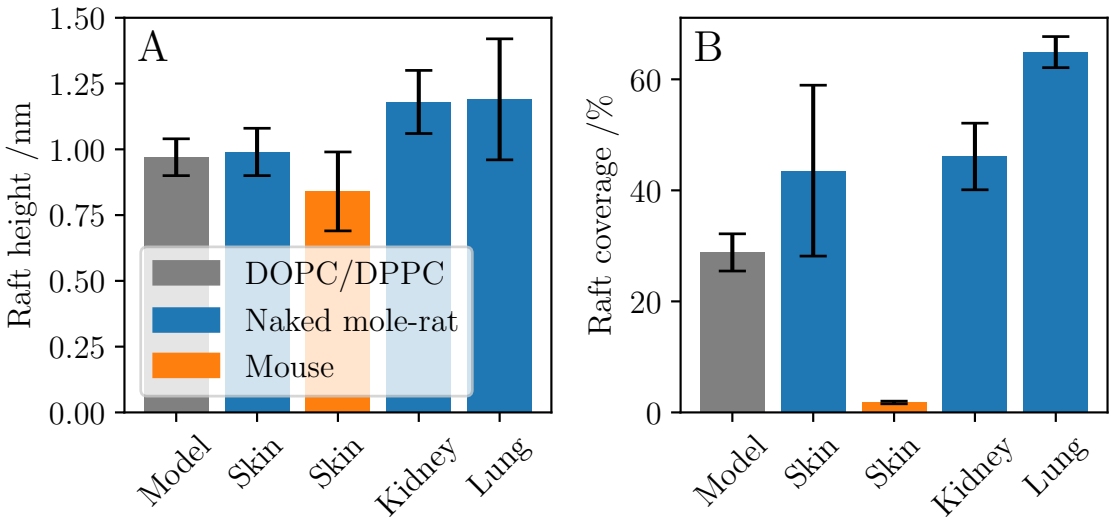

Figure 3.6: Raft height (A) and coverage (B) comparison between the different systems analysed. The raft heights are consistent across the samples, but the coverage amounts are vastly different with NMR having significant amounts of phase separation where mouse have very little.

differences in the breakthrough force as a result of the phase difference is apparent. The stiffer, more ordered rafts have a much higher breakthrough force than the more fluid disordered lipids.

When attempting the same on the highly phase separated NMR lipids, shown in Figure 3.8, a similar double set of peaks appears, however they do not successful split based on targeted indentations based on the image. This is likely because it is more difficult to accurately target the more crowded rafts from the less well defined surrounding disordered phase.

The NMR indentations were assumed to be 'leaky' and the data was aggregated and fit to the sum of 2 Gaussian distributions.

This leakiness can be seen to a minor degree in the distributions for the mouse indentations in Figure 3.7, with a small subset of breakthrough forces in the other phase region of values. This aggregated is much more consistent with the mouse bilayer result. Applying this data aggregation method to the mouse data does not substantially change the result of the fitting (table 3.1).

In both animals the ordered and disordered lipids have a differing breakthrough force. Between animals though the difference between phases is not significant.

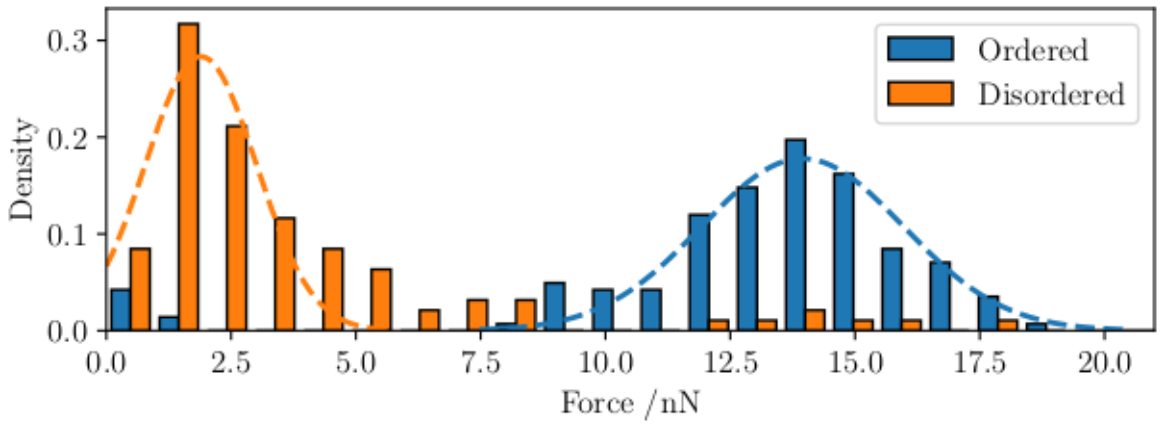

Figure 3.7: Breakthrough force following targeted indentations into the disordered and ordered sections of a mouse SLB. The ordered and disordered phases have a breakthrough force of 13.95 ± 2.02 nN and 1.89 ± 1.11 nN respectively. A total of 147 breakthrough events were recorded for ordered phase and 97 breakthrough events for the disordered phases.

Fit type	$F_{\text{disordered}}$ /nN	F_{ordered} /nN
Separated	1.89 ± 1.11	13.95 ± 2.02
Combined	1.73 ± 1.28	13.95 ± 2.03

Table 3.1: Fit breakthrough force for the mouse skin lipid targeted indentation data, keeping the data separated as ordered and disordered, and merging the data to a single collection

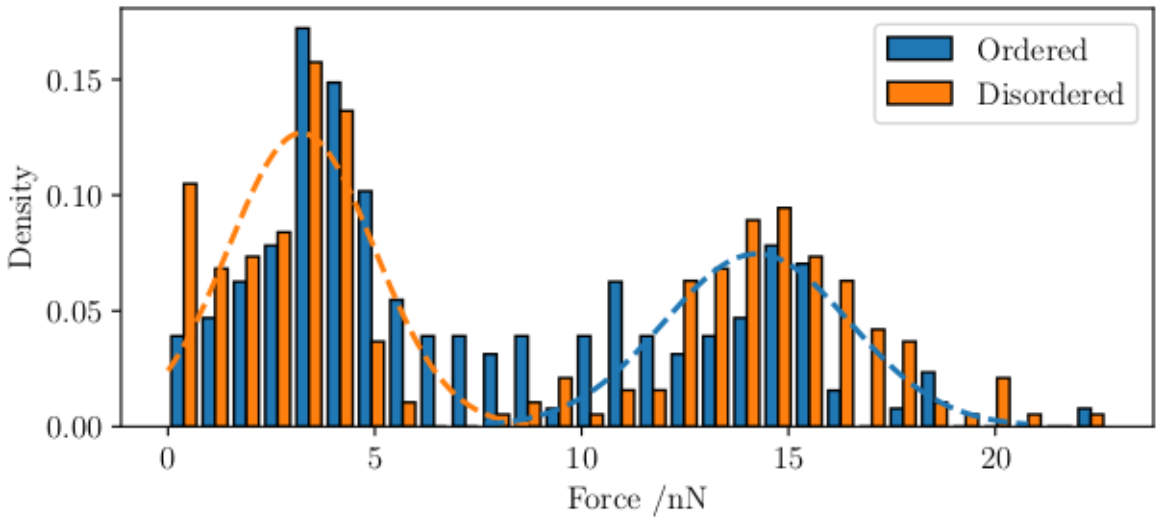

Figure 3.8: Breakthrough force following targeted indentations into the disordered and ordered sections of a NMR SLB. The targeted indentations have not managed to successfully separate the two phases so the data was aggregated and the sum of two Gaussian curves (similar to equation 3.2) were fit to the aggregated data. The ordered and disordered phases have a breakthrough force of $14.23 \pm 2.24\,\mathrm{nN}$ and $3.22 \pm 1.77\,\mathrm{nN}$ respectively. A total of 169 breakthrough events were recorded targeting the ordered phase and 252 breakthrough events targeting the disordered phases.

Importantly the average breakthrough force will differ, this is measuring via targeted indentations and not a system average. As has been shown in Figure 3.3 the phase separation in mouse lipids is to a much smaller degree than in NMR lipids.

3.4.3 Peroxidation induced damage of lipid bilayers

An interesting hypothesis is that either the composition or degree of phase separation will influence the degree of resistance to lipid peroxidation, and thus these differences may manifest between NMR and mouse samples.

Lipid peroxidation is a free radical driven process, once initiated the products of the reaction are able to propagate the reaction further. The key being once initiated the lipid peroxidation products (LPP) can initiate peroxidation in new lipids. Differing lipid bilayer properties and compositions might be able to hinder or accelerate this process, for example by decreasing the diffusion of the LPP, keeping propagated peroxidation more localised. Lipid peroxidation occurs in the acyl-tails, if the bilayer itself has lower permeability to peroxidation inducing species this could have a passive protective effect.

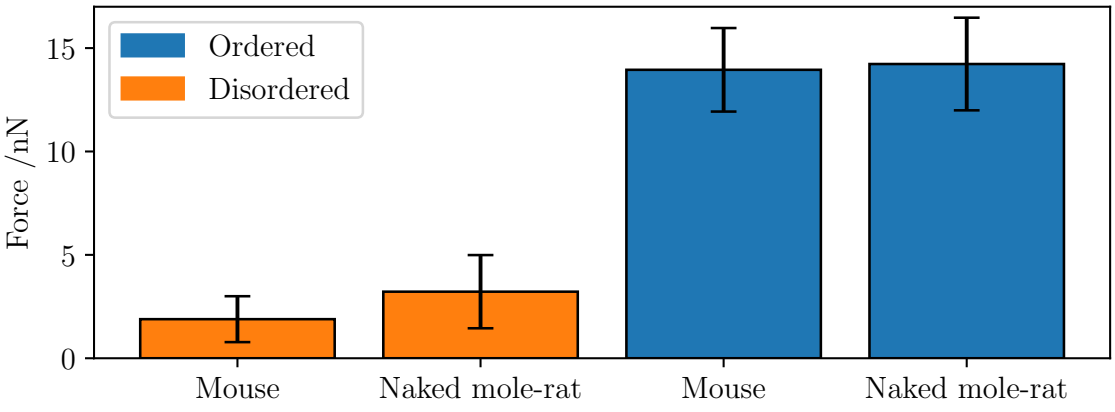

Figure 3.9: Breakthrough force distributions compared. The ordered and disordered lipids values differ but between animals the ordered and disordered regions have consistent breakthrough forces.

Since a lipid bilayer is not a perfectly mixed solution, but a quasi two dimensional layer, with the acyl tails on its interior, the peroxidising molecules (including the LPP) exposure to acyl-tails might be minimised.

At lower exposure of peroxidising agents the bilayers are able to remain in tact but feature a reorganisation of the lipids, with the ordered phase breaking apart, enveloping and surrounding regions of the disordered phase (Figure 3.10).

At higher peroxidation levels the bilayer is damaged rather than restructured (Figure 3.11). The height distribution of the higher peroxidation bilayer is consistent with that of a damaged lipid bilayer showing underlying mica (panel A). The remaining lipids, while damaged, are largely continuous with small but consistently spread patches of damage showing the underlying mica (panel B). The restructured rafts from the lower peroxidation are do not have a height profile range near that of a complete bilayer, instead consistent with phase separation (panel C). The lipids form a three tiered structure (panel D), like seen before peroxidation, especially visible in Figure 3.5. In the case of the restructured lipid though the intermediate height phase has given way to much more of the lower height phase.

This peroxidation induced restructuring occurs on a large scale over which no signs of damage can be seen (Figure 3.12). Across the entire large range no defects that would indicate severe damage can be seen.

In comparison to the NMR, where restructuring and destruction depend on the exposure time. Where the NMR bilayers show signs of peroxidation at both the

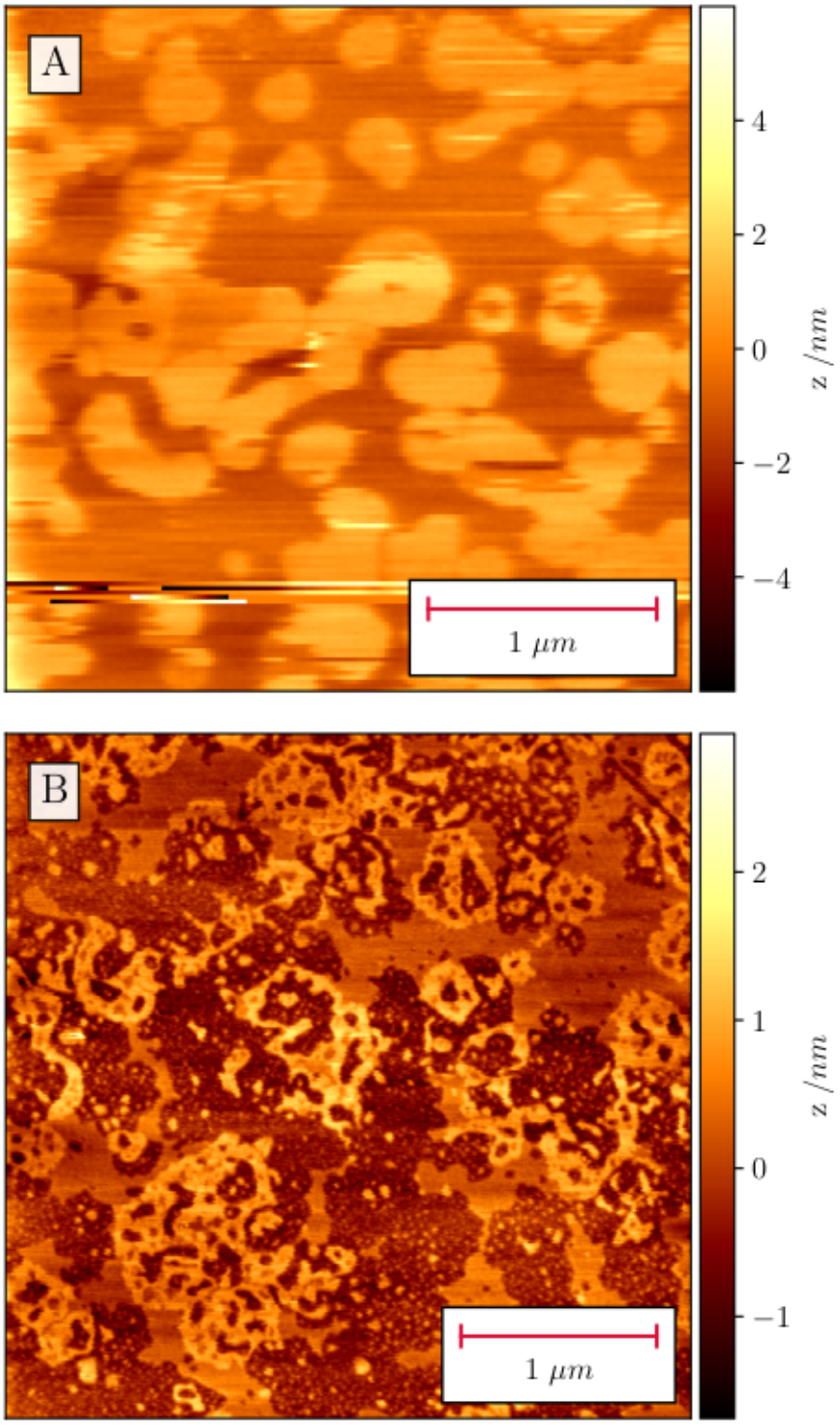

Figure 3.10: NMR lung lipid bilayer images before peroxidation (A) and after restructuring due to peroxidative damage (B).

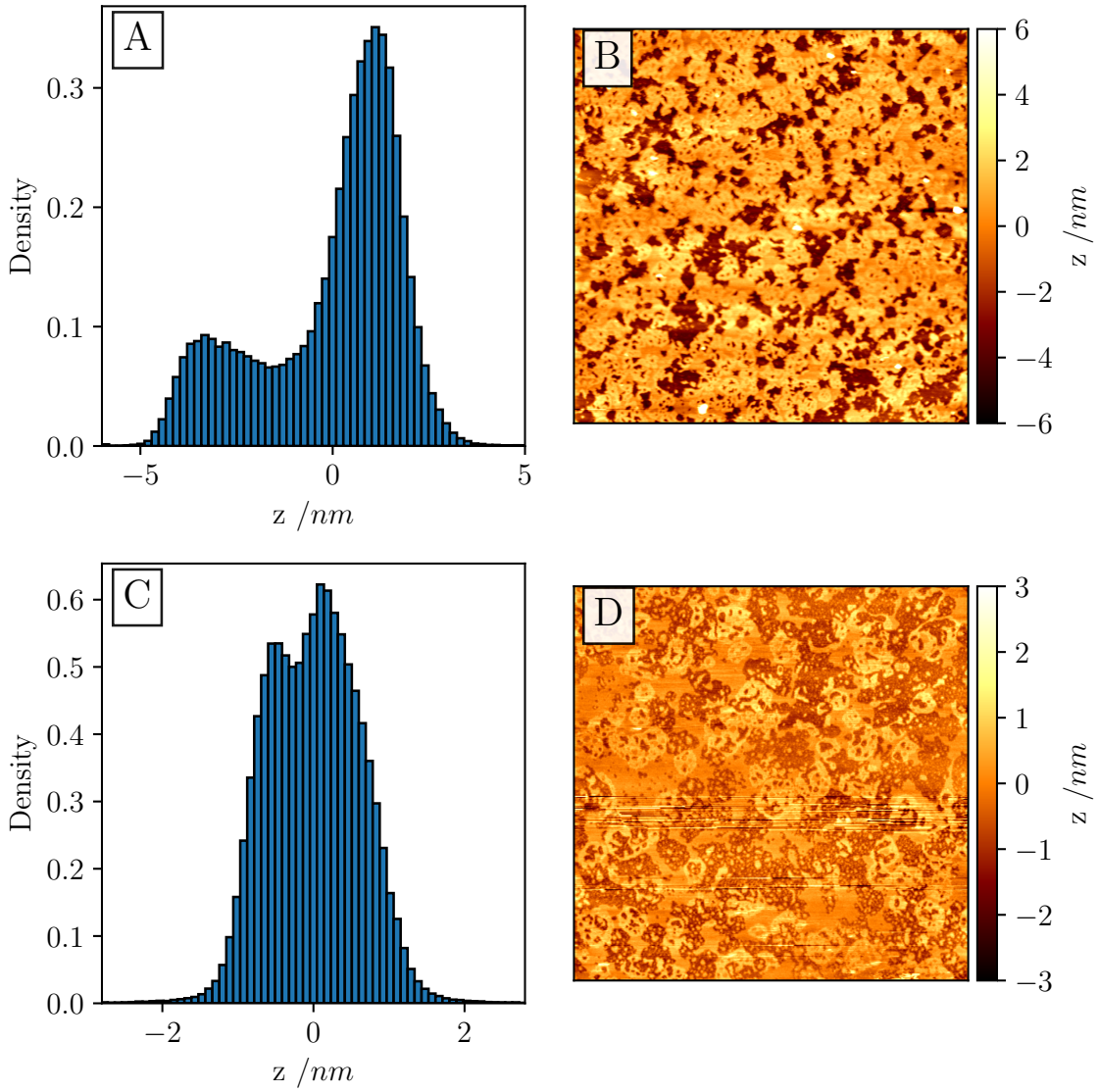

Figure 3.11: Height distribution of a fragmented peroxidised NMR lung lipid bilayer (A) and a tapping mode image of the fragmented bilayer (B). At lower exposure times the bilayer is able to remain in tact (D) with a height distribution (C). The fragmented bilayer is broken as shown by the $\sim 5\,\mathrm{nm}$ difference in peak heights where the intact bilayer does not, showing a raft like height difference.

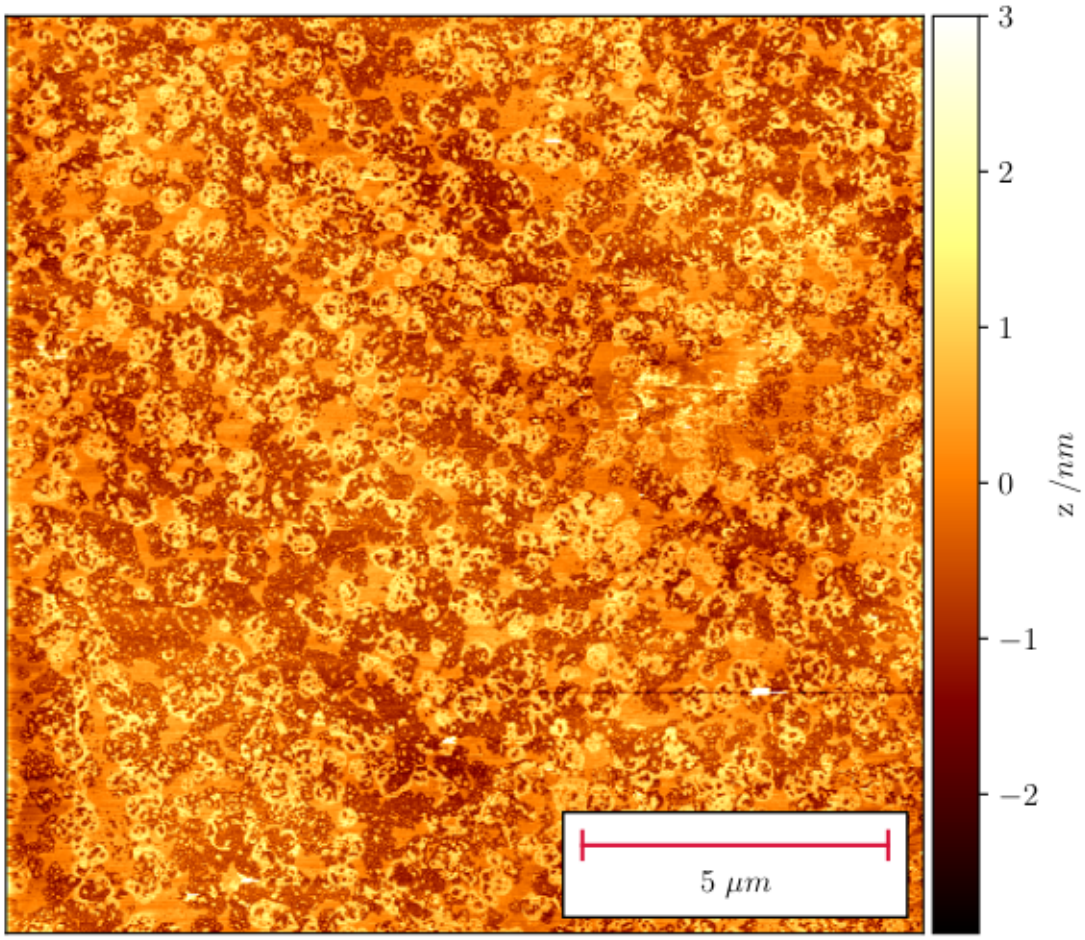

Figure 3.12: Remodelling of NMR lung lipid bilayer occurs on a large scale

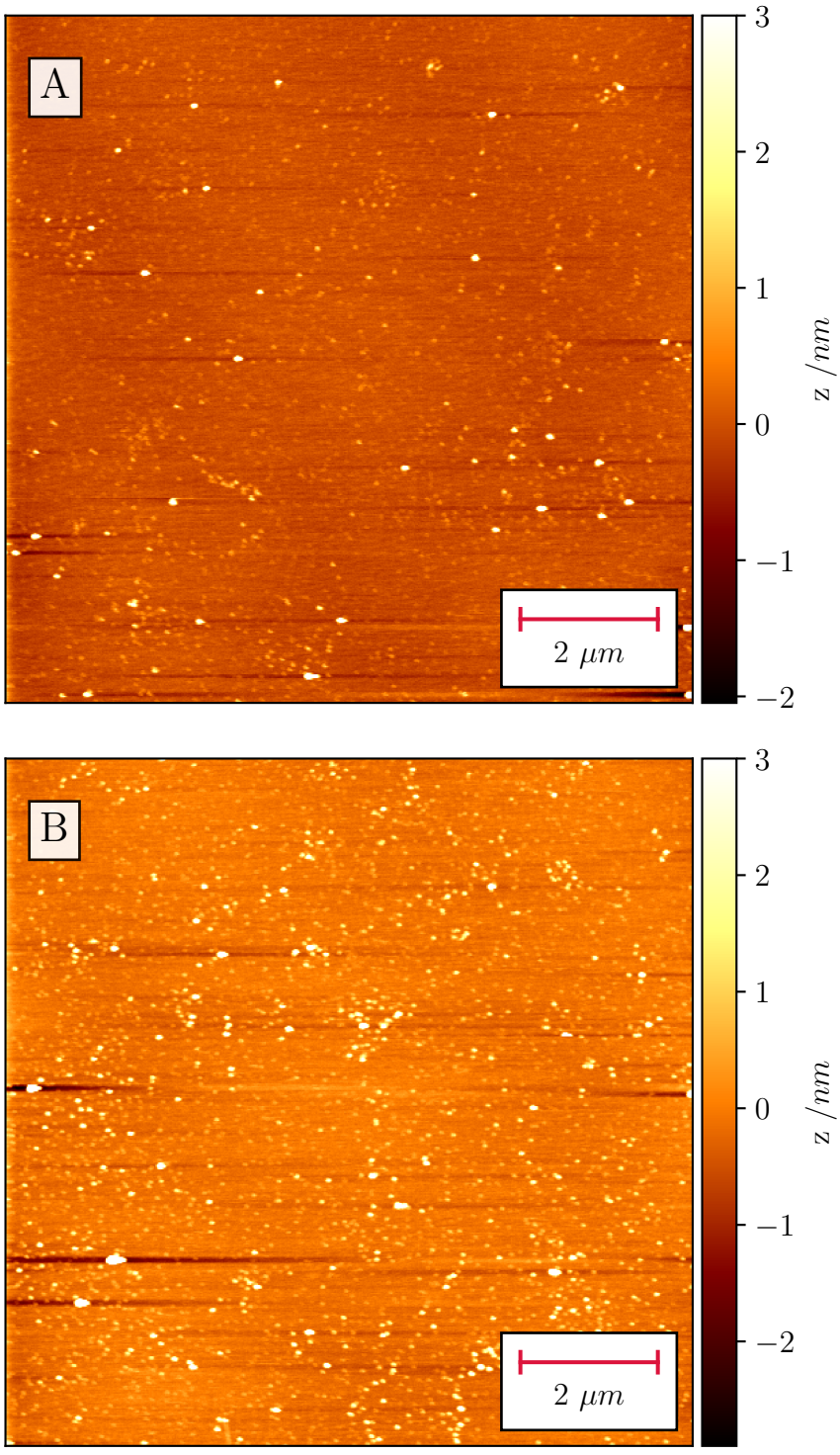

Figure 3.13: Tapping mode image of mouse skin lipid bilayer before (A) and after (B) peroxidation. There is very little change in the bilayer which does not break or fragment.

lower and higher peroxidation, restructuring and developing holes respectively, the comparative mouse system appears highly resistant to peroxidation induced changes.

Figure 3.13 shows mouse skin exposed the same as the damaged bilayer shown in Figure 3.11B. The bilayer remains entirely intact. There is an increase in the small point like rafts but no drastic restructuring and no signs of fragmentation or serious damage as seen in the NMR. The existence of the bilayer following was confirmed by switching to a contact mode tip and measuring breakthrough events across the surface.

3.5 Discussion and conclusions

Phase separation in SLBs can be observed in model membranes such as DPPC/DOPC (Figure 3.1). Although this is common in model membranes, in SLBs derived from animal cell extracts such as mouse skin (Figure 3.3A) or even in commonly used commercially available lipids such as porcine brain total lipid extracts (J. Lee, Kim, et al. 2017; Mrdenovic et al. 2019; Mari et al. 2018) this is rarely seen. With either no or a very small degree of phase separation visible ($< 2\%$ in the mouse skin).

In contrast with the mouse lipids, NMR lipids extracted from skin (Figure 3.3B), kidney (Figure 3.4) and lung (Figure 3.5) show complex and extensive phase separation ($> 40\%$) in all SLBs.

The phase separation is extensive covering large regions of the bilayers and in the case of each organ a different morphology is seen.

Large rafts in the skin lipids, ring like rafts in the kidney lipids with rafts encircling regions of disordered lipids, and a three tiered phase separation with a majority phase featuring both protrusions of a higher phase, and cavities of a lower phase. Height differences between the lower height and major phase are consistent with the disordered/raft phase seen in other lipid preparations, with the protruding phase appearing to be new.

The rafts themselves, with the exception of the lung lipid protrusions, do not differ drastically, with all rafts detected standing approximately 1 nm high from the disordered lipid background. This confirms these are phase separation features and not damaged bilayers, as the expected bilayer height would be 5 nm (Attwood, Choi, and Leonenko 2013).

While the morphology and coverage of the rafts differs between the two animal skin lipid samples, the rafts themselves have similar mechanical properties (Figure 3.9). While the mouse indentations into specific phases were mostly successful (Figure 3.7), the NMR data was 'leaky' and had to be pooled and refit, applying this same procedure to the mouse data did not give significantly different results.

Indentations into the bilayer were able to show that for different animal sources rafts did not have differences in breakthrough force, although the large amount of phase coverage in NMR lead to leaky indentations, proving difficult to isolate the two phases like in the much lesser separated mouse bilayers.

NMR lipids have a much higher breakthrough force because of the increased raft coverage, not because a difference in raft breakthrough behaviour.

When lipid peroxidation is induced in the highly phase separated NMR lung lipid bilayers damage is induced, although large portions of the bilayer remain intact and continuous, there are nonetheless holes through to the underlying mica (Figure 3.11). The lipids themselves do not show any innate resistance to the damage from peroxidation, although the fact that the bilayer is not totally fragmented and damage seems localised to small regions might allow for repair via an active mean sure as synthesis of new lipids.

Left over time this damage remains, the lipids themselves have no mechanism to repair or reorganise following peroxidation to avoid peroxidation related holes to the bilayer. The degree of peroxidation is however very minor which might explain the ability of the NMR to deal with a high oxidative stress load through active means such as additional lipid synthesis to repair the damage.

The level of peroxidation able to fragment and destroy the NMR bilayer did not damage a mouse comparison (Figure 3.13). At lower peroxidation levels the named mole-rat lipids showed drastic remodelling with raft morphology and coverage changing during peroxidation, going from round, complete rafts, to thin, ring like rafts surrounding disordered lipid regions (Figure 3.10). this occurred across large regions of the bilayer (Figure 3.12).

These peroxidation results are largely at odds with the membrane pacemaker theory of ageing. Mouse cell membranes have been measured as having nine time the amount of docosahexaenoic acid, the fatty acid most susceptible to peroxidation (A. J. Hulbert, Faulks, and Buffenstein 2006). This should make the NMR lipids more resistant compared with the mouse lipids, however the opposite was seen.

It has been suggested that the level of peroxidation itself is not key, but instead the ability to minimise the effects of this (Lewis, Andziak, et al. 2013; D. Munro et al. 2019). This work shows that the phase separation expressed in the NMR does not act in this protective manner. Instead seeming to amplify the damage compared with the compositionally more susceptible mouse lipids. In phase separated lipid bilayers, the disordered phase is rich in unsaturated lipids. Lipid peroxidation is a free radical reaction, where the intermediate, lipid peroxyl radical, is able to initiate the peroxidation of another unsaturated lipid (Ayala, Muñoz, and Argüelles 2014). These unsaturated fatty acid tails are the target of the peroxidation pathway.

The highly phase separated bilayers, with their composition heterogeneity, could be acting to increase the local effective concentration of the unsaturated, peroxidation

susceptible lipids. These lipids are more abundant in the disordered phase, so high amounts of ordered phase is effectively compartmentalising a larger numbers of the lipids together in smaller regions.

For this chain reaction to stop two radicals need to react with one another to terminate the chain. By locally concentrating the unsaturated lipids, this propagating chain reaction is able to occur at an accelerated rate.

These results do not rule out the phase separation as a protective feature in NMRs. These experiments expose the entire bilayer surface to peroxidising solution. If the peroxidation source, a reactive oxygen species in live cells, is localised within the bilayer, the phase separation might act in a protective manner by containing the peroxidation damage to smaller regions of the bilayer by hindering the free diffusion of the peroxidised lipids, radicals and reactive oxygen species.

Cell membranes contain a range of other molecules other than lipids which are able to terminate the free radical propagation such as antioxidants like vitamin E or proteins (H.-Y. Huang et al. 2002). Phase separation has been shown to alter the location of crowding of molecules like these (Stone et al. 2017; Wassall and Stillwell 2009).

Assuming the phase separation is expressed in cells, itself a controversial topic (S. Munro 2003), the phase separation could indirectly be a protective mechanism, with the phases providing a suitable environment for the crowding of molecules able to terminate the peroxidation before extensive damage can occur.

If the phase separation is a feature of thermodynamically equilibrated lipids, and the highly unequilibrated lipids found in cells do not phase separate, then the localised damage seen here would not occur and further work assessing the peroxidation on the out-of-equilibrium cell membrane not expressing this phase separation is required to see if a similar effect is seen in the much more complex system.

Chapter 4. Amyloid destroys naked mole-rat lipid bilayers

4.1 Summary

Naked mole-rats are extraordinarily long-lived rodents that do not exhibit signs of cognitive impairment or accumulate amyloid plaques, a hallmark of Alzheimer's disease, despite having high concentrations of amyloid beta, even from an early age. In this chapter, atomic force microscopy was used to show naked mole-rat brain extracted lipids phase separate, similarly to the cell line organ lipids in chapter 3. Amyloid preferentially interacts with disordered lipids in a DOPC/DPPC supported lipid bilayer but extensively fragments naked mole-rat brain lipid extract supported lipid bilayers. The naked mole-rat brain lipids are more susceptible to amyloid beta induced damage than mouse lipids, for both human and naked mole-rat sequence amyloid beta.

4.2 Introduction

As shown in chapter 3, naked mole-rat (NMR) cell-line lipids exhibit a high degree of phase separation with large amounts of ordered rafts, cholesterol-rich ordered domains within the lipid bilayer. The lipid bilayer composition and phase have been shown to be influential in behaviour of the interactions between amyloid beta (Aβ) and the lipid bilayer (Azouz et al. 2019; Sanguanini et al. 2020). The interactions with the differing states of Aβ in the Aβ aggregation pathway (figure 1.1) and various lipid phases is not fully resolved, with cholesterol, associated with ordered lipid bilayers, accelerating the primary nucleation pathway, yet disordered lipids accelerating the secondary nucleation pathway by interacting with Aβ fibrils, but not monomers (Habchi et al. 2018; Lindberg et al. 2017). The interfacial behaviour of Aβ aggregation in supported lipid bilayer (SLB) is also noted (Azouz et al. 2019), with Aβ visible in porcine brain extract at the damaged step edge of the SLB (J. Lee, Kim, et al. 2017; Mrdenovic et al. 2019).

While the NMR lipids show a high degree of phase separation, the commercially available brain total lipid extract do not show phase separation and will not feature

any phase related Aβ-lipid effects (Canale et al. 2018; J. Lee, Kim, et al. 2017).

If the phase separation shown in chapter 3 is consist with NMR brain lipid extract, then the high degree of phase separation might alter the Aβ-lipid interactions and provide insight into the longevity and resistance of NMRs compared with mice and their resistance to high levels of Aβ without the formation of plaques (Edrey, Medina, et al. 2013).

To develop further understanding of the relationship between Aβ and the NMR brain lipids, atomic force microscopy (AFM) will be utilised to confirm if the high degree of phases separation seen in the previous chapter is present in the NMR brain extracted lipids, something not seen in SLBs of commercially available porcine brain lipid extract. The interactions of both human and NMR Aβ with both a model phase separated SLB and with both NMR and mouse brain lipid extract SLBs. The aggregation of Aβ in the presences and absence of a range of lipid vesicles will be assessed. NMR, mouse and model systems will be used to determine any differences in the aggregation.

4.3 Methodology

4.3.1 Atomic force microscopy

AFM experiments were performed on an Agilent 5500 microscope with a closed loop scanner, using a liquid cell to examine the SLBs in PBS or water. All experiments were carried out at 20 °C. Tapping and contact mode images were obtained using aluminium coated cantilevers (PPP-NCSTR and PPP-CONTR, Apex Probes, UK respectively). All contact mode cantilevers had a nominal spring constant of between 0.02 and 0.77 Nm^{-1} with a tip radius of less than 7 nm.

4.3.2 Supported lipid bilayer preparation

The two model membrane lipids, dioleoylphosphatidylcholine (DOPC) and dipalmitoylphosphatidylcholine (DPPC) (Avanti Polar Lipids), were dissolved in chloroform in a 3 to 1 molar ratio and dried under nitrogen, then re-suspended in ultrapure water to a final concentration of 1 mg/ml and vortexed. The animal brain tissue derived lipids (mouse and NMR) were dried down to form a film and then resuspended in ultrapure water. Uni-lamellar vesicles were formed via ten cycles of freeze-thawing followed by extrusion ten times through a polycarbonate membrane with pores sizes of 100 nm using a mini-extruder (Avanti Polar Lipids) kept 50 °C on a hotplate. 200 μl of solution

containing the extruded vesicles was pipetted onto freshly cleaved muscovite mica and this was then placed on a thin metal disk that itself was placed on a hotplate at 50 °C and the sample was annealed for 15 minutes. The sample was rinsed thoroughly via repeated partial solution exchange, ensuring the samples always remained hydrated. The sample was then loaded into the AFM liquid cell ready for imaging. When imaged in contact mode, a confirmation indentation and successful breakthrough event were recorded to confirm the presence of bilayer before proceeding with imaging. This is not possible in tapping mode so where in doubt, after imaging, a contact mode tip was used to perform an indentation and confirm the existence of the bilayer.

4.3.3 Force spectroscopy

Indentations were made using the contact mode tips. The measured spring constant (using Thermal K) of tips used were all measured in the range 0.05-0.18 Nm^{-1}. Indentations were taken on a uniformly spaced 16 x 16 grid (256 points) on 10 μm x 10 μm areas of bilayer. The tip indentation speed was 1 $\mu\mathrm{m\,s}^{-1}$. Breakthrough events were detected and the breakthrough force was calculated using an automated method (J. K. Li, Sullan, and Zou 2011).

4.3.4 Aβ preparation

Aβ (1-42), human (Anaspec) and NMR (recombinantly expressed) was reconstituted with 1.0% NH_4OH and aliquoted before freezing. Before use the aliquot was defrosted and made up to the desired concentration with PBS buffer. This solution was then vortexed for 2 minutes before being added to the SLB. For all experiments 200 μl of 8 μM Aβ solution was added to the supported bilayer and left for 2 hr. This was removed by gentle pipetting and the bilayer was rinsed gently three times in PBS buffer to remove any free floating Aβ.

4.3.5 Aβ aggregation

20 μM thioflavin T (ThT) was added to 5 μM human Aβ in a low binding eppendoff tube taking care to avoid air bubbles. Each sample was then pipetted, along with lipid vesicle sample, into multiple wells of a 96-well half-area, low-binding, clear bottom and PEG coated plate (Corning 3881), to give 80 μL per well. Kinetics assays were initiated by placing the 96-well plate at 37 °C under quiescent conditions in a plate reader (Fluostar Omega, BMGLabtech, Offenburg, Germany). The ThT fluorescence

was measured through the bottom of the plate with a 44 nm excitation filter and a 480 nm emission filter. The ThT fluorescence was followed for three repeats of each sample and each sample was run without Aβ to create a baseline to be subtracted from the data.

The assay was run for 16 hours and the normalised intensity was fit to

$$F = F_0 + \frac{a}{1 + e^{-k(t-t_{0.5})}} \tag{4.1}$$

where F_0 is the initial intensity, a is the peak intensity, k is the rate constant and $t_{0.5}$ is the time to half maximal intensity. The lag time, t_{lag} was then calculated as

$$t_{lag} = t_{0.5} - \frac{2}{k} \tag{4.2}$$

4.4 Results

4.4.1 Aβ on mica

Before the effect of Aβ on lipid bilayers can be assessed, the base behaviour on bare mica needs to be seen. When imaged in liquid no sign of Aβ was seen, this behaviour has been previously reported as caused by electrostatic repulsion between negatively charged mica and Aβ (Watanabe-Nakayama et al. 2020). Upon drying the Aβ solution, depositing the Aβ onto the mica, fibres were visible along with higher order structures, this is the case for both the human sequence and NMR sequence (Figure 4.1). The two Aβ sequences only vary by a single amino acid with the histidine in the human sequence at position 13 replaced with an arginine in the NMR sequence. This single amino acid change does not effect the ability of the Aβ to form fibres, which both readily do (Figure 4.1A and 4.1C), having heights of a similar characteristic height of around 5 nm. The sequences also form higher order structures. In human sequence (Figure 4.1B), the majority of these structures have a similar height to the fibres, and individual fibres can be seen around them. In NMR sequence (Figure 4.1D) the structures are much less well defined and higher, having heights ranging from 8 nm to 16 nm. Surrounding the structures and fibre are small point like aggregates of Aβ which have the characteristic height of fibres.

4.4.2 Aβ avoids gel phase regions in DOPC/DPPC model lipid bilayer

With this baseline behaviour of Aβ on the bare mica the interaction with a binary phase separated membrane was studied. Prior to exposure to Aβ, the DOPC/DPPC

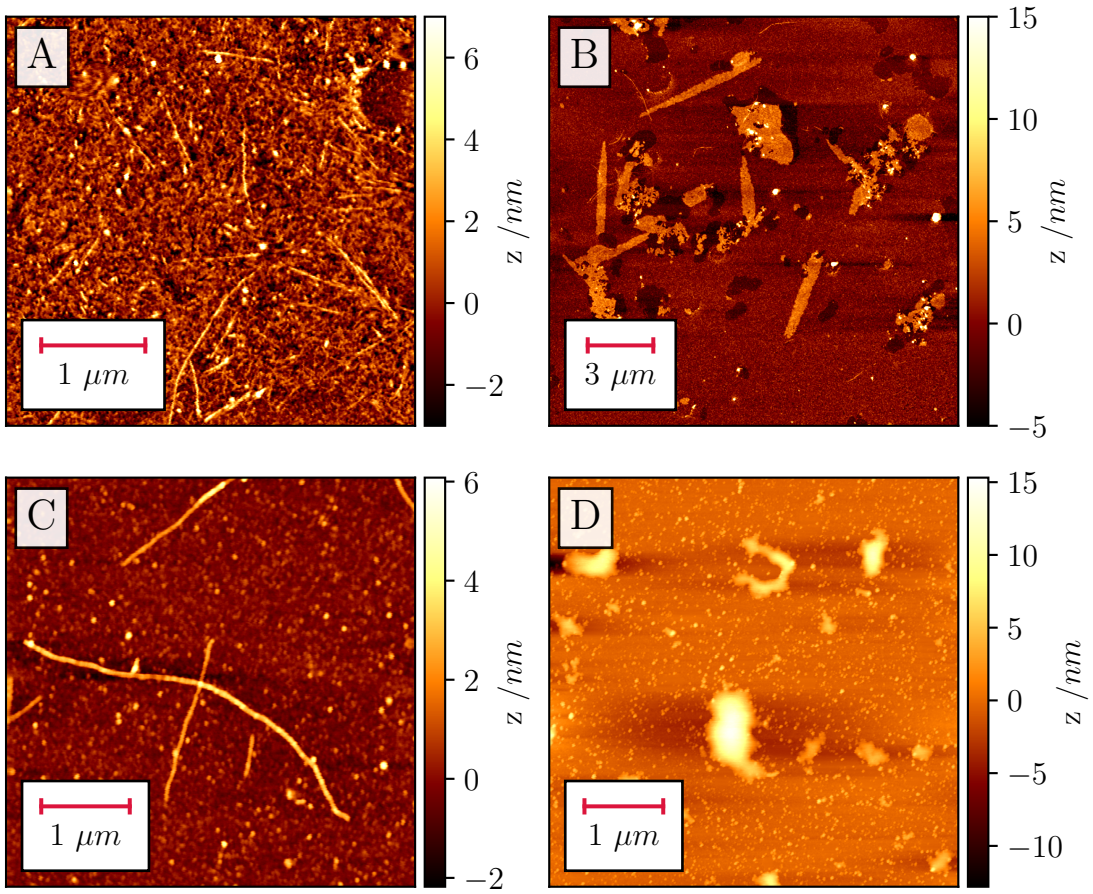

Figure 4.1: Tapping mode image of synthetic human Aβ fibres (A) and higher order structures (B) and recombinantly expressed NMR Aβ fibres (C) and higher order structures (D) on bare mica. Fibres in both cases have a high surface coverage and are approximately 5 nm in height. In human Aβ the higher order structures have a similar height to that of the fibres. Fibres can be seen with the higher order structures in with the human Aβ. NMR Aβ higher order structures are less well defined.

lipid bilayer exhibited the expected phase separation into a DPPC-rich ordered phase and a DOPC-rich disordered phase, shown in Figure 4.2A. Following exposure to Aβ for 2 hours the bilayer remained intact but with visible changes. 'Rough' areas appeared where the Aβ has interacted with the bilayer (Figure 4.2A). The Aβ is seen to be visibly interacting exclusively with the DOPC-rich regions, avoiding the DPPC-rich phase. Closer inspection (Figure 4.2C) shows that a small central DPPC-rich domain can still be seen intact, indicated by the arrow, surrounded by Aβ.

In a more visibly effected area of DOPC/DPPC this can seen (Figure 4.3). A line profile taken along the black dashed line shows the difference in height of the DPPC-rich regions shown in blue, DOPC-rich regions shown in green and the Aβ/DOPC region shown in white. The characteristic phase separation induced height change can be seen between the DPPC and DOPC rich regions, and a difference in surface fluctuations can be seen between the DOPC and Aβ/DOPC regions. Small isolated DPPC regions can also be seen unaffected by the Aβ.

4.4.3 Aβ destroys highly phase separated naked mole-rat lipid bilayers

The previous section showed how in a simple phase separated system, the Aβ/lipid interactions were highly dependant on the phase state of the regions of bilayer. With disordered lipids being much more susceptible to interaction with Aβ. NMR brain SLBs (Figure 4.4A) exhibit a much higher degree of phase separation than DOPC/DPPC. It is hypothesised that this increased amount of ordered lipid acts in a protective manner reducing interactions between Aβ and the SLB.

However, when exposed to Aβ however the bilayer is disrupted, with the raft covered membrane becoming fragmented (Figure 4.4B). The height of the remaining regions of lipid bilayer consistent with that of a bilayer intentionally damaged by dehydration to expose the underlying mica.

NMR sequence Aβ has the same effect as human sequence. In Figure 4.5, before exposure the tiered rafts are visible. With the same characteristic small additional 0.5 nm additional step seen in the cell-line lung lipids. After 2 hours of exposure to NMR Aβ however the same complete bilayer fragmentation can be seen, actually removing more of the underlying lipid than the human Aβ. Looking around the remaining fragments small amounts of lower height bilayer can also be seen. Figure 4.6 shows a close up of another area of fragmented bilayer. Along the profile of the black dashed line the broken bilayer can be seen along with the small indentation in the middle. The

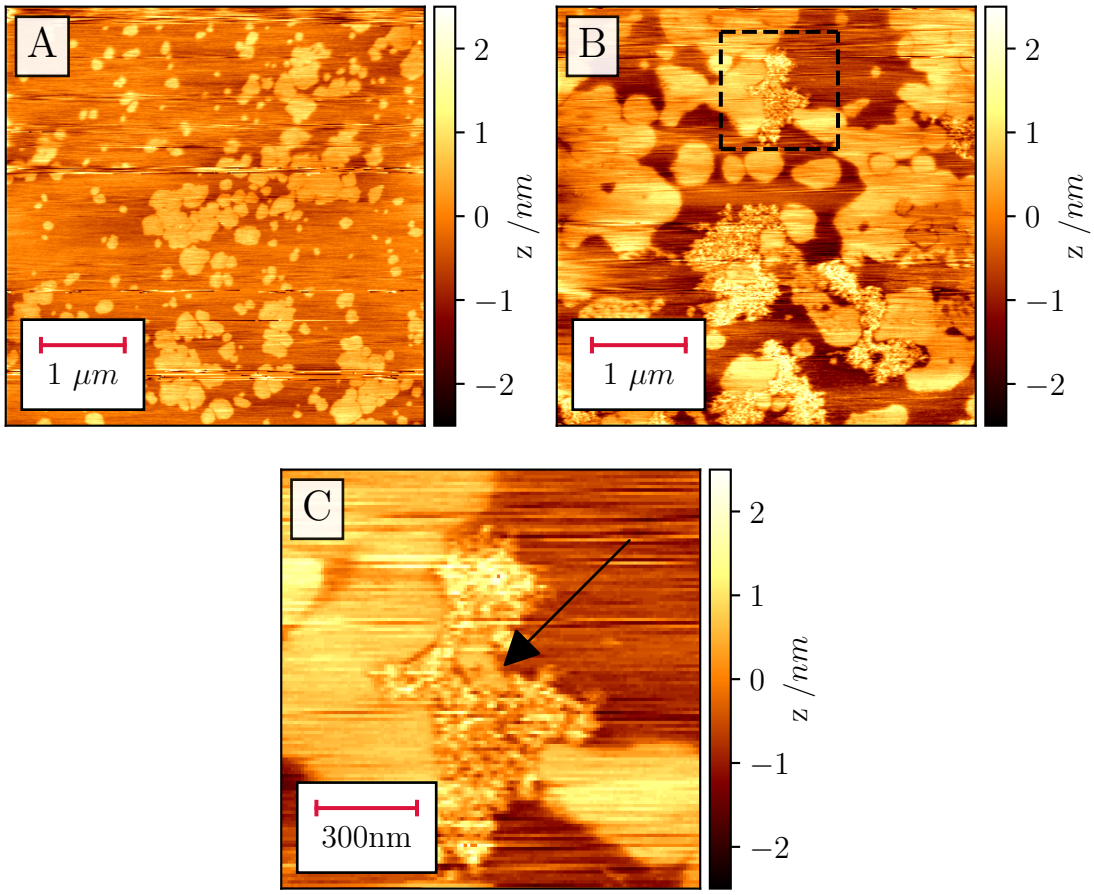

Figure 4.2: Contact mode images of the same 3:1 molar ratio DOPC/DPPC SLBs before (A) and after (B) exposure to human Aβ for 2 hours. A close up of the black box in panel B is shown in panel C. The Aβ alters the surface of the fluid liquid disordered phase while leaving the liquid ordered rafts untouched. The arrow in panel C indicates a small untouched central domain surrounded by Aβ.

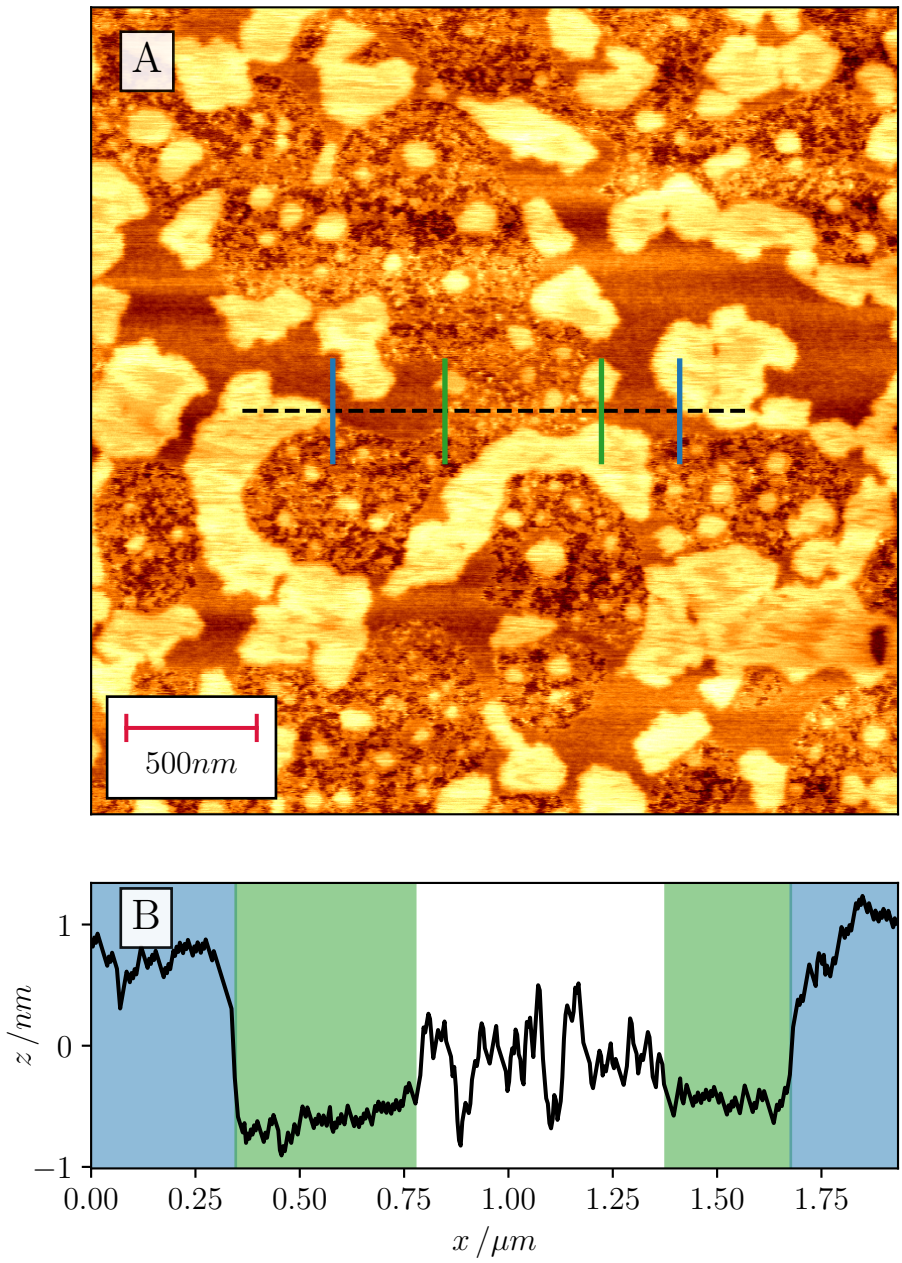

Figure 4.3: Contact mode image of a 3:1 molar ratio DOPC/DPPC SLBs after exposure to human Aβ for 2 hours (A). The line profile (B) shows the height along the black dashed line. The markers in A and colouring in B mark the interfaces of the different regions along the line profile. Blue on the outside is the gel phase. Green in the middle is the disordered phase. White in the center is the Aβ effected area.

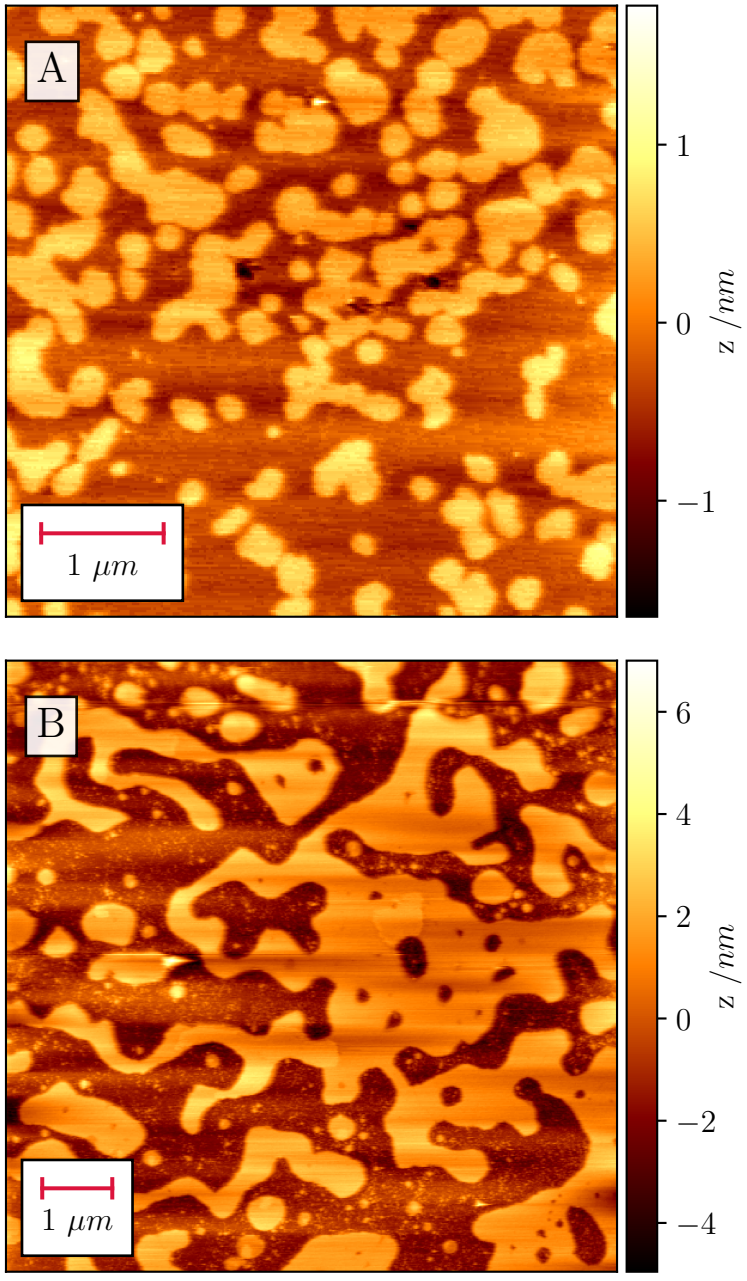

Figure 4.4: Tapping mode images of the same NMR brain SLBs before (A) and after (B) exposure to human Aβ for 2 hours. The characteristic high degree of phase separation can be seen before exposure. After the bilayer has been severely damaged with large sections of underlying mica visible.

height difference in the remaining lipids is 1 nm indicating these are small regions of disordered lipids remaining.

Human sequence and NMR sequence Aβ have similar disruptive properties to the NMR brain extracted lipids. In both cases the bilayers are heavily fragmented with vast areas of mica becoming visible between the remaining lipid fragments. Most signs of phase separation in the remaining fragments are gone but small amounts of lower height lipids are occasionally detected indicating the remaining fragments of bilayer are the ordered phase.

In direct contrast with this is the mouse brain lipid bilayer. Initially there is only sparse phase separation visible, similarly to reported result using porcine brain extract (Mari et al. 2018). Exposure to human Aβ does not have the same destructive effect as in NMR (Figure 4.7). The bilayer remains largely intact following 2 hours of exposure with the introduction of some defects. Closer inspection of the defects however reveal a pit like structure with a depth too shallow to be a complete hole. The integrity of the bilayer was maintained across large regions despite extensive pitting.

As with the NMR lipids, the mouse lipids behave similarly when exposed to NMR Aβ. The low amounts of phase separation are seen before exposure and pitting tis seen in the surviving bilayer. The key difference between human and NMR Aβ exposure is the extent of pitting. A lesser fraction of the surface is pitted.

The raft like features visible in both Figure 4.7B and Figure 4.8B are the same height as the sparse rafts seen prior to exposure in both cases, although they appear to be larger laterally and have increased surface coverage. When attempting the image these features closely they were not visible.

4.4.4 Aggregation of Aβ in the presence of lipids

The effect of Aβ on lipid bilayers has been seen to have differing effects - with raft avoiding behaviour in simple systems, fragmenting behaviour in NMR lipids and a pitting behaviour in mouse lipids. This brings to question if the lipids are accelerating the aggregation of Aβ, enabling the damage to be induced more or less rapidly. The lag time for aggregation of Aβ fibres is shown in Figure 4.9. Despite the differences in damage seen in SLBs, vesicles of mouse or NMR lipids do not have differing aggregation propensities relative to one another and both animals aggregate much slower than in the binary system, or single component DOPC or DPPC lipids. In all cases the addition of lipids hindered the lag time compared with the Aβ alone.

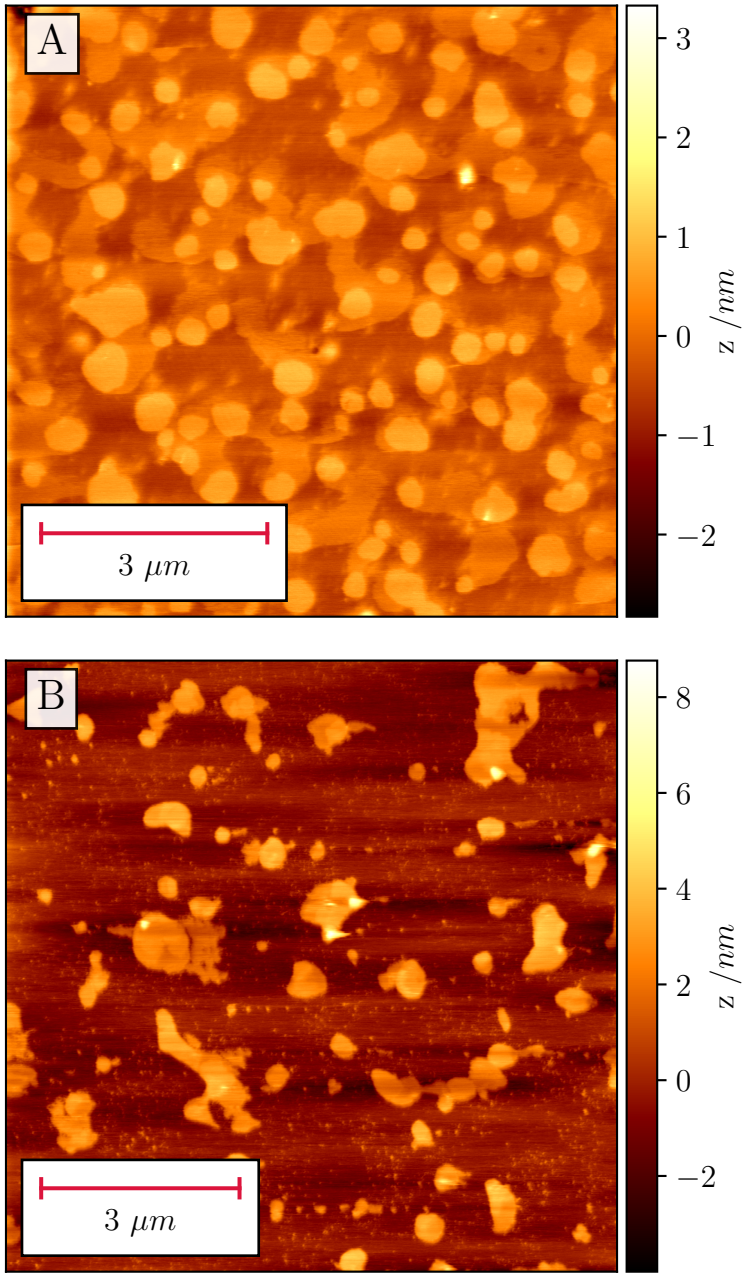

Figure 4.5: Tapping mode images of the same NMR brain SLBs before (A) and after (B) exposure to NMR Aβ for 2 hours. The characteristic high degree of phase separation can be seen before exposure, with a 2 tiered raft structure visible. After the bilayer has been severely damaged with large sections of underlying mica visible. Some of the two tiered structure is still visible around some of the remaining bilayer fragments.

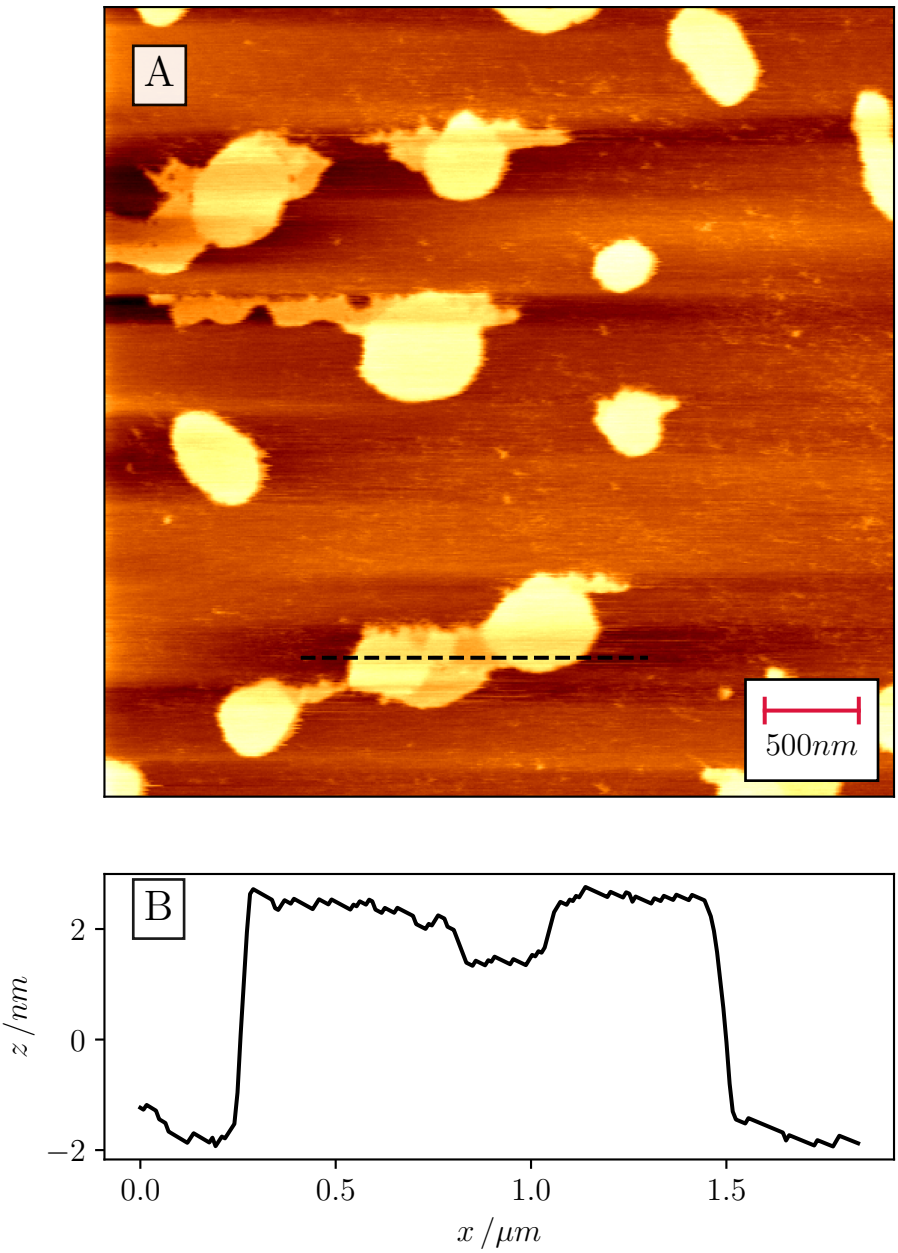

Figure 4.6: Tapping mode images of the a NMR brain SLBs after exposure to NMR Aβ for 2 hours (A). The line profile (B) shows the height along the black dashed line. The bilayer fragment can be seen to be seen to protrude $\sim 5nm$ from the mica surface, within the fragment a second tier can be seen $\sim 1nm$ below the higher regions.

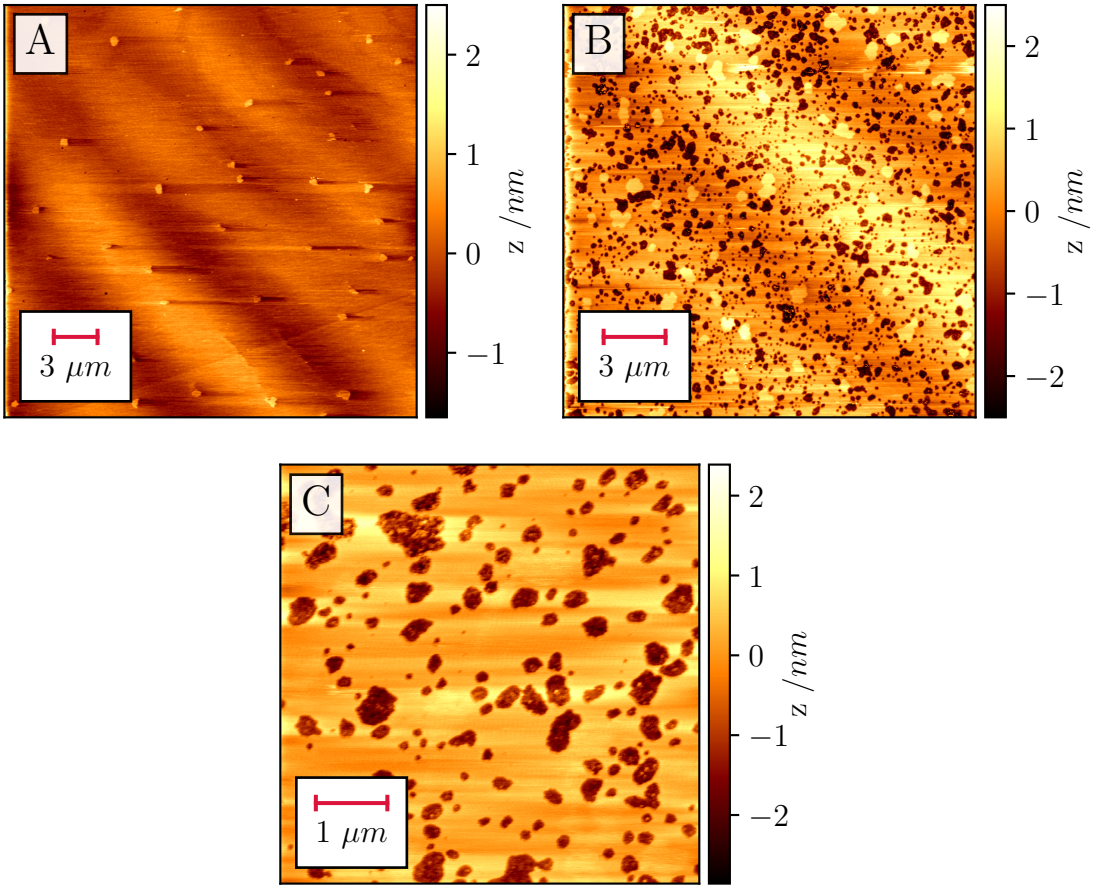

Figure 4.7: Tapping mode images of the same mouse brain SLBs before (A) and after exposure to human Aβ for 2 hours at large scale (B) and a smaller scale (C). The low level of phase separation can be seen before and after exposure the bilayer remains largely intact across large regions. Upon closer imaging pit like features can be seen. At $2\,nm - 2.5\,nm$ these pits are too shallow to be holes to the underlying mica.

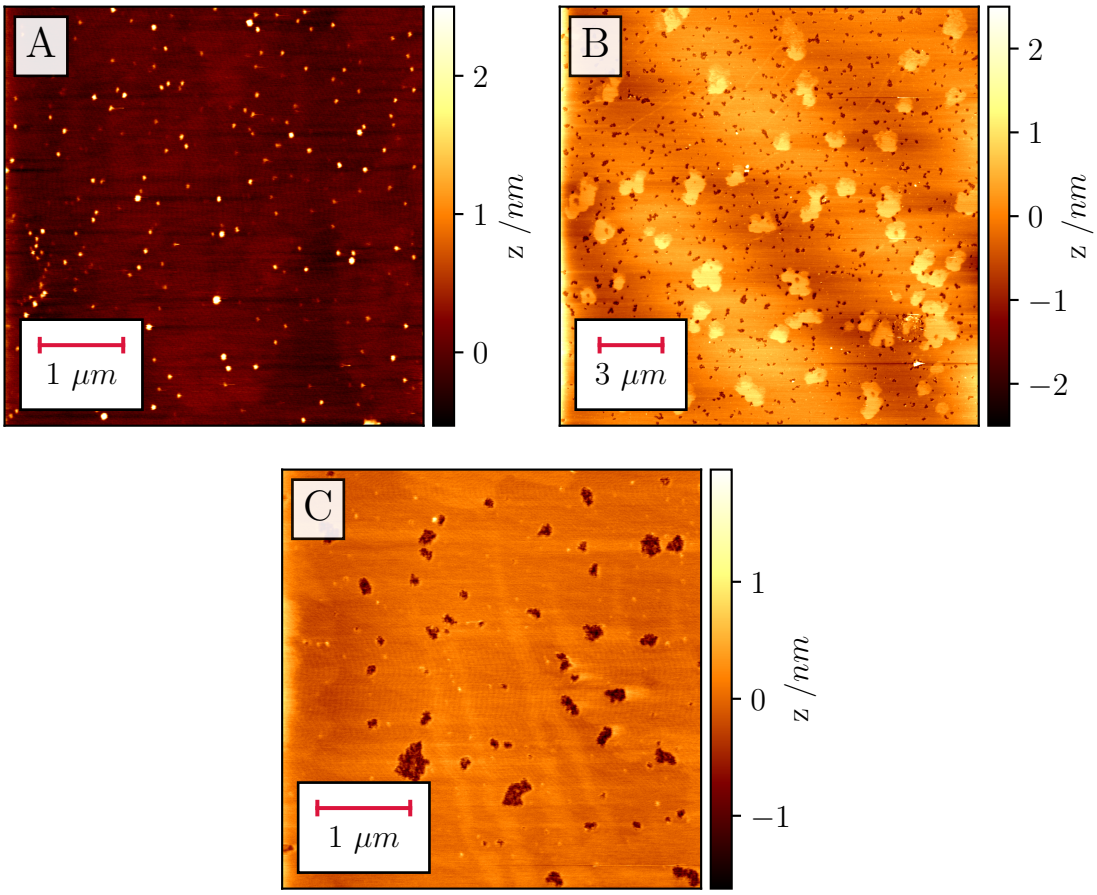

Figure 4.8: Tapping mode images of the same mouse brain SLBs before (A) and after exposure to NMR Aβ for 2 hours at large scale (B) and a smaller scale (C). The low level of phase separation can be seen before and after exposure the bilayer remains largely intact across large regions. Upon closer imaging pit like features can be seen. At $1\,nm - 2.5\,nm$ these pits are too shallow to be holes to the underlying mica.

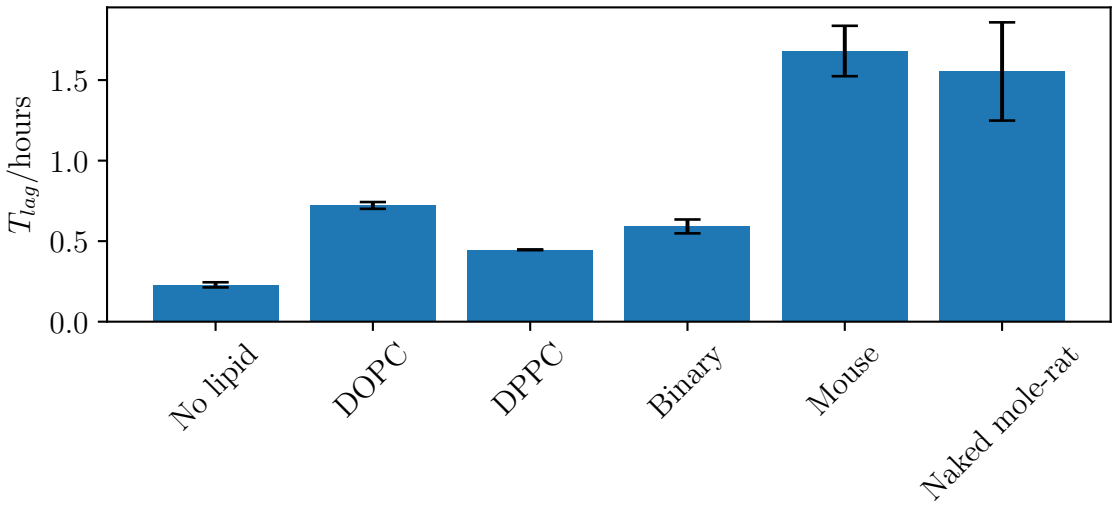

Figure 4.9: Result of the ThT aggregation assay for human Aβ and a range of lipids. Each sample was run 3 times and at least 3 samples were used (from different animals where applicable). There is no significant difference in the aggregation lagtime between mouse and NMR although both severely hinder the aggregation relative to no lipids, single component or binary lipid vesicles.

The high degree of phase separation in the NMR brain lipids does not act according to the simple binary system. Force spectroscopy, shown in Figure 4.10, confirms the difference in properties of the mouse and NMR bilayers, in agreement with the high degree of ordered phase separation, the NMR bilayer requires much more force for a breakthrough event to occur. There are no noticeable difference in breakthrough depth, which is a metric for the bilayer thickness, although underestimates relative to the image based analysis.

Despite the fact that NMR brain lipids are phase separated with high degrees of ordered lipids, which are able to resist Aβ interaction in model systems, somewhat counter intuitively the NMR lipids are highly susceptible to damage by Aβ. The composition of the lipids were assessed to detect key differences in the bilayers (Frankel et al. 2020). Of particular interest are two components in the brain lipid extracts. Sphingomyelin (SM) and cholesterol, both linked with the interaction of Aβ and lipid membranes. The relative concentrations of cholesterol and sphingomyelin, shown in Figure 4.11, show the key differences in composition of the lipids. This could explain the high degree of phase separation in NMR lipids as cholesterol is a key component

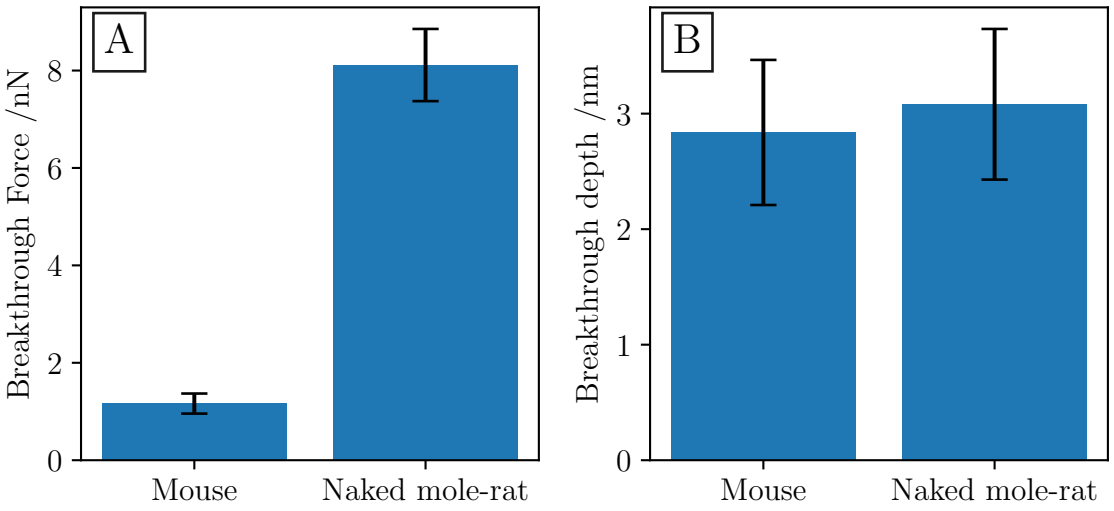

Figure 4.10: Force spectroscopy results taken on grids on the NMR and mouse brain lipid bilayers. The breakthrough force (A) is largely different, with a high force for NMR indicating a less fluid bilayer. The breakthrough depth (B) of the two samples is consistent. 2859 and 1220 breakthrough events were recorded for NMR and mouse bilayers respectively.

associated with lipids rafts, increasing the order and stiffness of lipid bilayers.

4.4.5 Naked mole-rat cell line organ lipid are not destroyed

In contrast with the brain extracted lipids, exposure of human Aβ to NMR organ cell-line lipids such as lung (Figure 4.12) behaved in a similar manner to the model DOPC/DPPC bilayer (Figure 4.3). Beforehand a high degree of phase separation, characteristic of all NMR SLBs is visible. Upon exposure to Aβ a high level of surface coverage of the Aβ can be seen but there is a distinctly visible boundary between the ordered phase separated regions and the Aβ. This SLB shows no signs of fragmentation or direct damage, even less so than the mouse brain SLB even. The extensive interaction of the disordered phase and Aβ are highly consistant with that of DOPC/DPPC (Figure 4.3), with both systems also showing small regions of smoother surfaced disordered lipids remaining but a majority of the disordered lipids showing a much rougher surface than both the disordered and ordered lipid regions.

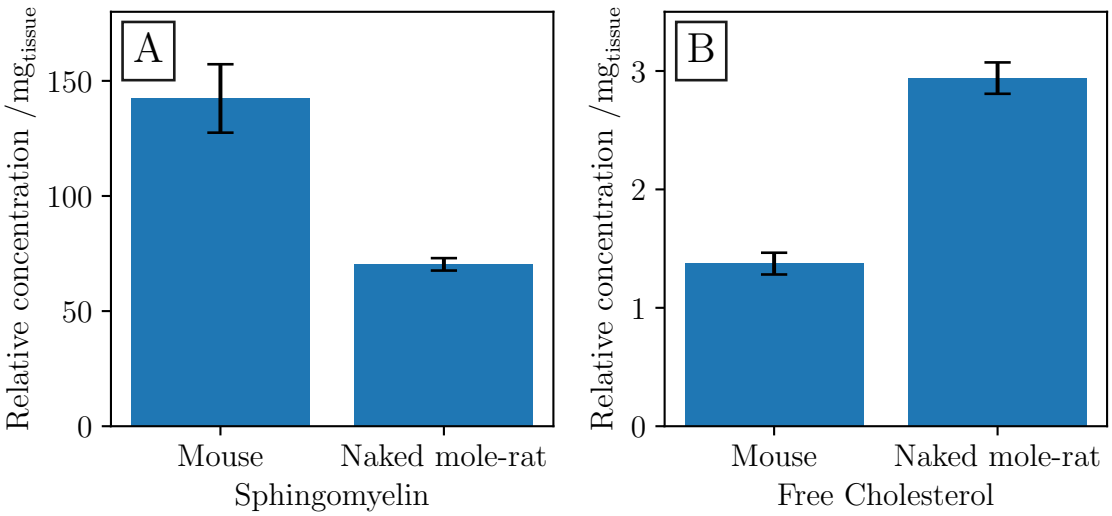

Figure 4.11: Relative concentration of sphingomyelin (A) and cholesterol (B) in brain lipid extract per mg of brain tissue the sample was extracted from, taken from 7 NMRs and 6 mice. NMR brain lipid extract has significantly less sphingomyelin and more cholesterol than mouse brain lipid extract.

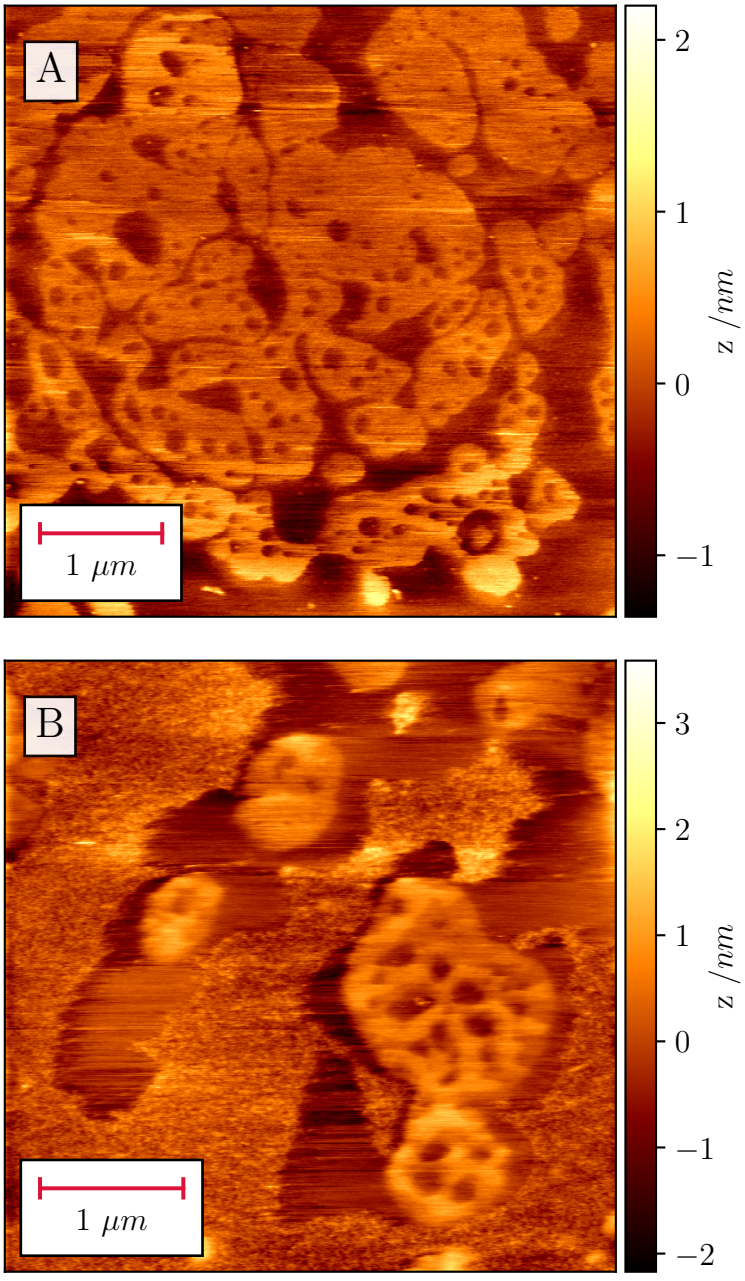

Figure 4.12: Contact mode images of the same NMR lung cell line lipid bilayers before (A) and after exposure to human Aβ for 2 hours (B). The complex and high degree of phase separation can be seen both before and after and Aβ is seen to be away from the ordered phase.

4.5 Discussion and conclusions

NMR Aβ differs from human Aβ by a single amino acid. An arginine replaces a histidine at position 13 (Edrey, Medina, et al. 2013). This amino acid change does not appear to be the mechanism of protection in NMRs, in agreement with studies in the same Aβ sequence but still susceptible Degu (Inestrosa et al. 2005). Their behaviour on bare mica is very similar, with both sequences readily forming fibres of a similar characteristic height of 5 nm and both sequences also form higher order structures (Figure 4.1). The two forms of Aβ also behave similarly when exposed to NMR brain lipids (Figures 4.4 and 4.5) and to mouse brain lipids (Figures 4.7 and 4.8).

As with the NMR organ cell-line lipids in the previous chapter, the NMR brain extracted lipids also form highly phase separated SLBs (Figures 4.4 and 4.5)

When human Aβ was exposed to the phase separated DOPC/DPPC model membrane, the Aβ has specific interactions with the bilayer (Figure 4.2). The Aβ avoids the ordered lipids, instead interacting exclusively with the disordered DOPC lipids. Where the Aβ interacts the surface of the disordered lipids is changed, with them being much rougher (Figure 4.3) but there are no signs of the underlying mica which would indicate extensive damage to the bilayer. The interaction of Aβ is highly phase linked, and the NMR lipids are highly phase separated, with large regions of ordered lipids. Indentations into the surface of the lipids show the NMR lipids are significantly more ordered, with a higher breakthrough force.

However, unlike the DPPC/DOPC which showed Aβ resistance, with the Aβ avoiding interaction with the more ordered phase, NMR suffered extreme damage and the bilayer was extensively fragmented when exposed to both human Aβ (Figure 4.4) and NMR Aβ (Figure 4.5). There are small fragments of bilayer that remain, and these would appear to mostly be ordered lipids when assessing the height profile of these fragments (Figure 4.6). The NMR ordered lipids did not provide the protective mechanism expected based on the model phase separated system. This could be because the complex composition of the lipids, while DPPC has been shown to hinder aggregation of Aβ, the addition of cholesterol removed this ability (Hellstrand, Sparr, and Linse 2010).

This extensive damage was not mirrored in mouse brain lipids, which showed morphological differences and developed 'pits' but did not break (Figures 4.7 and 4.8). The pits are too shallow to be holes through to the underlying mica, like seen on a in the NMR (Figures 4.4 and 4.5). In the larger scale images there appeared to be the development of rafts after exposure to both Aβ sequences, however attempting closer

inspection these disappeared so could not be confirmed as a real feature (Figures 4.7B and 4.8B). When attempting contact mode imaging of mouse brain (and other organs), tip-bilayer interactions had proved troublesome. The existence of this in multiple separate SLB preparations exposed to the two differing Aβ sequences could imply this is just a feature, however highly sensitive to the experimental conditions.

The mouse lipid/Aβ pits are different again from the DOPC/DPPC Aβ interactions. The mouse lipid pits are inset into the surrounding lipids, lying below the height of the bilayer surface. The rough surface that appears with in the DOPC/DPPC lipids (Figure 4.3) is not inset into the surrounding lipid, only appearing that way when the Aβ regions are at the order/disorder boundaries.

While the NMR seems unaffected by high levels of Aβ in their brains, passive protection from the composition and unique phase behaviour of their brain lipids does not offer the explanation for this ability to resist Aβ. As with the peroxidation in the previous chapter, the phase separation and compartmentalisation of the lipids into two distinct regions with different compositions could be contributing to this. This is not necessarily true for all NMR lipids. Lung lipids when exposed to Aβ showed similar behaviour to the DOPC/DPPC lipids (Figure 4.3), with the Aβ roughening the surface of the disordered lipids and avoiding interactions with the more ordered lipids (Figure 4.12).

Assessing the aggregation rate of Aβ plaques in solution with the ThT assay showed that all lipids hindered the aggregation compared with no lipids (Figure 4.9). This is in contrast with some reported T_{lag} values which indicate lipids accelerate the process (J. Lee, Kim, et al. 2017) although the effect of lipid vesicles has been shown to both hinder and accelerate the aggregation based on the lipid species and mixture complexity (Sanguanini et al. 2020). While the animal extracted lipids had the largest hindering effect, there was no significant difference between the two. The ThT assay measures the larger aggregates, and the lower the plaque formation potentially the increase exposure time to Aβ monomers and oligomers which have been suggested to be the damaging components, not the plaques (Walsh and Selkoe 2007) Increasing the concentration of cholesterol in vesicles accelerates the Aβ aggregation (Habchi et al. 2018), however the mouse and NMR aggregation rate is similar despite NMRs having a much higher concentration of cholesterol (Figure 4.11). If the intermediate aggregation products are causing damage, and the aggregation is the same, this raises the question how the NMR brain lipids are thoroughly fragmented where mouse lipids are not? Does the

cholesterol and sphingomyelin differences lead to differences in the aggregation pathway or the specific intermediates in the process?

Chapter 5. Effect of Sphingomyelin fatty acid chain length

5.1 Summary

Sphingomyelin was identified as a key difference in the lipid composition of naked mole-rat and mouse brains in chapter 4. Increased levels of this lipid are linked with Alzheimer's disease patients and with inducing phase separation of lipid bilayers. A key differences between the sphingomyelin of naked mole-rat and mouse brains was the tail length distribution. In this chapter, molecular dynamics simulations were undertaken of a range single component sphingomyelin lipid bilayers at a range of differing tail lengths. All simulations were at physiological naked mole-rat burrow temperatures. All bilayers formed in the ripple phase rather than the fluid phase and with increasing tail length, the conformational complexity of the lipid increased along with the amplitude of the bilayer undulation. Attempts to classify the bilayer into a two state coexistence using standard metrics proved unsuccessful.

5.2 Introduction

The different compositions of lipids in naked mole-rat (NMR) and mice may contribute to the different behaviour in phase and amyloid interaction demonstrated in chapter 3 and 4. In the previous chapter, the relative amounts of sphingomyelin (SM) and cholesterol were identified as key compositional differences between the NMR and mouse brain lipids. Both of these components have been attributed to raft formation and amyloid aggregation (Amaro et al. 2016; Azouz et al. 2019; M. C. Owen et al. 2018).

In this chapter atomistic molecular dynamics (MD) simulations of lipid bilayers will be undertaken to get a molecular level insight into the behaviour of the lipids and the bilayer itself. Before complex physiological composition lipid bilayers can be understood the individual components need to assessed as a baseline to compare any lipid behaviour differences. Based on lipidomic analysis of the lipid components of the NMR brain, simulations of single component SM lipid bilayers with a range of tail

length asymmetries will be analysed to assess the key changes in bilayer properties with the different chain lengths. Lipid asymmetry has strong links with the phase behaviour of bilayers. Increasing asymmetry in SM is able to stabilise gel and ordered domains at higher temperatures in lipid vesicles (Engberg et al. 2020), although at very long chain lengths it has also been reported that lipids form a homogenous mixture, rather than a phase separated system at shorted chain lengths (Ramos, Bouwstra, and Lafleur 2020). Asymmetric, saturated, lipid tails have been suggested to act in a similar manner to unsaturated lipids in a bilayer yet are not susceptible to peroxidation (P. Smith, D. M. Owen, et al. 2021).

While this type of MD simulation have been completed before they did not cover the highly asymmetric lipids, focusing on the 16 and 18 carbon tail SM molecules (Venable et al. 2014). These simulations, as is common practice for lipid bilayer simulations, were performed at high temperatures. A through understanding of the basic behaviour of baseline single component systems at temperatures more closely related to the experimental work of the previous chapters and physiological conditions for the NMR burrow (Holtze et al. 2018).

5.3 Methodology

5.3.1 Simulation details

Atomistic MD simulations of single component SM lipid bilayers were performed. Systems consisted of 128 SM lipids and ∼5120 TIP3P water molecules (Jorgensen et al. 1983). The CHARMM36 forcefield was used (J. Huang et al. 2017). GROMACS 2019.6 was used to perform all simulations (Abraham et al. 2015). Initial membrane structures were generated using the CHARMM-GUI membrane builder (J. Lee, Cheng, et al. 2016). Three systems with acyl chain lengths of 16, 18, 20, 22 and 24 carbons were generated using CHARMM-GUI. A further three 14 carbon acyl chain length system was generated based on the SM16 systems, for a total of 18 independent systems. Systems were first energy minimised and equilibrated in the NPT ensemble at a pressure of 1 bar and a temperature of 303.15 K. Production simulations were run using the V-rescale thermostat and the Parrinello-Rahman barostat, with the pressure controlled semiisotropically (Bussi, Donadio, and Parrinello 2007; Parrinello and Rahman 1981). A 2 fs timestep was used and periodic boundary conditions were applied in all directions. A switching function over 1-1.2 nm was used for Lennard-Jones interactions. The particle-mesh Ewald method with a real-space cutoff of 1.2 nm was used for electrostatics (Essmann

et al. 1995). As with the equilibration simulations, productions simulations were run at 303.15 K. Each bilayer was simulated for at least 10 μs.

5.3.2 Analysis details

Visualisation was performed using VMD and data analysis was performed using custom python codes with the MDAnalysis library (Gowers et al. 2016).

Deuterium order parameter, S_{CD}, measures the ensemble average orientation of the C-H bond vector (θ) with the bilayer normal (z-axis) as

$$S_{\mathrm{CD}} = \frac{1}{2}\langle 3\cos^2\theta - 1\rangle \tag{5.1}$$

Bilayer thickness, the distance between the phosphate atoms in each leaflet, was calculated on a per lipid basis by coupling each lipid with the nearest lipid in the opposite leaflet and taking the phosphate distance in the z-axis

$$T_i = Z_{phosphate,i} - Z_{phosphate,j} \tag{5.2}$$

Since a lipid bilayer consists of two leaflets, for a bilayer of N lipids in total, the leaflet thickness is defined as

$$T_{leaflet} = \frac{1}{2N}\sum_{i=1}^{N} T_i \tag{5.3}$$

Similarly to the bilayer thickness, the individual lipid chain lengths were measured. This was defined as the largest distance in the z-axis between any two of the carbon atoms in the same chain. This is not necessarily the start and end carbon.

Area per lipid was calculated accounting for the bilayer undulations, applying a Voronoi diagram area approach with lipids in small patches of 1.5 nm in radius around the lipids mapped onto flat planar sections. The area of each Voronoi cell was calculated using the shoelace formula.

Lipid splay angle was defined as the angle formed between the triangle comprising of the terminal lipid tail atoms with an apex at the carbon near the tail split.

Distributions of data were calculated using kernel density estimation and the mean value of the property for each lipid across the trajectory timescale. A Gaussian kernel was used with the bandwidth estimated using Scott's rule (Scott 1992).

Lipid distribution separation was undertaken using Gaussian mixture modelling (GMM) and density-based spatial clustering of applications with noise (DBSCAN).

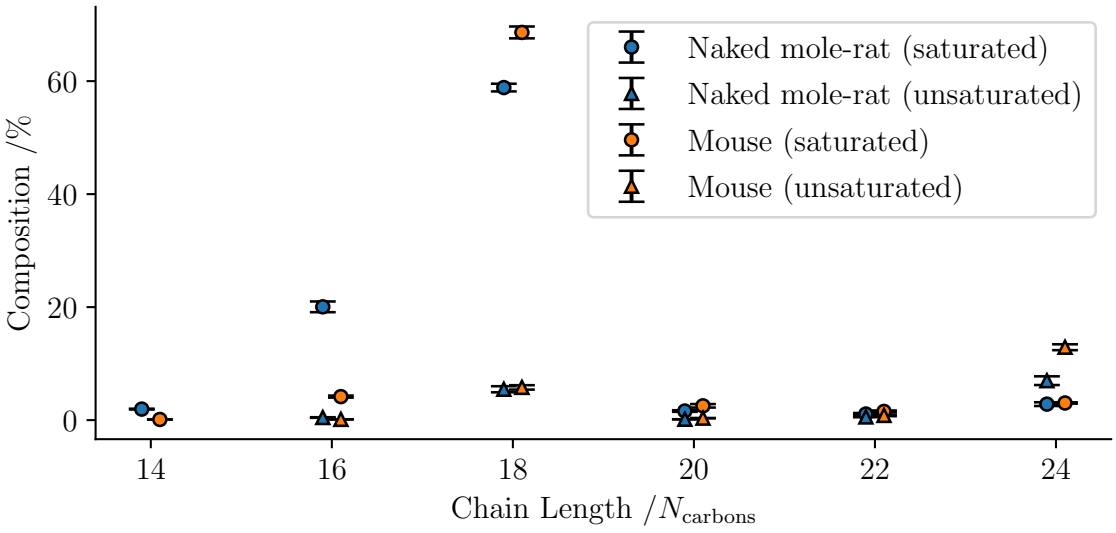

Figure 5.1: Percentage distribution of saturated (circle) and unsaturated (triangle) fatty acid chain lengths in the NMR and mouse brain lipid extracts. Values were calculated from extract from the brains of 7 naked mole rats and 6 mice. Key differences between the animals at chain lengths of 16 and 18 in saturated lipids and 24 for the unsaturated lipids.

5.4 Results

5.4.1 Sphingomyelin chain distribution

SM is not just a single lipid molecule. It is a family of structurally similar lipid molecules. A SM molecule consists of three key features:

1. A phosphocholine headgroup
2. A sphingosine backbone
3. An fatty acid/acyl tail

The phosphocholine headgroup is the same as that in PC lipids such as DOPC and DPPC. The sphingosine backbone, is an unsaturated alcohol consists of 18 carbon atoms that forms one of the lipid tails, the sphingo tail. The other lipid tail is formed by the fatty acid (acyl) tail. The nature of the acyl tail alters the SM and can introduce large lipid tail asymmetry, compared with the sphingosine backbone.

Comparing the fatty acid tail distributions for NMR and mouse (Figure 5.1) shows the differences are not just in the total amount of SM molecules (Figure 4.11), but in

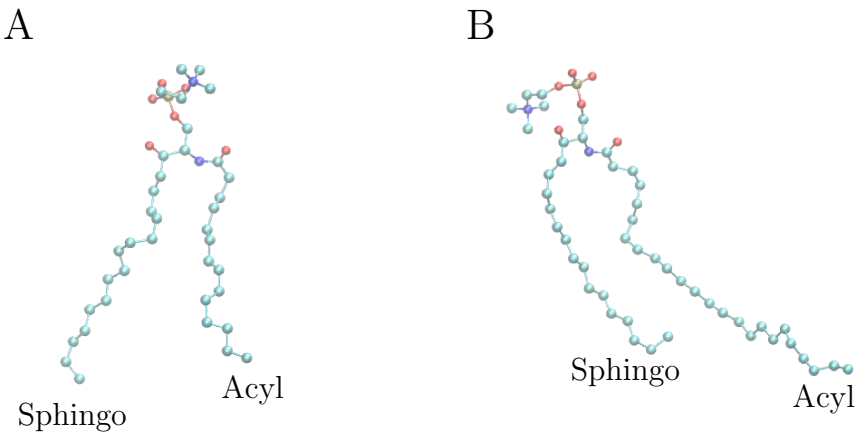

Figure 5.2: Example of a SM14 (A) and SM24 (B), shown here without any of the hydrogen atoms for clarity. Beads are coloured according to atom type. Carbon (cyan), nitrogen (blue), oxygen (red) and phosphate (gold).

the distributions too (Frankel et al. 2020). Excluding 14 (where unsaturated was not measured), in all chain lengths, except 24 there are more saturated than unsaturated lipids for both animals. At chain length 24, in both animals there are more unsaturated than saturated. The differences appear in the distribution of the lipids, particularly in chains of length 16, 18 and 24. In each of these cases there is a significant split between the mouse and NMR compositions. NMR has increase levels of saturated, shorter 16:0 chains whereas mouse has more of the longer chains 18:0 and 24:1.

An example of one of the shortest and longest acyl-chain SM lipids used in this chapter have been shown in Figure 5.2. The fixed 18 carbon length sphingo-tail is on the left in each case and does not change in any of the lipid species. The varying acyl-tail on the right, connects to the second carbon in the sphingo chain via a nitrogen atom.

5.4.2 Ripple phase in sphingomyelin

At the temperature simulated, all the SM bilayers are in the ripple phase rather than the often studied fluid phase. One of the characteristic traits of the ripple phase is the undulation which leads to a minor, thinner region in the bilayer. The ripple phase is considered to be a coexistence of ordered and disordered lipids which allows for this

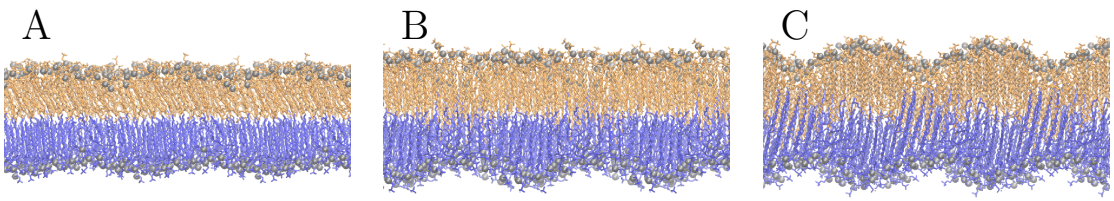

Figure 5.3: Snapshots of single component lipid bilayers with a fatty acid chain length of 16 (A), 18 (B) and 24 (C) carbons. Phosphates are coloured in grey, the individual leaflets of each bilayer have been coloured in orange and blue respectively. Three different schemes can be seen: minor amplitude undulations at 16, large amplitude undulations in one leaflet at 18 and large undulations in both leaflets at 24.

thickness difference to exist. The ordered lipids adopt a conformation with elongated tails rigid and 'frozen' forming the thick region of the bilayer. The disordered lipids are are much more fluid in nature allowing for the smaller thickness.

At 303.15 K, all SM bilayers formed into the ripple phase, rather than the much more commonly studied, higher temperature fluid phase. This is in agreement with experimental data which detects the main transition temperature for SM16 as 314K(Arsov et al. 2018).

This can be seen by visualising the bilayers and is more pronounced in the larger acyl-tail systems (Figure 5.3). In contrast to the other phases of a lipid bilayer, the ripple phase is unique in that it ceases to form a planar, quasi-2d structure and instead develops undulations, most noticeably in the 24 carbon system (panel C). The ripple phase is suggested as a trade off mechanism allowing the large phosphocholine headgroup of the lipids to maintain sufficient hydration whilst also allowing the tighter packing of the tails below the main transition temperature. The optimal solution to this is the melting of some of the lipids tails, allowing an undulation to occur and water to hydrate the headgroups while maintaining a large number of correctly packed tails (Walter, Ruscher, Gola, et al. 2021).

The thickness and area per lipid distributions of the shortest acyl-tail length, 14 carbons, has been shown in Figure 5.4. While the thickness value shows a multimodal distribution, the area per lipid is much more normally distributed centred around approximately 50Å^2. This is in agreement with the theory that the ripple is a hydration maintaining feature, each lipid has a similar exposed surface area to the surrounding

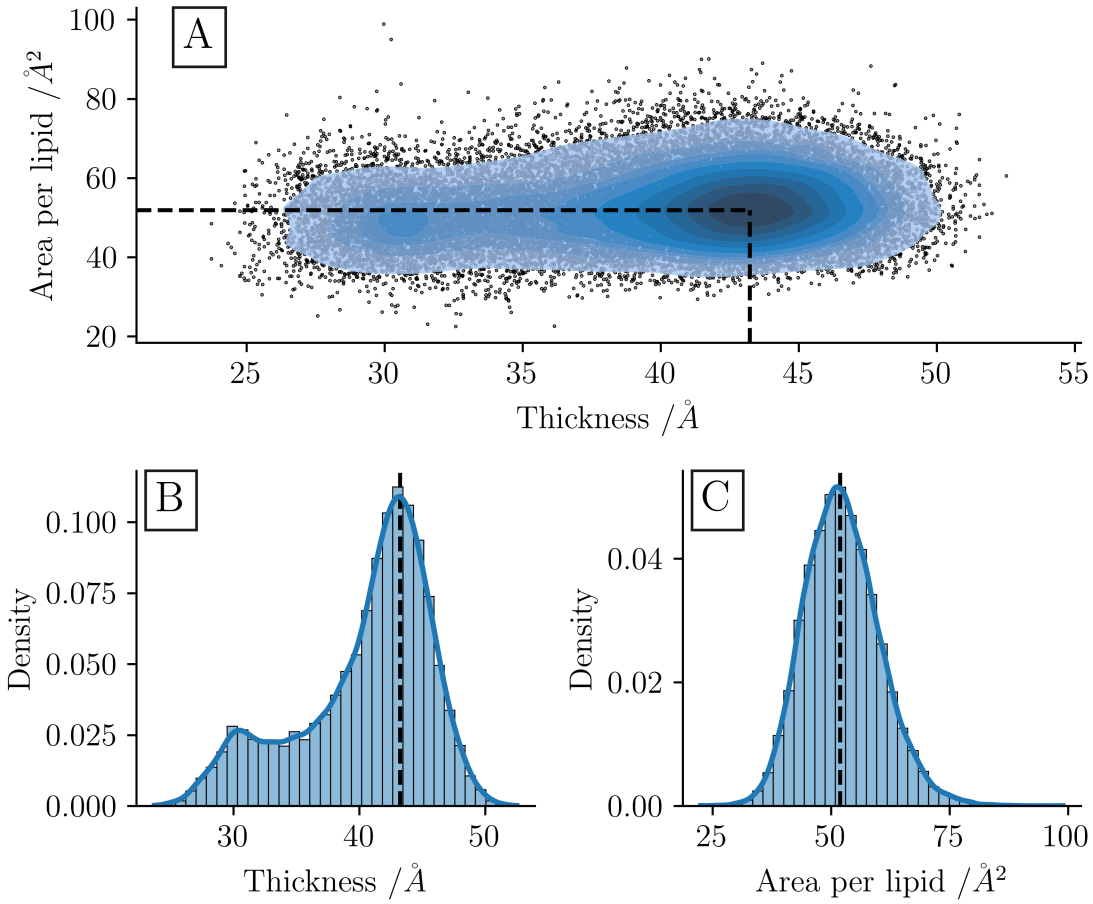

Figure 5.4: Lipid coupled thickness and area per lipid for the SM14 systems. Scatter plot of bilayer thickness and area per lipid (A) and individual histograms of the thickness (B) and area per lipid (C) showing the bimodal thickness and unimodal area per lipid. The black dashed lines indicate the most probable value in each case.

water molecules, and this is enabled by a small subset of lipids forming a thinner region introducing the undulations seen in Figure 5.3.

In all chain lengths this trend is similar, with increasing mean thickness and in all cases consisting of a non-normal distribution containing a subset of lipids in a much thinner distribution. This is with the exception of the largest tail length. SM24 still shows a non-normal distribution and still increases in mean thickness, but the thinner set of lipids is the larger, major peak (Appendix A.1), leading to a decrease in the median thickness.

For the less asymmetric tail length distributions, 16 (two less), 18 (equal) and 20 (two more) carbons, the distributions do not have as clear a second peak, instead

the secondary peak is absorbed into the main peak and appears more like a skewed distribution (Appendix A.2).

5.4.3 The sphingomyelin ripple as a two phase coexistence

The ripple phase is often considered a two component coexistence between ordered and disordered lipids. Here attempts are made to quantify and classify the lipids that belong to these two regions. The undulations of the ripple lead to a thicker and thinner region, referred to as the major and minor arm respectively. The two regions have been separated by applying GMM with two components to estimate the two underlying thickness distributions of these two regions in a bilayer comprised of SM16 (Figure 5.5A). The probability of the lipid with a given thickness belonging to one of these distributions and not the other is then calculated, each lipid at a given time step was assigned to the cluster it was most probable to belong in.

While the thickness distribution of a bilayer can be split into two Gaussian distributions, applying this split to other properties of the bilayer is not as convincing. While the thickness of a simulation can be split into two distributions the splitting is not effectively mirrored when mapped onto other lipid properties: the area per lipid, acyl tail length, tail splay angle and deuterium order parameter (Figure 5.5).

The area per lipid distribution, which is normally distributed, splits into two mostly overlapping distributions, with the thinner lipids having a smaller average area per lipid (Figure 5.5B), something already seen in Figure 5.4. These thinner lipids exist in the area of concave region of the undulation, and the larger in the convex region. The shape of a lipid and its intrinsic curvature are often linked like this, convex curvature requiring a larger headgroup and concave curvature requiring a smaller headgroup (Epand et al. 2015).

Of these properties the tail length (panel C) and splay angles (panel D) do not separate into obviously distinct distributions, with the maxima showing little shift. The tail length distribution features a major peak around 23Å, as might be expected, approximately half of the median bilayer thickness. It also features a minor peak/tail of smaller lipids, similarly again to the thickness, although the probability of this is much lower than in the thickness distribution. The separation into two underlying distributions might then be expected to separate these regions, as it has in the thickness. The thinnest lipids are indeed more likely to be shorter, but the major peak of the distribution has not been split in any meaningful way and just split in proportion

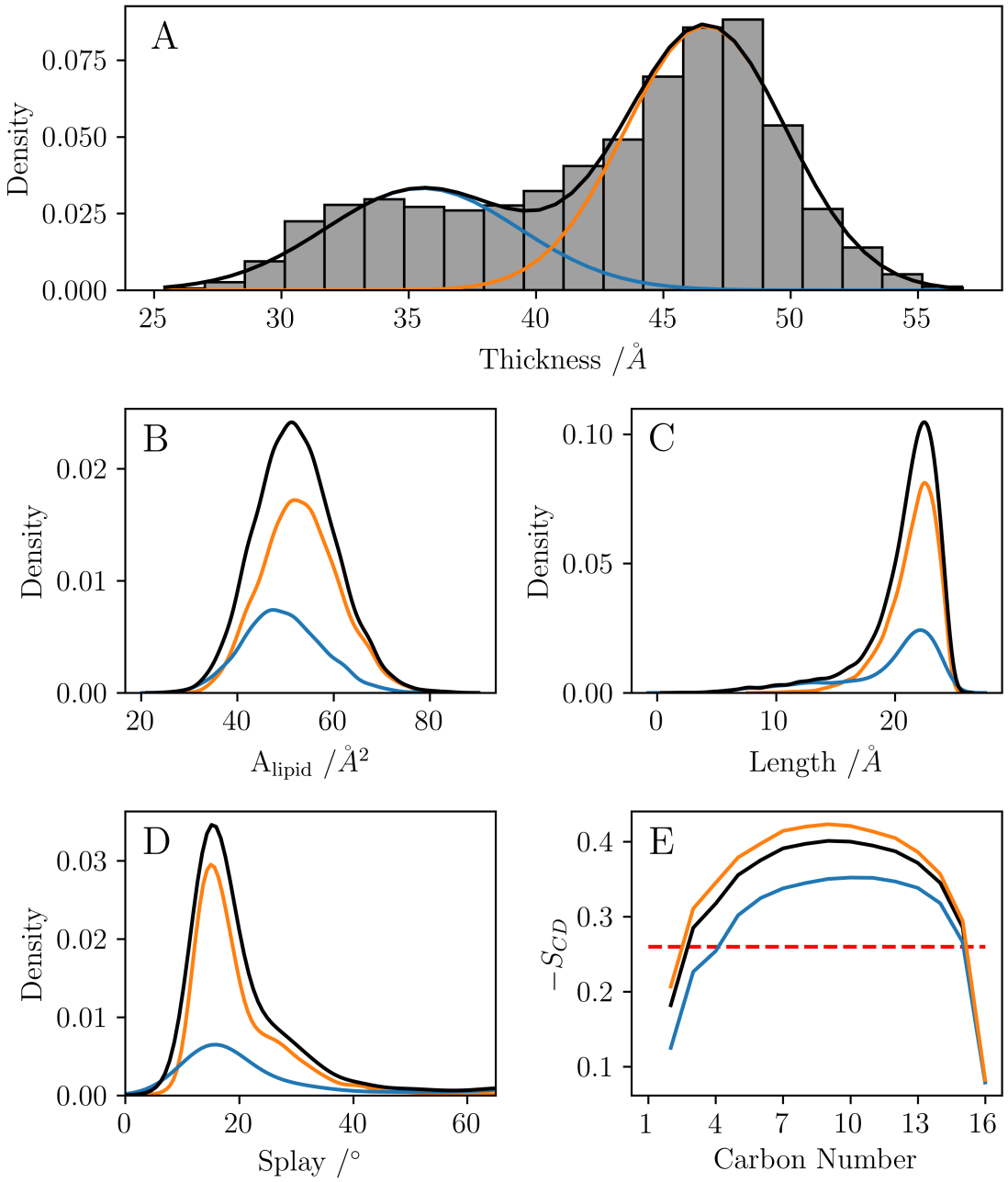

Figure 5.5: Splitting the bilayer properties of a SM16 bilayer based on thickness (A). The area per lipid (B), acyl tail length (C) and splay (D) do not show a substantial splitting of distributions. The deuterium order parameter (E) does but still remains much more ordered than the maximum fluid phase value (red dashed line).

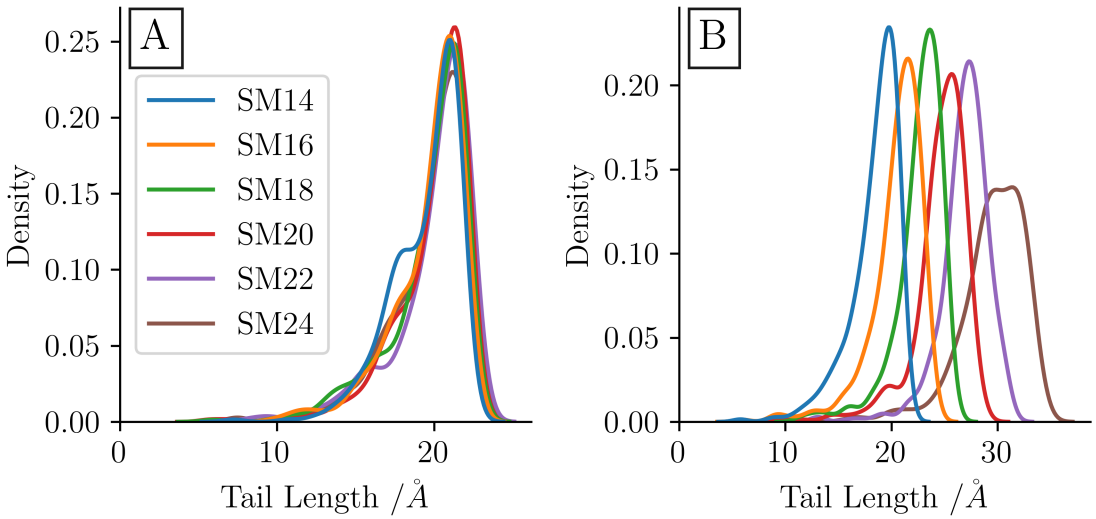

Figure 5.6: Distribution of tail lengths for the sphingo-tails (A) and acyl-tails (B). The sphingo tail distributions remain constant, and the acyl distributions increase with additional carbon atoms.

between the two underlying distributions.

A similar effect can be seen with the lipid splay, which features a shoulder centred at approximately 25°, this is not effectively split using the two state model.

The deuterium order parameter, a common metric to distinguish between ordered and disordered lipids, shows the two regions do split indicating the lipids in the thinner region are more disordered than then thicker counterparts. However comparing this with the expected values from higher temperature disordered simulations these are still much more ordered than would be expected. The red dashed line shows the maximum order for a fluid phase SM16 bilayer (Doktorova et al. 2020).

Across the leaflets of the bilayer the interactions between lipids are complex. The increase in bilayer thickness is matched by the acyl tail. With an increasing number of carbons in the tail the length of the tail increases whereas for all systems and the sphingo-tail remains constant (Figure 5.6).

The distributions for the sphingo (panel A) and acyl tail (panel B) lengths are not normally distributed and show complexity, with a most probable extended conformation, but a minor peak representing a shorter length. In the sphingo tails this is most prominent in the shortest tail (SM14) and in the acyl tail this is most noticeable in the larger tail (SM24), the major peak is substantially broadened.

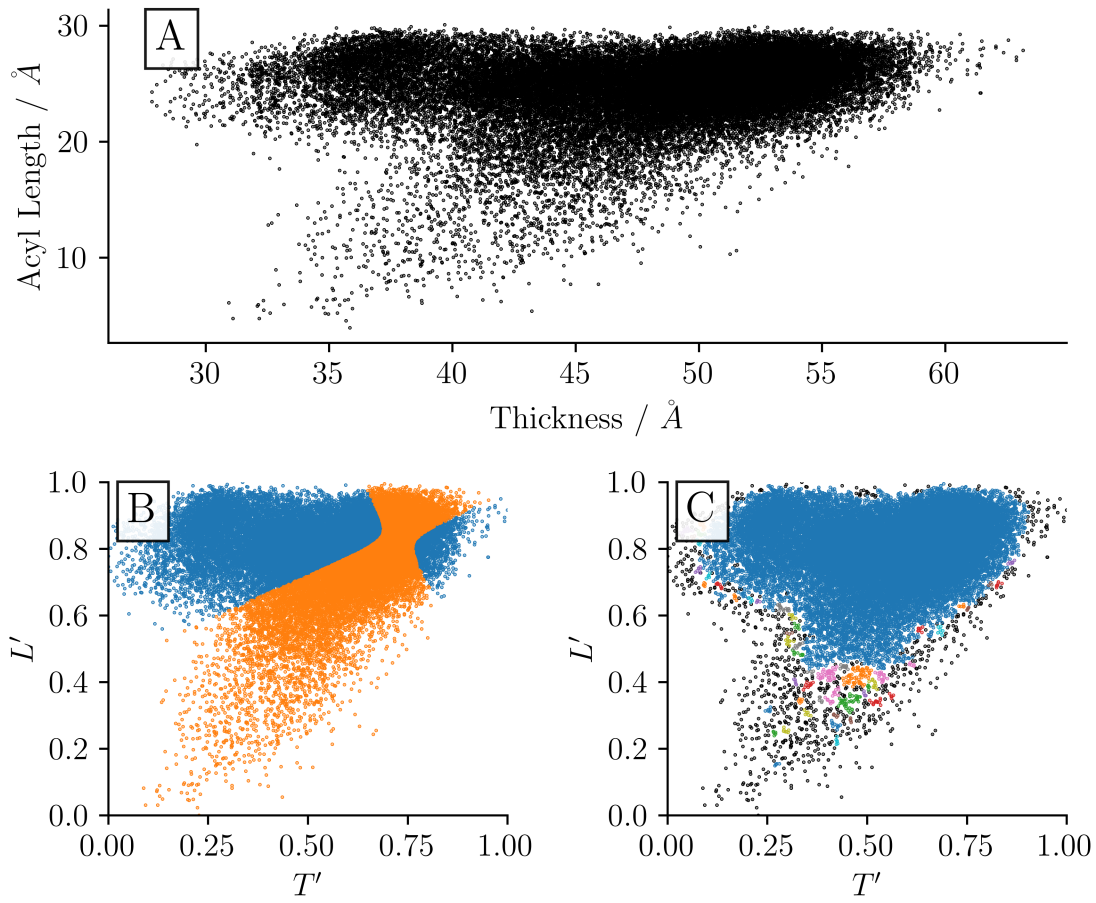

Figure 5.7: Complex interaction of acyl chain length and coupled bilayer thickness for SM20 (A). Examples of unsuccessful attempts at separating the underlying distributions using GMM (B) and DBSCAN (C).

Looking at the interplay between the thickness and acyl length on a per lipid basis reveals much more complicated distribution (Figure 5.7A), featuring a bifurcation at lower thickness values. As would be expected, the thickest lipids in the bilayer have the most extended acyl tails. These lipids correspond with the major arm of the ripple. However in the minor arm, the acyl length is split, with both long and short acyl chains existing. In fact the bilayer was able to become thinnest when the acyl tail was elongated. This complexity could explain why the simple thickness based GMM separation was not able to separate the lipids in a convincing manner, the underlying distribution is not just a function of bilayer thickness but some more complex conformational property.

Higher dimensional attempts, including multiple metrics, also proved as unsuccessful as with the simpler, single feature method above. Shown in Figure 5.7B and C are

a GMM and DBSCAN attempt at separating the two distributions of the major and minor arm, shown here normalised.

The mean increase in leaflet thickness is lesser than the mean increase in acyl tail length, with the acyl-tails interdigitation into the opposing leaflet slightly, overlapping with the tails in the opposite leaflet, increasingly visibly in the larger chain length simulations (Figure 5.3C). This offers an explanation as the ability for a lipid to have an elongated acyl tail, but a shorter thickness. With the two forks in the distribution representing the lipids which had interdigitated and those which had not.

Attempts introducing additional structural metrics, both intrinsic and extrinsic properties of an individual lipid also proved unsuccessful. These additional structural metrics, applied in a variety of combinations, included the area per lipid, sphingo chain length, PN vector angle, tail splay angle, lipid tilt angles and a series of distances and angles between selected atoms. Atoms were selected to attempt to create metrics which would capture and distinguish the lipid conformations identified via visualisation of the lipids within the bilayer.

The metrics are not proving adequate to effectively capture the partition between the major and minor arm of the ripple into a two state system.

5.4.4 Sphingomyelin conformational complexity

With larger chain asymmetry the complexity of the structural quantification of the SM conformation becomes more apparent. At longer acyl tail lengths many of the metrics used begin to show flaws. The splay angle, for example, becomes degenerate once the tail becomes too long due to the increase conformational freedom (Figure 5.8). In an extended state (panel A), the lipid will have a small splay angle, the angle between the terminal carbons with an apex at the carbon where the lipids tails split. However, due to the definition of splay angle, overlapping and inward snorkelling lipids (panel D and E) will also have a small angle, potentially even smaller than that of the extended conformation. Splayed, bent (panel B and C) and outward snorkelling lipids (not shown) will all express as large splay. In reality, only splayed lipids actually show splay, although the inward snorkelling lipid could be considered a splayed lipid with the 'excess' tail bending inward and upward, and resulting in a smaller splay angle. The use of splay angle become less meaningful as a structural metric to distinguish lipids due to this degeneracy.

The lipid average splay angle and thickness have been plotted in Figure 5.9, where

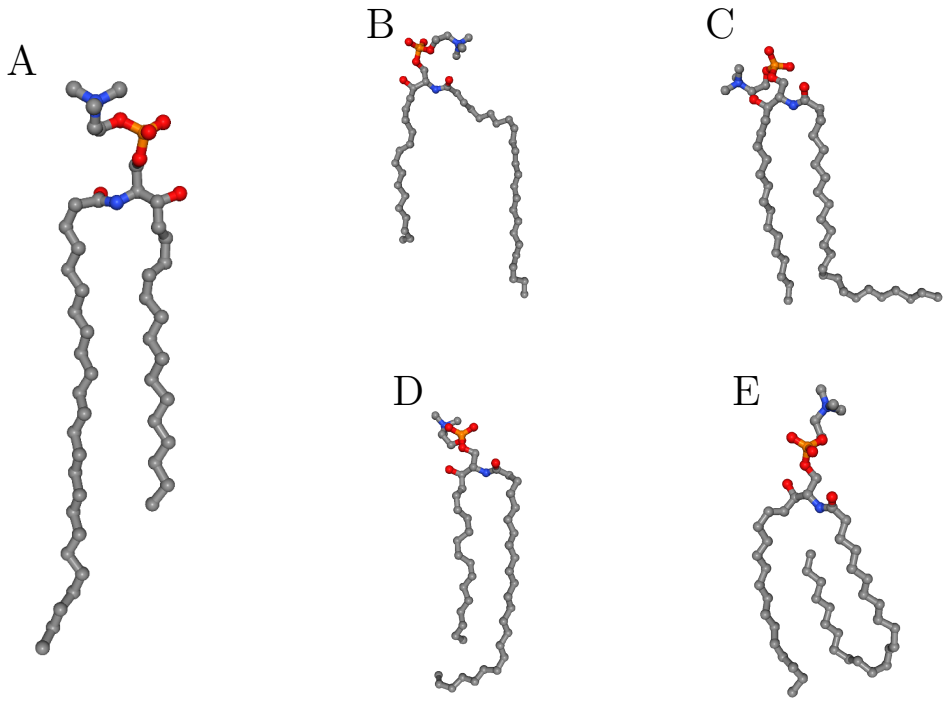

Figure 5.8: Examples of the range of conformational arrangements for SM24 tail packing. Extended (A), splayed (B), bent parallel to the midplane (C), overlapping itself (D) and snorkelling (E).

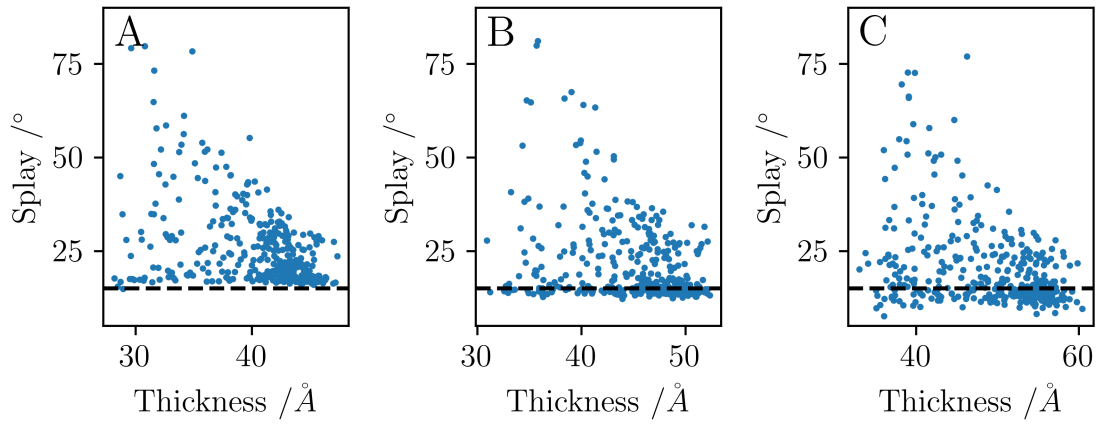

Figure 5.9: Scatter plot if the splay vs thickness for each lipid. SM14 (A), SM18 (B) and SM22 (C). The black dashed line is plotted at 15° in each plot as a guideline.

each point represents a single lipid from all the simulations for a given chain length. In the case of all chain lengths there is a similar structure to the distribution of data, with a low splay angle at high thicknesses and as the thickness decreases the variance on the splay increases. For the large thickness, low splay this is logical given that splaying requires bends in the tails, which would detract from the length. As thickness decreases the lipids become more able to splay, although not all lipids do so. There are some lipids with splayed tails, and others without, although both are able to maintain a small thickness via other mechanisms such as interdigitation, tilting of the lipid and conformational features such as snorkelling, splaying and bending (Figure 5.8). These conformations allow for a smaller thickness because the lipid tail bends backwards and is inserted back into the same leaflet as the lipid, creating a thinner, but laterally larger lipid shape. As the tail length increase the packing of the lipids is able to get more complex, as the conformational features become more available. The lipid tails need to remain in internalised within the bilayer. With the large differences in length the long tail occupies a large degree of complex conformations compared to that of a more even tail length lipid. Each has an impact on the bilayer via differing excluded volume properties. Extended and overlapping lipids have a taller excluded volume, whereas splayed, bent and snorkelling lipids have a wider excluded volume. Splayed lipids leave a void between their tails which must be filled, in fact a inward snorkelling lipid, as shown in panel E, is a splayed lipid which bends to fill the void it leaves. Snorkelling lipids are not always inward and can take the form of an outward snorkel, where the tail bends back upwards but the lipid does not take a splayed form. The wider variety of lipid shapes, modulated the excess tail, allows for a range of more complex conformations, able to introduce a larger amplitude ripple, maintaining the area per lipid, despite the larger size of the lipid.

All this conformational complexity removes the value of some forms of analysis that work effectively for shorter tailed lipids, which do not have as high conformational freedom. Consider the splay and thickness metrics, shown in Figure 5.9. For the shorter tail lipids (panel A) there is a hard limit on the minimum splay given the terminal carbons cannot occupy the same space, indicated by the black dashed line. As the acyl tail gets longer (panel B and C) the lipids are able to access more of the complex conformational states (Figure 5.8) and overlapping and snorkelling states become more available, allowing the splay angle to become smaller across the whole range of thicknesses.

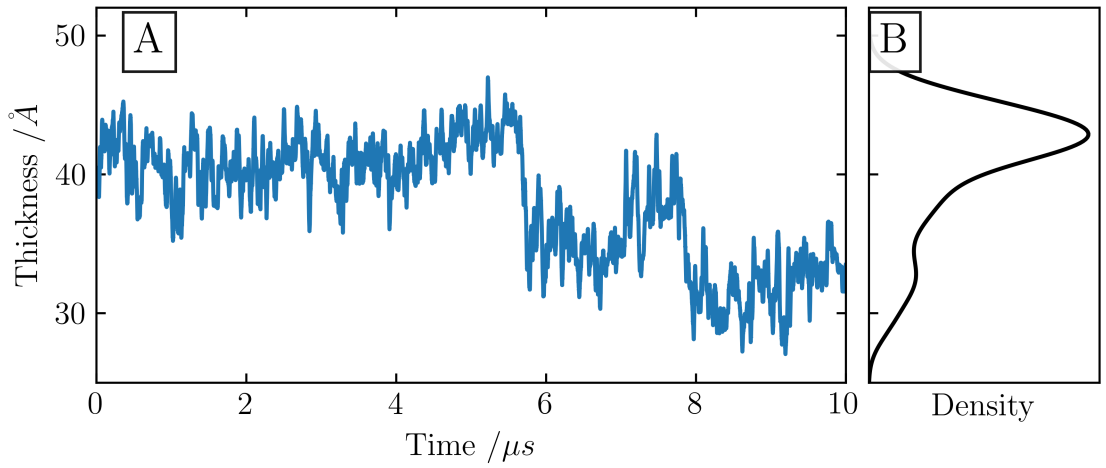

Figure 5.10: Thickness of a single lipid across the entire simulation time from one of the SM14 simulations (A). The lipid can be seen to occupy multiple states in the second half The probability distribution from the average lipid coupled thickness for all lipids (B).

These conformations, whilst distinct from one another, can appear similar when these measures are used. A splayed (panel B), and bent (panel C) lipid will both have high splay scores and low thickness, due to the terminal carbon often ending in a similar position. Equally an inward and outward snorkelling lipid will have a different splay, regardless of the fact they are both tightly packed and within the same leaflet, attempts to identify snorkelling lipids required a metric based on terminal carbon distance from the bilayer midplane to effectively identify.

The case for coupled thickness is even worse since this property replies on the state of both the lipid and its coupling partner, both of which can be in any one of many conformations itself.

A single SM14 lipid thickness can switch between multiple states (Figure 5.10). This is without the added complexity of the larger, asymmetric lipids which are able to occupy multiple conformational states depending on the position on the longer tail. In effect as a property which replies on extrinsic information from the coupled lipid (in the opposing leaflet) the total number of states increase. In the commonly studied fluid phase, this is less of a problem, since the bilayer is planar, without undulations and lipid heterogeneity/coexistence like seen in the ripple phase. This raises the question, is

coupling the lipids across the z-axis correct, or is a more rigorous definition of coupling required for non-planar bilayers? Lipid structure and the ripple phase is not just defined by the lipid tails however. While some of the lipids modulate their thickness though the tail conformational changes, others do so with the headgroup. Figure 5.11 shows a single lipid which can be seen to occur in 3 different thickness states (panel A) over the final 500 ns of the trajectory. The lipid conformation has been extracted at three points in corresponding to each of the major thickness states seen in panel A. In all three states the acyl tail adopts a bent, extended conformation with no splaying occuring in the tails. In the thinnest state (panel B), the headgroup is bent forming a reverse 'c' shape with two bends, both in the headgroup and at the headgroup/tail connection. The intermediate thickness state (panel C) is similar but the headgroup and headgroup/tail connection are in a more straightened state. Finally, the thickest conformation of the three (panel D) has the top of the headgroup bent, allowing the phosphate (orange) to occupy the higher space within the bilayer, being higher than the nitrogen (blue) of the headgroup.

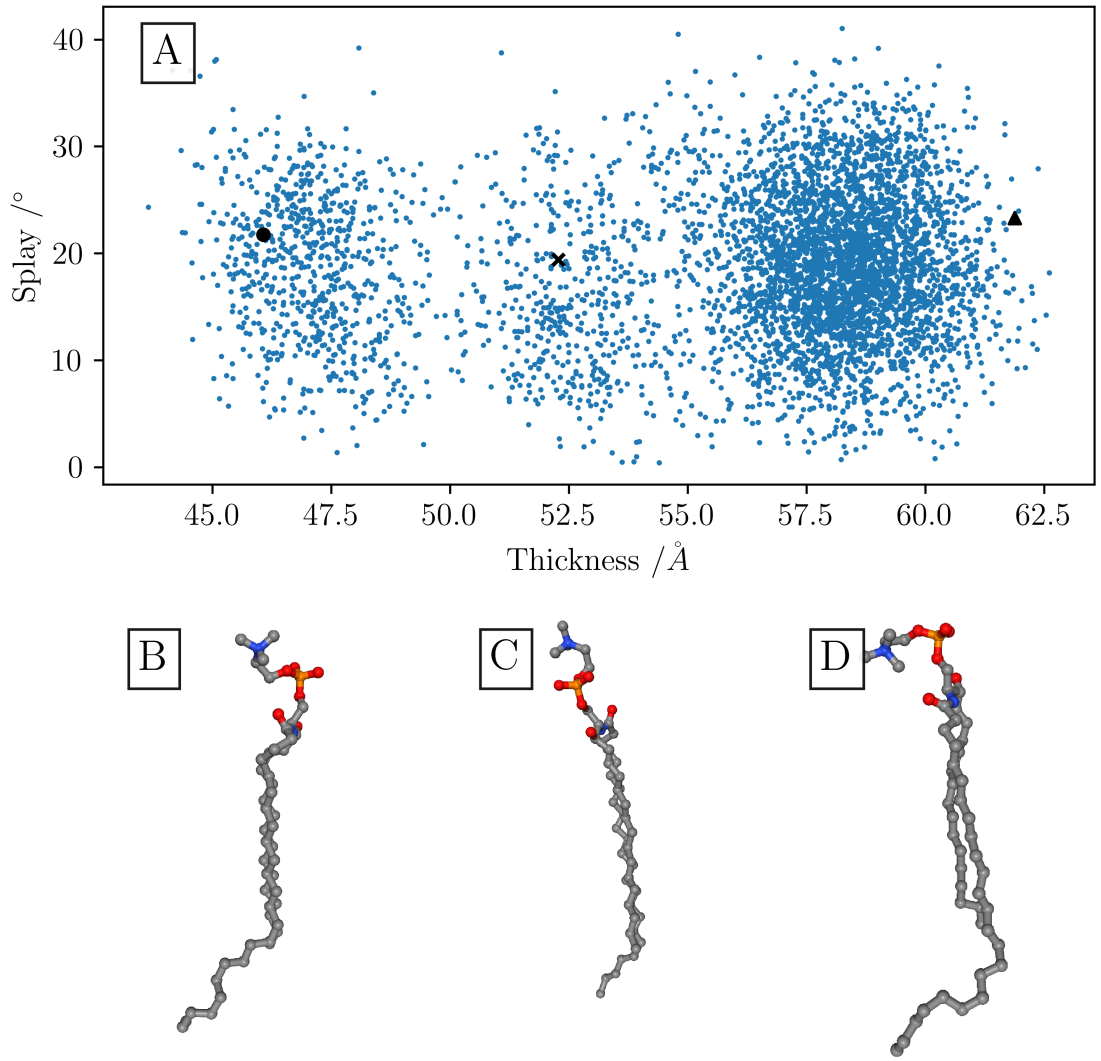

Figure 5.11: Thickness and splay values for a single SM24 lipid across a 500 ns window of the trajectory (A). The lipid structure example from each of the three states visible and have been visualised and the data point they correspond to has been marked by a black circle (B), cross (C) and triangle (D).

5.5 Discussion and conclusions

NMRs, unlike humans, do not regulate there temperatures, instead it is based on the ambient temperature (Buffenstein and Yahav 1991). Assessing the lipid behaviour across the range of probable temperatures for a NMR is key (Holtze et al. 2018). Modelling temperatures more realistic than those above the commonly studied main transition temperature (Arsov et al. 2018), one key component of the NMR lipid extract was studied, SM. SM not only differs in total concentration, as discussed in the previous chapter, but also in the distribution of acyl tail length between NMR and mouse samples. NMR brain lipid extract lipids had more shorter acyl chain, whereas mouse brain lipid extract had longer acyl chains. In all cases where saturated and unsaturated were measured, with the exception of the longest acyl chain (24 carbons), saturated lipids were more common than unsaturated (Figure 4.11).

At 303.15 K, SM at all acyl chain lengths studied formed into the ripple phase, as expected given the main transition temperature for SM16 is approximately 315 K (Arsov et al. 2018). In fact, the temperature of wild captured NMRs (297 K-309 K) was contained within the experimental ripple phase range (297 K-315 K) (Arsov et al. 2018; Holtze et al. 2018).

The ripple phase is characterised by an undulation in the lipids (Figure 5.3) with a major and minor arm of lipids causing a saw-tooth shape. As the acyl chain length and asymmetry increased so too did the visibility of the ripple.

The ripple phase complicates the distributions of properties of the bilayer such as thickness (Figure 5.4), changing the distributions from an expected single distribution to complex multimodal distributions. This more complex bimodal distribution is consistent with the existence of the major and minor arm, and is present in all acyl chain length simulations. Although in the case of the largest acyl tail length, the major peak is the thinner of to two peaks, unlike all other simulations, where the major peak is at a larger thickness. At larger acyl-chain lengths a much wider range of tail conformations (Figure 5.8) becomes apparent, minimising the effect of the tail asymmetry and by allowing each individual lipid to access a wider range of excluded volume shapes.

By alternating headgroup conformation the lipids are also able to exist in different thickness states, rather than just altering the tail conformations (Figure 5.11).

The structure of a lipid molecule is key to the thickness state it occupies, but a better understanding of the metrics to measure this are required. With all this conformation flexibility, some metrics can become misleading when applied to lipids, particularly

those with large tail asymmetries in the ripple phase. The splay angle as measured here is highly susceptible to the position of the terminal carbons and the conformations of the headgroup in the bilayer leading to an inability to distinguish the different states as they are degenerate with respect to the splay angle.

While visualisation of the bilayers and the multimodel distributions of data are clear, attempts to cleanly separate this data proved unsuccessful. Unsupervised machine learning clustering was attempted using a variety of features as inputs. GMM has predominantly been reported here, but attempts were undertaken using a variety of techniques to attempt this including DBSCAN. In all cases attempts to separate the major and minor arm into a two state model, and effectively separate the different peaks in distributions proved unsuccessful either using a single feature (Figure 5.5) or more (Figure 5.7). Especially noticeable at longer chain lengths, was the issues of quantifying the structure of individual lipids to generate useful features for machine learning based classification. Selection of metrics to use as features is highly domain and application specific. Proper identification of these requiring extensive prior understanding of the key features required to able to differentiate the data. By selecting key metrics to attempt to classify the lipids, this can force an incorrect separation on those lipids and fail to identify underlying key features. A more robust structural quantification methodology, requiring lesser prior understanding of the system specific properties is required to eliminate the introduction of bias into the results of structural classifications of lipids.

The assumption that the bilayer is in a two state coexistence might also be flawed, the thickness of lipids has been shown to exist in more than two states when looking at individual lipids (Figure 5.10), which does not just depend on the complex lipid tail conformations available to largely asymmetric lipids (Figure 5.8) but instead can depend on the headgroup conformation instead (Figure 5.11). While these might just be intermediate, metastable states, they can exist for significant time, on the order of microseconds (Figure 5.10).

Chapter 6. Ripple phase lipid structural quantification

6.1 Summary

Quantifying the ripple phase in chapter 5 proved unsuccessful. To simplify this problem and develop a new analysis workflow, molecular dynamics simulations of a simpler, ripple forming lipid, DPPC, were used. In this chapter, a new mixed radial-angular, three-particle correlation function method was applied to lipids for the first time. This metric measures the local structure and when used as the input for an unsupervised machine learning workflow revealed four distinct conformational populations within the single component bilayer. The failure in chapter 5 was a result of looking for a two state model, based on the two regions of a ripple phase bilayer. The two regions of the ripple phase bilayer, the major and minor arm, consist of homogeneous ordered lipid and a heterogeneous mixture of all four lipid compositions respectively.

6.2 Introduction

In the previous chapter it was shown that sphingomyelin (SM) of any chain length forms a ripple phase at physiological and experimental relevant temperatures. The existence of the asymmetric ripple phase was first discovered almost 50 years ago (Tardieu, Luzzati, and Reman 1973). Many of the details of the ripple phase (P'_β) remained unknown until the asymmetry of the ripple was seen to have two sides, a major and minor arm (W. J. Sun et al. 1996). The major arm was gel-like phase (L_o), and the minor arm was fluid-like phase (L_d). However This definition has been debated. The most accurate experimental study to date shows the complexity of the ripple phase (Akabori and Nagle 2015). This study split the minor arm into five different conformational classes. Simulations of ripple phase lipids have been reported, but the molecular structure and conformational components that form the ripple are yet to be resolved.

Attempting to classify the lipids in the previous chapter proved unsuccessful with standard techniques and metrics which proved to be degenerate or extrinsic to the lipid

itself. This was further complicated by the extensive conformational complexity introduced by the long, highly asymmetric lipid tails. In this chapter molecular dynamics (MD) simulations of a simple ripple forming bilayer are undertaken. dipalmitoylphosphatidylcholine (DPPC) was chosen as a simple, well simulated lipid, without any of the additional complexity of SM, specifically avoiding the tail asymmetry, unsaturation in one of the tails, and ability to hydrogen bond within the tails. A new structural metric capable of measure of local structure will be applied for the first time to lipids (Sukhomlinov and Müser 2020). This metric will be coupled with unsupervised machine learning to develop a workflow capable of effectively quantifying the conformational differences of the major and minor arm of the ripple phase.

It is hoped that shedding light on the nature of the ripple phase in this simple model system will provide a starting point for the analysis of more complex biological membranes that show ripple behaviour.

6.3 Methodology

6.3.1 Simulation details

Atomistic MD simulations of single component DPPC lipid bilayers were performed. Systems consisted of 512 DPPC lipids and ∼20000 TIP3P water molecules (Jorgensen et al. 1983). The CHARMM36 forcefield was used (J. Huang et al. 2017). GROMACS 2019.6 was used to perform all simulations (Abraham et al. 2015). Initial membrane structures were generated using the CHARMM-GUI membrane builder (J. Lee, Cheng, et al. 2016). Systems were first energy minimised and equilibrated in the NPT ensemble at a pressure of 1 bar and a temperature of 325K. Production simulations were run using the V-rescale thermostat and the Parrinello-Rahman barostat, with the pressure controlled semiisotropically (Bussi, Donadio, and Parrinello 2007; Parrinello and Rahman 1981). A 2 fs timestep was used and periodic boundary conditions were applied in all directions. A switching function over 1-1.2 nm was used for Lennard-Jones interactions. The particle-mesh Ewald method with a real-space cutoff of 1.2 nm was used for electrostatics (Essmann et al. 1995). Productions simulations were run at 293 K, 298 K, 300 K, 305 K, 310 K, 315 K, 316 K, 317 K, 318 K, 320 K and 325 K. This temperature range was used as it spanned the main phase transition temperature reported for the CHARMM36 forcefield, 317 K (L. Sun and Böckmann 2018). Each bilayer was simulated for at least 500 ns. Size dependence was measured by simulating a further 2 system sizes, 128 lipids and 4096 lipids. The 128 lipid systems were run for at least 1 μs each at 8 different

temperatures: 295 K, 300 K, 305 K, 310 K, 314 K, 317 K, 318 K and 320 K. The 4096 lipid systems were run for 500 ns each at 3 different temperatures: 313 K, 315 K and 317 K.

6.3.2 Analysis details

Visualisation was performed using VMD and data analysis was performed using custom python codes with the MDAnalysis (Gowers et al. 2016), scikit-learn (Pedregosa et al. 2011) and scikit-image libraries (Walt et al. 2014). Principle comonent analysis of the lipid motion was calculated using PCAlipids (Buslaev et al. 2016).

Deuterium order parameter, S_{CD}, measures the ensemble average orientation of the C-H bond vector (θ) with the bilayer normal (z-axis) as

$$S_{\mathrm{CD}} = \frac{1}{2}\langle 3\cos^2\theta - 1\rangle \tag{6.1}$$

Bilayer thickness, the distance between the phosphate atoms in each leaflet, was calculated on a per lipid basis by coupling each lipid with the nearest lipid in the opposite leaflet and taking the phosphate distance in the z-axis

$$T_i = Z_{phosphate,i} - Z_{phosphate,j} \tag{6.2}$$

Area per lipid was calculated accounting for the bilayer undulations, applying a Voronoi diagram area approach with lipids in small patches of 1.5 nm in radius around the lipids mapped onto flat planar sections. The area of each Voronoi cell was calculated using the shoelace formula.

Lipid splay angle was defined as the angle formed between the triangle comprising of the terminal lipid tail atoms with an apex at the carbon near the tail split.

Lipid lateral diffusion was calculated using the Einstein relation (Calandrini, V. et al. 2011). Using the mean squared displacements (MSD) of the lipids with the periodic boundaries removed

$$\mathrm{MSD}(r_d) = \langle \frac{1}{N}\sum_{i=1}^{N} |r_d - r_d(t_0)|^2 \rangle \tag{6.3}$$

the diffusion coefficient was then calculated by fitting the linear region of the MSD curve vs lagtime, τ,

$$D_d = \frac{1}{2d}\frac{d}{d\tau}\mathrm{MSD} \tag{6.4}$$

Practically, this meant a fit from 5 ns to 20 ns lagtime, for the 50 ns trajectories analysed to account for the ballistic region and poor sampling at lower and higher lagtimes respectively.

Distributions of data were calculated using kernel density estimation and the mean value of the property for each lipid across the trajectory timescale. A Gaussian kernel was used with the bandwidth estimated using Scott's rule (Scott 1992).

6.4 Results

6.4.1 Three-particle correlation function to measure local structure

To quantify local structure, a new mixed, radial-angular, three particle correlation function (g_3) was used. Originally introduced by Sukhomlinov and Müser (2020) and Sukhomlinov and Müser (2021) in a different context, it has never been applied to lipids.

In this method, illustrated in Figure 6.1, a triplet of atoms is selected:

1. the central atom (blue), B
2. the nearest neighbour to the central atom (orange), A
3. and, the other atom within the cutoff (red), C

Physically, $g3$ (or in alternative notation $g_3(\vec{r}_{BC}, \theta_{ABC})$) is proportional to the probability of finding the other atom at a distance of r from the central atom when the vectors $\vec{r}_{BC}$ and $\vec{r}_{BA}$ form an angle of θ_{ABC}. Figure 6.1 gives three examples of this using the same central and nearest neighbour atoms in each case.

Here, g_3 was applied on the carbon atoms of the DPPC molecules in two ways: 1) to calculate the bilayer average including both inter- and intra-molecular contributions and 2) to analyse each DPPC molecule individually, only assessing the intra-molecular contributions. For the calculation of g_3, 401 radial and 201 angular bins were used with a cutoff of 7 Å. The cutoff was chosen to be greater than the packing distance (S. O. Smith et al. 1994) to capture the salient structural details. Above a critical value capturing the nearby chain contributions the analysis was not sensitive to the choice of cutoff value. The nearest neighbour distance was determined using the traditional radial distribution function but other criteria can also be used. Figure 6.1 shows three structural details specific to the DPPC carbon atoms. Panels A and B show two cases of bonding within the chosen tail. This is relative to the nearest neighbour; since the

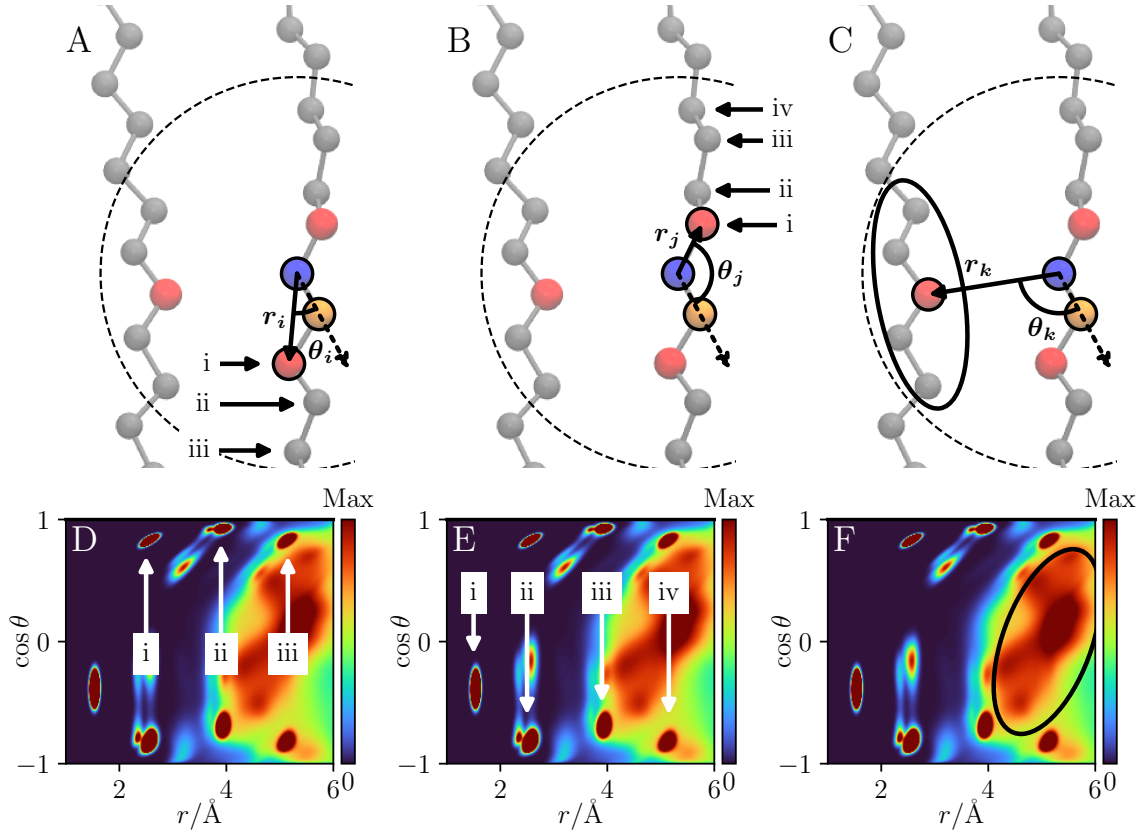

Figure 6.1: Schematic of the mixed angular-radial three-particle correlation function applied to a single carbon in a DPPC acyl chain/lipid tail. A central atom (blue) and its nearest neighbour atom (orange) are selected. The angle formed between the three atoms with the central atom at the apex, θ, and the distances between the central atom and the selected atoms, r, are calculated. This is repeated for all target atoms within the cutoff (dashed line). Three key structural contributions are shown here with an example target atom in red. The 'same-side' tail (A), 'opposite-side' tail (B) and 'other' tail (C). Below each diagram the locations of the main contribution to the probability distribution by each of these different tail contributions have been indicated. The same tail contributions are marked with arrows, labelled showing the peak density and contributing atom (from the central atom shown). The 'other' tail is much more diffuse and contributions from single atoms are less resolvable so this has been indicated by the black ellipse showing the contributed region. The same-side contributions are radially offset relative to the opposite-side because the nearest neighbour atom is not included.

nearest neighbour is not included in the distribution, the same-side contributions are shifted. The distinct peaks in the distributions correspond to the atom n bonds away from the central atom on the opposite side and $n+1$ bonds away on the same side. The first peak in both cases picks up the adjacent atom angular component and hence does not split. For $n \geq 2$, in a bonded chain, there are increased degrees of freedom which allow peak splitting. Panel C shows the packing of other tails. This is the contribution by the carbon atoms not in the same lipid tail as the target central atom, but in another lipid tail packed close to the lipid tail in question.

6.4.2 Lipid clustering and lipid similarity

To compare the g_3 distributions of individual lipids with each other, the mean structural similarity index metric (SSIM) (Wang et al. 2004) was applied. SSIM was originally developed as a metric for determining the similarity of images. Here the images are the g_3 distribution matrices as computed above for each of the individual lipids. SSIM is unique compared to many other metrics in that it combines three quantities to determine the similarity metric and, second, these quantities are evaluated locally.

The three quantities in the original paper were luminance, contrast and structure (Wang et al. 2004). In the case of lipid g_3 probability distributions, the differences in mean probability, standard deviation, and in spatial probability distribution are used. The SSIM, can be defined in each of the local windows as

$$SSIM(x,y) = \frac{(2\mu_x\mu_y + c_1)(2\sigma_{xy} + c_2)}{\left(\mu_x^2 + \mu_y^2 + c_1\right)\left(\sigma_x^2 + \sigma_y^2 + c_2\right)}, \tag{6.5}$$

where x and y refer to the window in each distribution matrix, μ is the window mean, σ^2 is the variance of the window, σ_{xy} is the covariance of the two windows and c_1 and c_2 are small arbitrary correction factors, proportional to the possible data range, introduced to avoid division by zero.

The final SSIM is the average over the local windows,

$$SSIM = \frac{1}{N}\sum_{i=1}^{N} SSIM(x_i, y_i), \tag{6.6}$$

where x_i and y_i are the i^{th} window in matrices x and y, and N is the total number of windows. This was applied to all simulated systems. The data range was set to the maximal density value in all compared g_3 distributions. A window size of 7 bins was used. It was verified that the result was independent of the window size. All lipids

($N_{\text{lipid}} = 5632$) from all temperatures of the 512 lipid systems were used to sample the conformational phase space. This generated N_{lipid} features (similarity scores) for each of the lipids in the system. The features were combined into an $N_{\text{lipid}} \times N_{\text{lipid}}$ similarity matrix. The difference here compared to other works is that other machine learning techniques build feature matrices like this by using predefined distances between predefined atoms (Ziolek et al. 2021; P. Smith, Quinn, and Lorenz 2020; Walter, Ruscher, Benzerara, et al. 2020). Here, the natural length scales emerge spontaneously from the system and its properties via g_3.

6.4.3 Unsupervised machine learning

To identify and extract the underlying clusters from within the individual lipid g_3 structural similarity data, an unsupervised machine learning approach was utilised. After generating the similarity scores, dimensionality reduction was performed by applying the t-distributed stochastic neighbour embedding (t-SNE) which was scaled to have unit variance (Maaten and Hinton 2008). This reduced the similarity matrix to 2-dimensional embedded representation. The unsupervised machine learning clustering algorithm called density-based spatial clustering of applications with noise (DBSCAN) was applied to the 2d data (Schubert et al. 2017). DBSCAN was chosen instead of the commonly used k-means clustering since in DBSCAN the number of clusters is not predefined but emerges from the data (Kriegel, Schubert, and Zimek 2017). Second, and very importantly, in contrast to k-means, DBSCAN is able to find clusters that are non-linearly separable. DBSCAN needs a neighbourhood defined by the parameter ϵ. A value of 0.085 was used here but this will vary based on the system analysed. The selection of a suitable ϵ is key to identifying all the clusters. This value was selected and verified by using the "elbow plots" (Schubert et al. 2017), by visual inspection of the scaled dimensionally reduced data coloured according to the clusters, a plot of the similarity matrix reduced to 2d via principle component analysis (PCA), and confirmed via examination of the g_3 distributions of the lipids. Feature extraction from the clusters was completed by visualising the g_3 distributions within each cluster to determine the locations of density differences. The lipids within each of the clusters were then identified and further analysed. Figure 6.2 summarises the data analysis and clustering process.

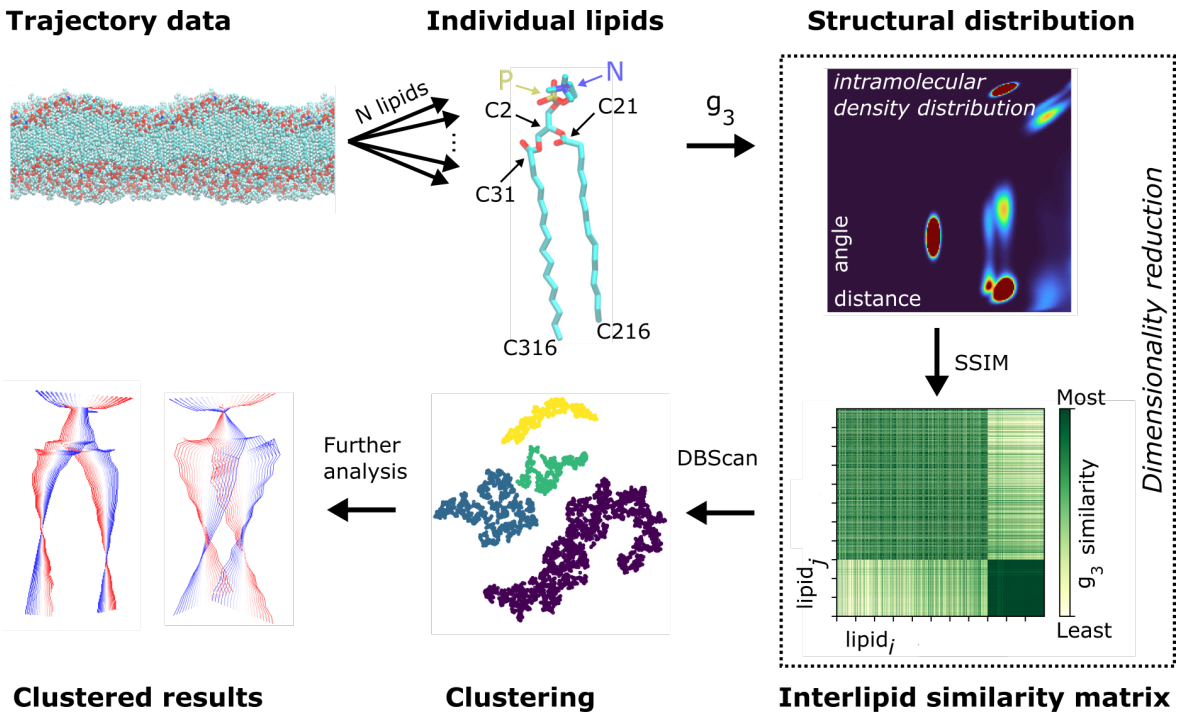

Figure 6.2: Conformational clustering: First each lipid (some of the important atoms are marked) is isolated from the trajectory and g_3 is calculated to quantify the *intramolecular* structure. The mean SSIM, Equation 6.6, of each lipid g_3 distribution is compared with all other lipids. Embedding with t-SNE reduces the matrix of similarity values to a 2d form (from N_{lipids} dimensions). This 2d data is clustered using DBSCAN to find similar conformational groupings. This is mapped back onto the bilayer for further analysis. The similarity matrix shows how similar the distribution of row i is with the distribution of row j. The distinct difference in the final quarter of similarity matrix is a result of passing over the phase transition and the large conformation difference this causes.

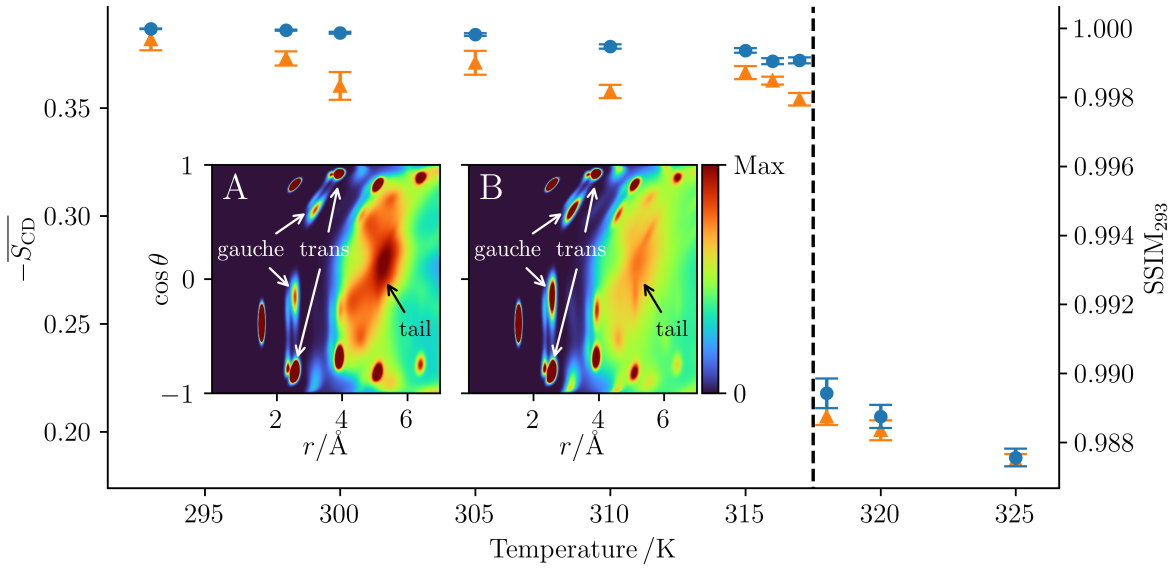

Figure 6.3: Phase transition detected by the average deuterium order parameter, $\overline{S_{CD}}$, (orange) and using g_3 similarity (SSIM) compared with the 293 K system (blue). Both deuterium order parameter and g_3 similarity are able to detect a phase change between 317 K and 318 K. Insets: Probability density distributions for g_3 of the DPPC carbon atoms at 317 K (A) and 318 K (B). The dihedral gauche and trans peaks have been marked along with the contribution by the other tails. Errors estimated by block averaging for the order parameter and by comparing g_3 distribution from multiple 5 ns windows of each simulation.

6.4.4 Structural details from g_3 analysis and the main phase transition

The particular strength of g_3 is that it is able to detect and quantify structural motifs and changes within the DPPC lipid tails without any a priori knowledge of the underlying lipids, structural metrics or connectivity. The algorithm sees merely the system as a monatomic cloud of atoms. Details such as tail bonding, packing and conformational properties emerge spontaneously in the distributions; this analysis could be applied to any molecule or system undergoing structural changes and help aid in the determination of system structure without prior knowledge of the structural properties relevant to the molecule.

Figure 6.3 shows temperature dependence of the conventional deuterium order parameter (S_{CD}) and g_3 using both intra- and inter-molecular contributions. The phase transition temperature detected by these two independent metrics is identical, between 317 K and 318 K. This is slightly above the experimental values of about 314 K (Biltonen and Lichtenberg 1993; Ivanova and Heimburg 2001; W. Chen et al. 2018) but consistent with other simulations using the CHARMM36 force field (L. Sun and Böckmann 2018).

The inset in Figure 6.3 shows g_3 distributions below (317 K) and above (318 K) of the phase transition.

The distributions display two key features: Firstly, and most obviously, the influence of the other tails on the distribution (see the discussion in connection with Figure 6.1). Below the transition, the lipid tails are packing in rigid, fixed positions, producing a sharper peak which drops off at larger distances. Above the transition, this peak becomes much more diffuse, with lower peak height and spread across a longer distance, reducing the level of drop off compared to the more ordered lipids.

The second noticeable difference is in the trans/gauche peaks. Below the transition, the gauche peak density is significantly reduced when compared to above T_{m}. The ordered lipids show less gauche dihedrals in the tails, a well-reported metric for determining the main phase transition.

The phase transition can easily be verified even by visual inspection: As the temperature decreases below T_{m}, it switches from a flat, planar bilayer to a kinked one with regions of different thickness and of asymmetric lengths, Figure 6.4. This was robust and all bilayer sizes and system temperatures below T_{m} adopted a ripple conformation with the exception of one of the 128 lipids systems, which has been noted as a finite size effect (Walter, Ruscher, Gola, et al. 2021).

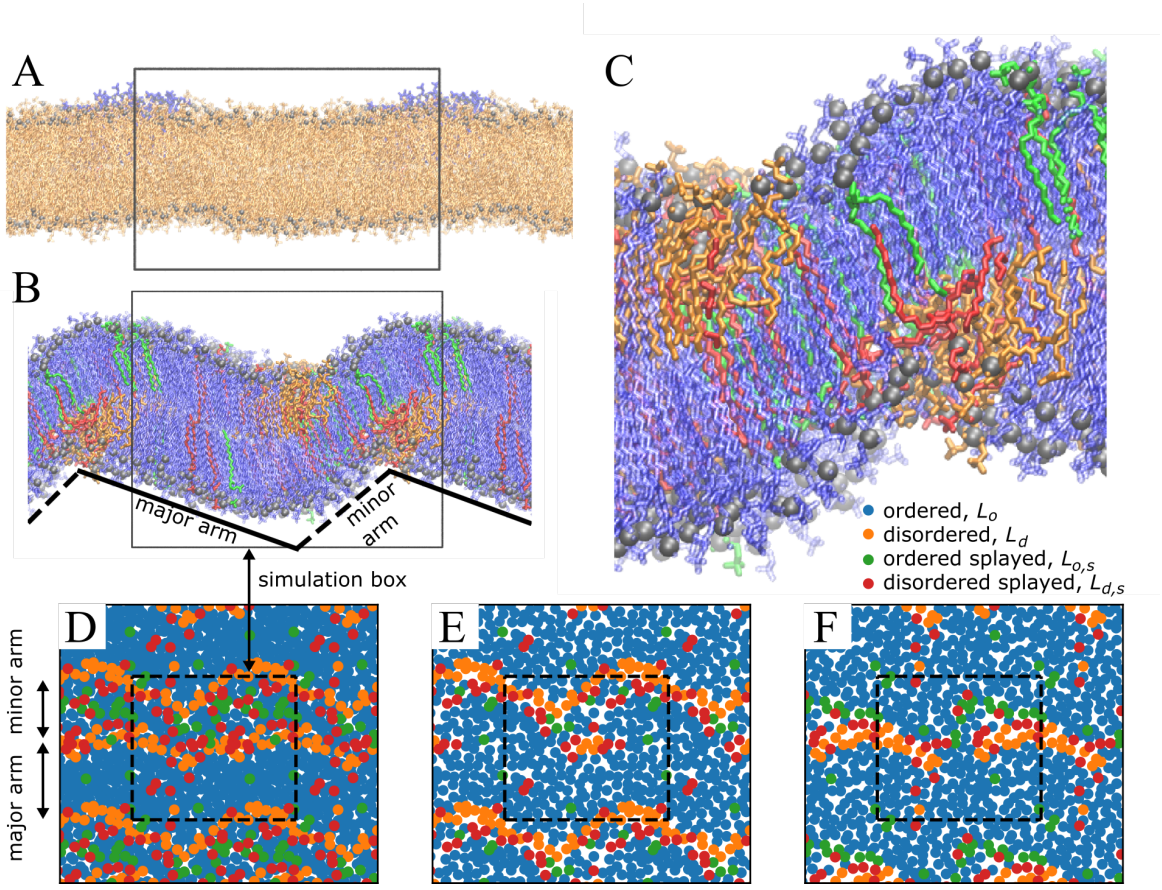

Figure 6.4: Snapshots from simulations at 318 K (A) and 317 K (B), either side of T_m (see Figure 6.3). A zoomed in snapshot of the ripple in the 317 K system (C). All snapshots are coloured according the conformational cluster the lipid has been assigned. The ripple phase features two regions, the major arm (solid line) and the minor (dashed line). (D)-(F): Top views of the 317 K system. (D) Shows the sum of the two leaflets, (E) and (F) the upper and lower leaflet, respectively. The simulation box is indicated in the figures by the box and periodic images are included for clarity. The two arms are asymmetric in length in agreement with experiments and theory (Tardieu, Luzzati, and Reman 1973; W. J. Sun et al. 1996; Lubensky and MacKintosh 1993; Kamal et al. 2011).

6.4.5 The structure of the ripple phase

While the system-wide g_3 is capable of detecting the phase transition on a system-wide scale, the ripple phase is not homogeneous. The structure of the ripple phase can, however, be analyzed by examining the lipid-wise g_3 and comparing the interlipid similarity. Importantly, clustering (using DBScan) revealed four distinct conformational motifs for lipids: disordered (L_d), ordered (L_o), ordered-splayed ($L_\mathrm{o,s}$) and disordered-splayed ($L_\mathrm{d,s}$). These structural motifs emerged in both the 512 and the large 4,096 lipid systems but only three of them appeared in the 128 lipid system, with no differentiation between the ordered-splayed and disordered-splayed lipids; as recently pointed out by Walter et al., finite size effects can be significant in lipid systems (Walter, Ruscher, Gola, et al. 2021). An example of each of these lipid conformations and the g_3 distribution of this is shown in Figure 6.5.

Unsplayed-splayed behaviour is captured by the lipid tail contribution, and the ordered-disordered behaviour by the gauche defects.

The conformational dynamics of each of the lipids clusters was assessed with lipid PCA (Buslaev et al. 2016). Figure 6.6 shows the main component of each of the lipid clusters. The disordered lipids' (L_d and $L_\mathrm{d,s}$) main motion is a scissoring motion, which has been seen in the fluid phase DPPC lipids in a range of force fields (Buslaev et al. 2016). The ordered (L_o and $L_\mathrm{o,s}$) lipids instead have their tails constrained and primarily have a twisting rotational motion. All of the four components are fully distinct.

Above T_m the major component is the widely studied disordered lipid. Below T_m, however, the complex, heterogeneous nature of the ripple phase becomes apparent. With the spatial ordering, laterally within a leaflet and asymmetrically across the leaflets being key to the ripple. The obvious question is: Do these four distinct conformations exist and have finite lifetimes? The number of lipids in each of the clusters as a function of temperature is shown in Figure 6.7A and the time dependence of the splay angle of each of the four species for one of the lipids at 315 K is show in Figure 6.7B. As the Figure shows, all of the components are present in the ripple phase and disappear in the disordered phase. Figure 6.7B further shows that the components are clearly distinct. The disordered lipid (orange), switches its angle as can be expected. The other three components are very clearly present for extended times.

Applying this clustering workflow onto the individual simulations, treating using 5 ns chunks for each distribution still gives rise to the similar cluster behaviour, shown in Figure 6.8. Below the transition temperature a complex mixture of many components

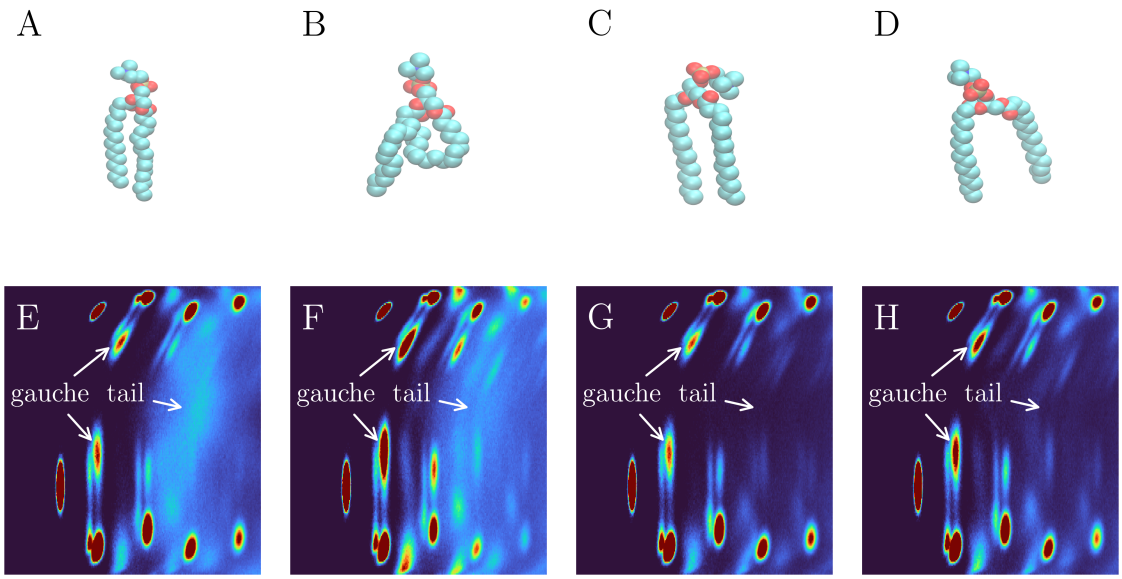

Figure 6.5: Exemplary lipid from each of the identified clusters taken from the 315 K simulation. A linear-ordered lipid (A), disordered lipid (B), splayed-ordered lipids (C) and splayed-disordered lipids (D). The corresponding g_3 distributions are also shown. E, F G, and H correspond to A, B, C, and D respectively. The first gauche defect peaks (up and down tail) have been marked with arrows and the contribution of the other tail peak has been marked with an arrow for clarity.

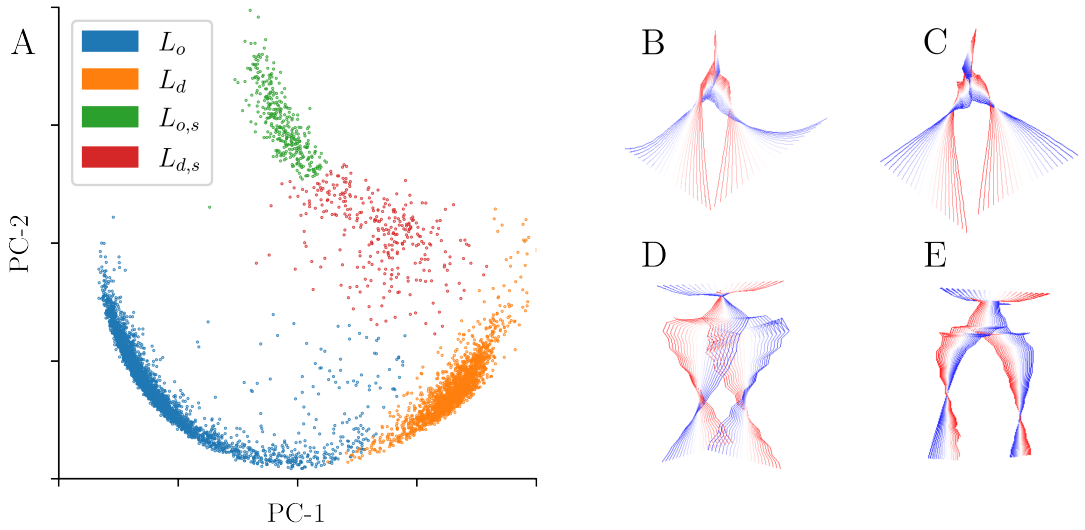

Figure 6.6: Principal component reduction of the lipid similarity matrix showing the first and second components (A). Each of the points represents a lipid and is coloured according to the cluster it was assigned to. Right: The first (most dominant) principal component from the PCA lipids analysis for L_{d} (B), $L_{\mathrm{d,s}}$ (C), L_{o} (D) and $L_{\mathrm{o,s}}$ (E). The key motion in the disordered conformations (B and C) adopt a similar scissoring/splaying tail motion. In contrast, the ordered conformations (D and E) adopt a twisting rotational motion. The colour scheme goes from red-white-blue showing the projected value of the component.

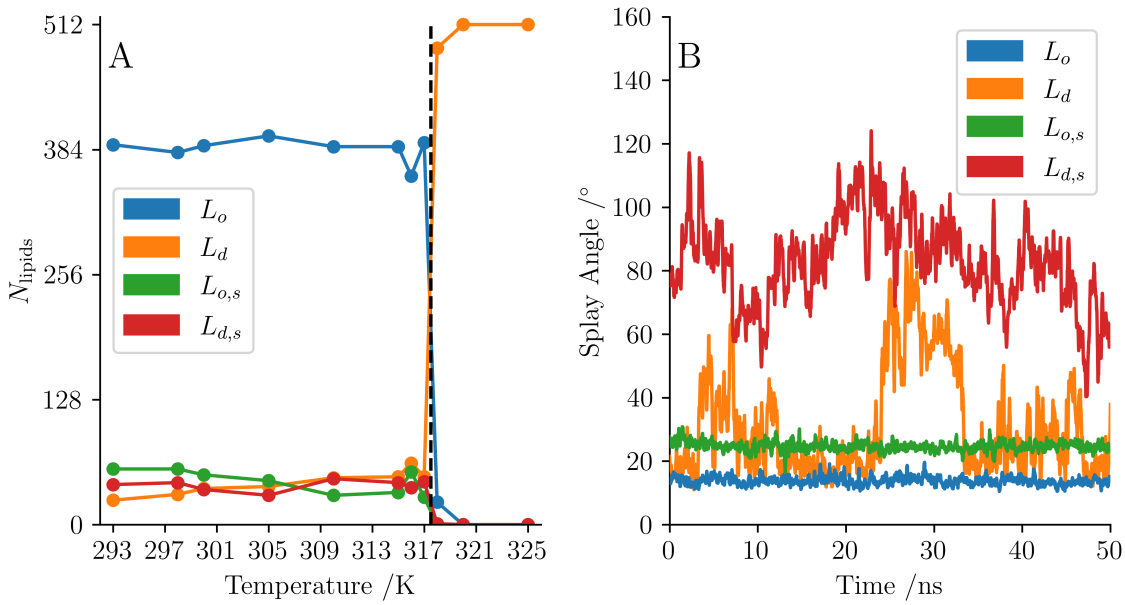

Figure 6.7: Number of lipids in each cluster at each simulation temperature (A) and the splay angle of an example lipid from each of the clusters taken from the 315K simulation (B). The black dashed line shows the phase transition temperature between 317 K and 318 K. The bulk lipid in each case is the linear lipid, ordered below the transition temperature and disordered above. Below T_{m} there exists disordered lipids and splayed lipids. By 320 K the only lipid component is the lipid disordered. The example splay plots show one of the key differences between the clusters, the L_{o} and $L_{\text{o,s}}$ lipids both have a low variance whereas the L_{d} and $L_{\text{d,s}}$ lipids are highly mobile. The L_{d} lipid can bee seen to transition to a splayed conformation briefly at 25 ns but returns to the more linear nature within 10 ns. Since g_3 is a time averaged property the clustering is assigned based on majority of time rather than instantaneous value.

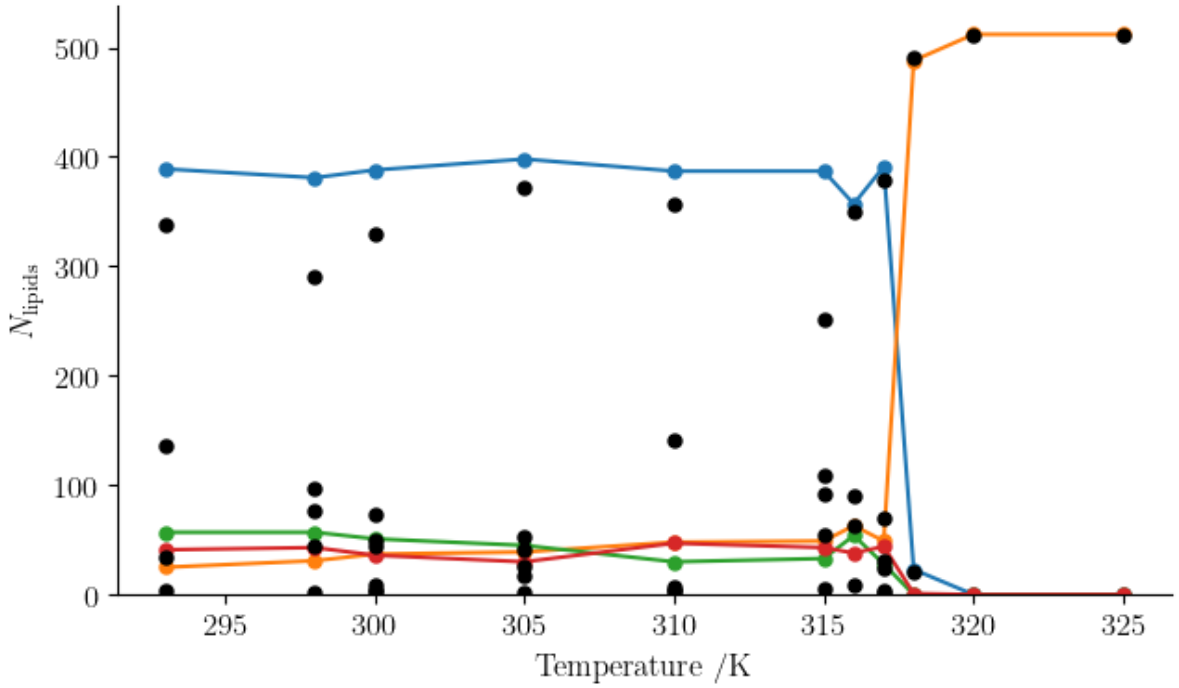

Figure 6.8: Clustering applied to the individual simulations with distributions for each 5 ns trajectory window to increase sampling (black points). Individual results have been overlaid onto the results for the combined clustering. The transition is still easily detected although the exact same clusters do not emerge in most cases. The individual points were normalised by the number of blocks used in the calculation.

exists and above the transition temperature it becomes a single component. The clusters are not exactly the same in most cases and the occurrence of unclustered 'noise' points emerged, this is probably due to the reduced effective sampling compared with the aggregated system clustering in which all lipids were successfully assigned to a cluster. This blocking analysis makes the assumption that the results will be uncorrelated enough to effectively increase the sampling and given a long enough simulation should converge to a similar result. The timescale of each distribution, 5 ns for the individual clustering, 50 ns for the aggregated clustering may also effects the results. The shorter windows will better capture shorter lived transitions such as the ones shown in the splay in Figure 6.7. The shorter windows are not without error, the reduced time means less atom triplets are counted and a coarser distribution grid might be required to allow adequate sampling of the distribution.

6.4.6 Properties of the different ripple phase conformations

The PCA of the lipid motions show the difference in lipid conformations, however how this relates to more standard lipid analysis needs to be seen.

The area per lipid and thickness distributions are shown in Figure 6.9 decomposed into the individual lipid conformation clusters. The complex thickness distribution (Figure 6.9A) shows the splayed lipids contribute to lower thickness areas of the bilayer, whereas the disordered lipids are generally much thicker. The ordered lipids maintain a more complex distribution structure matching that of the overall distribution well. This makes sense considering lipid spatial organisation, whereby ordered lipids occupy are not excluded from the thinner kink of the ripple, but instead make a significant proportion of this since the leaflets components are out of registration, which has been noted experimentally. All of which which can be seen visually in Figure 6.4.

The simpler area per lipid distribution (Figure 6.9B) does not show a drastic change based on cluster decomposition, however this would make sense considering the ripple is likely driven by the conflicting interactions acting on the bilayer, maintaining sufficient head group hydration as the tails become more ordered (Walter, Ruscher, Gola, et al. 2021). By maintaining a constant area per lipid hydration levels can remain consistent.

As a key feature of the lipid conformational cluster differences the lipid splay angle, Figure 6.10, decomposes into the four distinct distributions much more notably. The rigid ordered tails of the ordered and ordered, splayed lipids form sharp, thin peaks. In contrast with this the disordered and disordered, splayed lipids cover a much larger

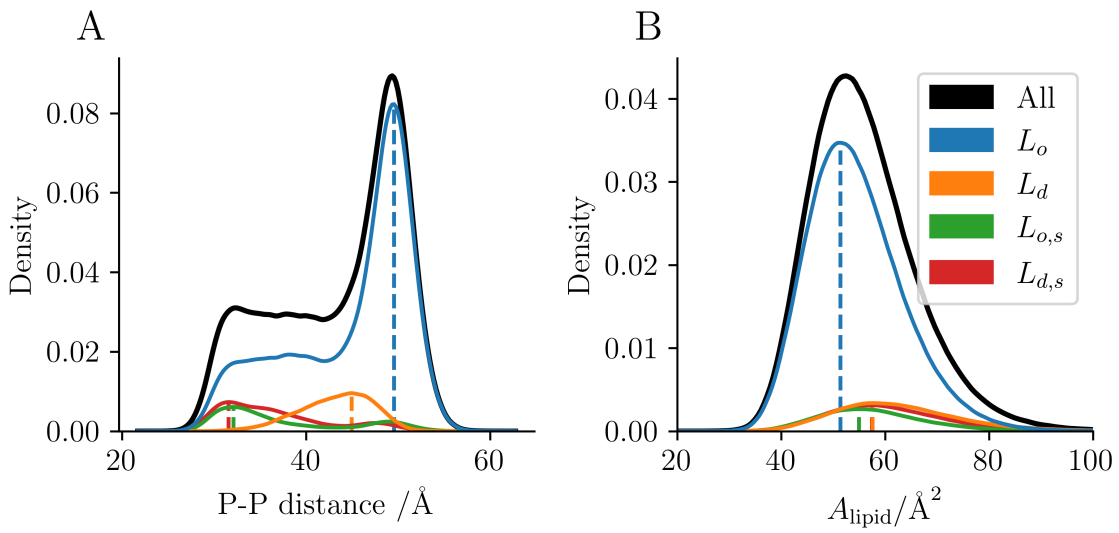

Figure 6.9: Lipid bilayer coupled thickness (A) and area per lipid (B) for the 315 K system. The system properties decomposed into the four conformational clusters. Distinct differences in the thickness distributions of the clusters can be seen with the splayed pair being much thinner, although the liquid ordered lipids are still the bulk component in the thin region of the bilayer. The area per lipid does not decompose as distantly.

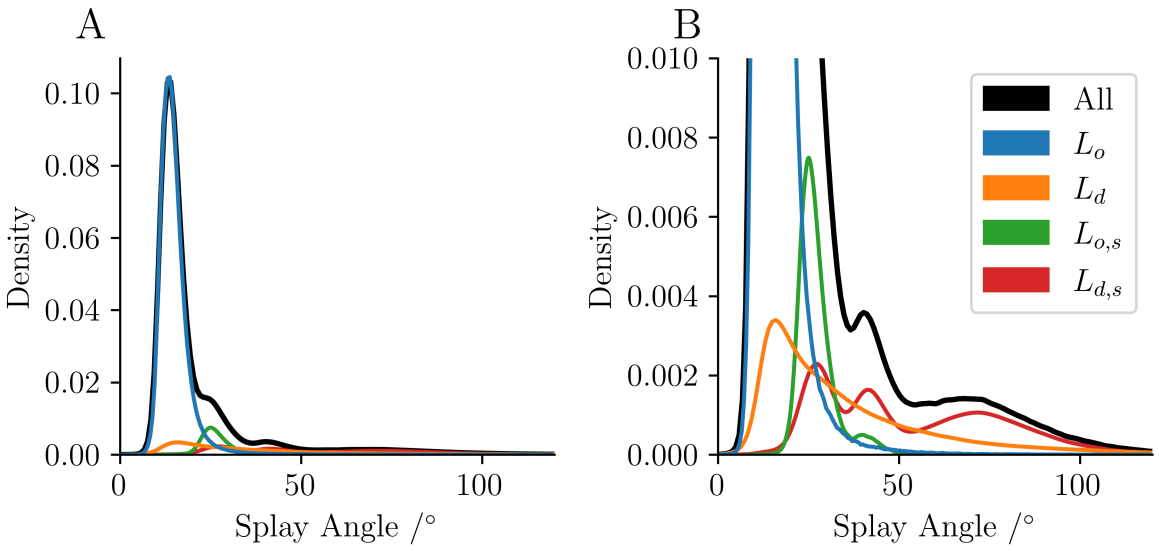

Figure 6.10: Lipid splay angle for the 315 K system (A). A close up of the same distributions showing the split clusters more closely (B). The ordered lipids form sharp, thin peaks and the disordered lipids are much more spread.

range of angles due to the increases variance of the splay of an individual lipid across time. This can be seen in Figure 6.7, where the disordered lipids have a tendency to access a much larger range of splay angles, whereas the ordered lipids are locked into place.

The other key feature, the lipids ordered state is confirmed by calculating the deuterium order parameter for the lipids in each cluster as seen in Figure 6.11. The interfacial nature of the lipids in the splayed group, particularly in the disordered splayed group, can be seen. Bridging between the disordered lipids and the ordered ones, particularly towards the ends of the tails. The disorder at the start of the tails in both ordered and disordered splayed lipids is a result of the splaying. A splayed lipids in one with a 'shoulder', where the upper carbons must deviate from the linear, ordered state to facilitate the splay, this can been seen in Figure 6.5, particularly in panel D.

The diffusion of the different lipid clusters is show, as the MSD, in Figure 6.12. The lipid laternal diffusion is approximated by the phosphate atom MSD (panel A)

Above the main transition temperature, the lateral diffusion coefficient is consistent with similar DPPC simulations (Piggot, Piñeiro, and Khalid 2012).

Below the main transition temperature, the behaviour of the disordered lipids is quite different from those of the other three populations (Figure 6.12). In all simulations

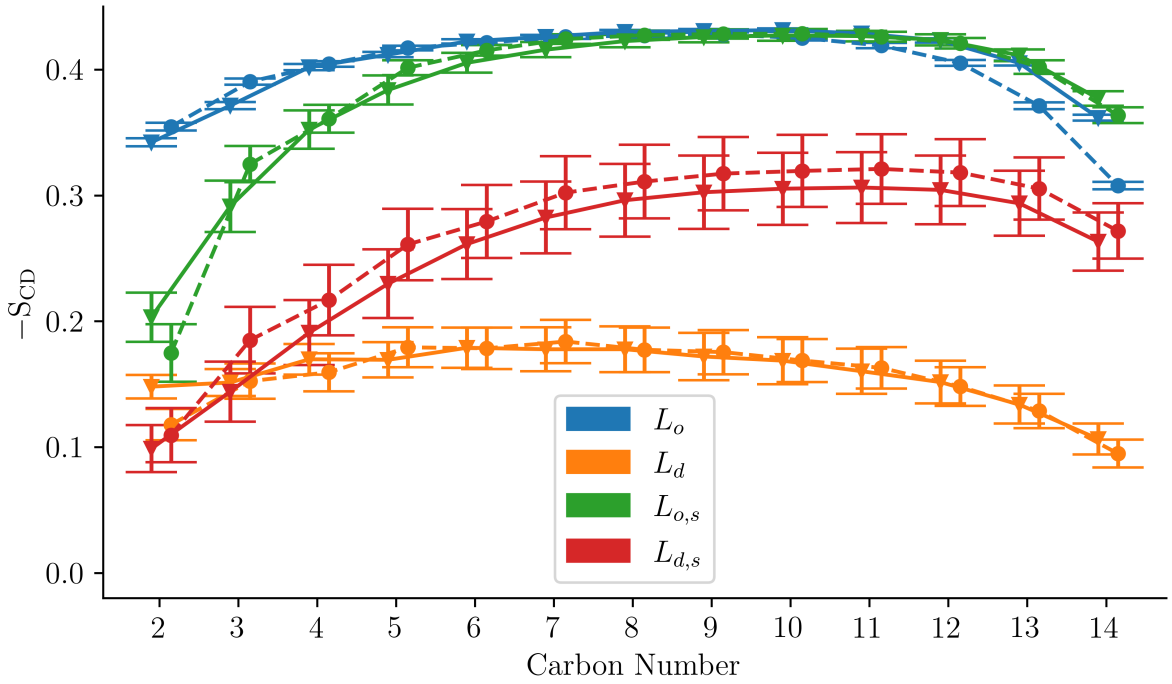

Figure 6.11: Deuterium order parameter for the 315 K system. Each of the conformational clusters along with the system average have been plotted. Both tails have been plotted, distinguished by the solid and dashed lines. There is a separation between the ordered and disordered clusters, although at the ends of the lipid tails the disordered, splayed lipid has a surprising level of order. Error bars show the standard error of the mean across all lipids.

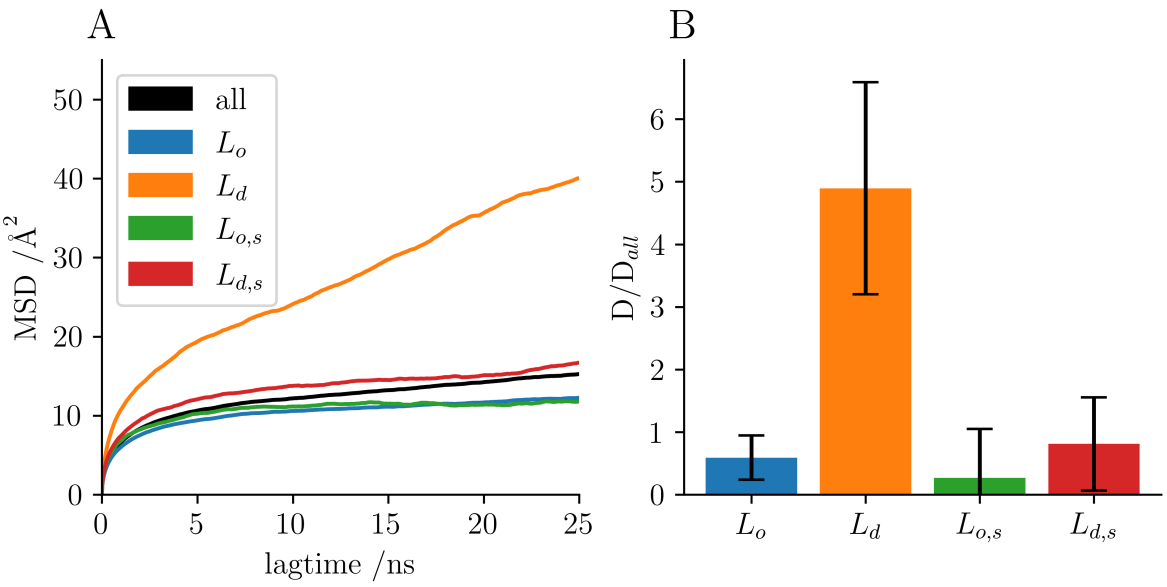

Figure 6.12: MSD for each of the conformational clusters for the phosphate atoms (A) and the ratio of the lateral diffusion coefficient of each cluster relative to the diffusion coefficient of all the lipids (B). Amongst the four clusters the diffusion is vastly different. With the disordered lipid phosphate atoms diffusing at a much greater rate compared to the other more similar clusters. Error estimated from the difference of the diffusion coefficients obtained from fits over the two halves of the fit interval of the MSD curves.

the diffusion coefficient of the disordered lipids is much lower than that of disordered lipids above the transition temperature. However, the disordered lipids have a much higher diffusion coefficient than the other lipid populations of the same bilayer.

The naive analysis of all lipids, rather than the identified clusters gives drastically different results for some of the lipids in the system in all cases below the transition temperature. Drastically under representing the disordered lipids, but also over representing the ordered bulk component.

6.5 Discussion and conclusions

A new radial-angular three-particle correlation function (g_3) in combination with unsupervised machine learning has been applied to examine the phase transitions in DPPC lipid bilayers using data from atomistic MD simulations. The analysis revealed the presence of four distinct conformational populations of lipids in the ripple phase of DPPC lipid bilayers. The expected ordered and disordered lipids are found along with their splayed equivalents. The analysis using g_3 showed distinct differences in their gauche distribution and tail packing. Principle component analysis (PCA) further confirmed the existence of these four lipid groups. Finite size effects influenced smaller (128 lipid) bilayers and only three clusters were identified, with no differentiation between the ordered-splayed and disordered-splayed. The splayed lipids exist to stabilise the interface mismatch. In order to cover the interface region in smaller bilayer systems, a higher ratio of the lipids must be melted to splayed disordered. This was not the case in the small 128 lipid systems and so those systems were influenced by finite size effects.

In a very recent study Walter, Ruscher, Benzerara, et al. (2020) also applied machine learning to study the main phase transition in DPPC bilayers. One fundamental difference is that they used supervised machine learning and trained their algorithm to distinguish between two pre-defined lipid conformations, fluid or gel. In this work using unsupervised machine learning, the number of lipid conformational categories was not fixed beforehand but emerged from data.

The structure of the ripple phase has remained an open question and in their study Akabori and Nagle (2015) state that the ripple structure that emerges from their scattering data does not agree with the ripple consisting of interdigitating ordered lipids as has been reported by several previous simulations (Vries et al. 2005; Lenz and Schmid 2007). Akabori and Nagle (2015) dismissed the possibility of interdigitation of ordered lipids being the dominant behaviour in the thinner minor arm since the observed electron density is inconsistent with that scenario in large enough of scale. Instead, they proposed that the major arm consists of the usual ordered gel-like lipids and then hypothesised that the minor arm has five other lipid types of variable lengths and packing. Those lipids were classified as "more fluid than the gel phase" or intermediate, and suggested to exist on both sides of the minor arm. They did not elaborate these five additional lipid types further.

The results in this chapter resolve the above controversy and provide a detailed picture of the ripple structure. First of all, as discussed above, conformational clustering

using unsupervised machine learning (Figure 6.2) revealed four distinct classes of lipids whose existence were subsequently verified by PCA. As Figures 6.4B,C show, disordered (orange) and disordered splayed (red) lipids cluster are found in the groove region of the ripple only. This is unlike to what has been suggested by Akabori and Nagle (2015) based on x-ray scattering and Khakbaz and Klauda (2018) based on their MD simulations using 72 lipids that the two sides of the ripple are symmetric in terms of lipid conformations (the two arms are asymmetric). As evident in Figure 6.4, the convex part has the usual ordered (blue) and some ordered splayed lipids (green) with some of them also distributed in the planar, gel-like regions. Furthermore, outside the disordered region, the minor arm consists of the usual ordered lipids (blue). Figures 6.4D-F also reveal that splayed lipids, both ordered and disordered splayed tend to be present only on the minor arm side of ripple. The splayed lipids act as intermediates between the ordered and disordered lipids. The disordered-splayed lipids often adopt a conformation with one of the tails relatively ordered and the other much more fluid, seemingly half transitioned, forming an interfacial layer in the ripple. As Figure 6.4C also shows, there is some interdigitation but that presence of the fluid phase is the key here and clarifies the picture of Akabori and Nagle (2015). In addition, Figures 6.4E-F show that the idea of dislocation lines consisting of lipids in the fluid phase put forward by Heimburg (2000) over 20 years ago is indeed a very good description of the ripple phase.

The existence of the four distinct classes of lipids and their unique distribution in the convex and concave side of the ripple also shows the shortcomings of current leading theories (Goldstein and Leibler 1988; Lubensky and MacKintosh 1993; Kamal et al. 2011). While several of them do predict the ripple phase and the existence of the two arms of different lengths, none of them addresses the ripple structure or the asymmetry across the ripple. Coupling between the two leaflets and incorporation of the behaviour of individual lipids appear to be the major issues that need to be addressed in future theories.

Analysis of the individual clusters gives insight into the importance of this type of analysis rather than just assuming a homogeneous mixture of lipids. The behaviour of the different clusters of lipids is distinct and different. The tail mobility of these different clusters is vastly different, with the disordered lipids, splayed and not, having much more mobile tails (Figure 6.7) and lower order (Figure 6.11). The diffusion of the lipids is also vastly different. Disordered lipids diffuse at a much greater rate than the other lipids (Figure 6.12). This vastly increased diffusion occurs within channel-like

regions along the length of the bilayer (Figure 6.4). How this alters the interactions of the ripple phase lipids and other molecules (e.g. cholesterol or peptides) such as their partitioning and permeability are unknown.

Chapter 7. Conclusions

Lipids from the naked mole-rat (NMR) show extensive phase separation, not seen in the lipids of other model animal extract systems like mouse and pig. This phase separation was shown to occur in lung, skin and kidney lipids. Mechanically the phases behave the same between samples,the main difference being the amount of phase separation. When exposed to peroxidation however this phase separation does not seem to offer protection compared with the mouse model. The extensive phase network does restructure based on low amounts of damage and holes form with increased damage. In comparison the mouse bilayer seems undamaged and unaltered.

In DOPC/DPPC lipid bilayers, the phase separation acts in protective manner against amyloid beta (Aβ). The Aβ avoids the ordered phase and instead accumulates in the disordered phase. It was hypothesised that since the NMR brain lipids also exhibit extensive phase separation they would also show this behaviour. With the liquid ordered domains acting as a passive protective mechanism. This was not the case and exposure to both human and NMR sequence Aβ completely fragmented the bilayers. There seemed to be no restructuring like seen in the case of peroxidation and the damage was much more substantial. In the peroxidation case the bilayer remains mostly continuous with defect-like holes formed. The Aβ completely fragmented the bilayer destroying much larger areas. As with the peroxidation the mouse brain lipid bilayers were largely unaffected with the bilayer remaining intact when exposed to both human and NMR Aβ. There were signs of interaction unlike in the peroxidation case. The mouse brain lipid bilayers became pitted, with defect appearing on the surface, but these were not deep enough to be holes through the bilayer. While NMRs are able to live with high amounts of Aβ the results here indicate that it is not due to simple mechanical properties of their brain lipids that they have this resistance. Unexpectedly, NMR lung lipids did not show the same destruction when exposed to human Aβ, instead they behave like the simple model system, with the Aβ interacting, but not destroying, the disordered phase, and avoiding the ordered phase.

Two lipid species heavily linked with Alzheimer's disease and Aβ are also some of the key differences between mouse and NMR brain lipids: sphingomyelin (SM) and cholesterol (e.g. Varma et al. 2018; Habchi et al. 2018). NMR brain lipids are much more abundant with cholesterol, which explains the much more highly ordered lipids and raft formation. In contrast, SM is much less abundant in NMR brain lipids, with a distribution containing more shorter chain lipids than the mouse brain lipids.

Molecular dynamic simulations of single component SM bilayers, across the same tail distribution range measured experimentally in NMR and mouse brain lipid extracts reveal that at all tail lengths, SM forms the undulating ripple phase at 303.15 K. The effect of the increasing tail asymmetry on the conformational complexity of the ripple phase SM showed shortcomings in the common naive analysis, standard in the analysis of fluid phase bilayers, when applied to the ripple phase. Most bilayer structural properties varied linearly or remained constant with increasing chain length, and no drastic differences were seen such as phase transition type discontinuities. Probability distributions of these further exemplified the complexity of the ripple phase bilayer, showing that these were complex distributions and not the more simple Gaussian distributions you would expect in the more commonly studied fluid phase lipid bilayers.

Attempting to cluster the individual lipids into two states, the ordered and disordered coexistence, in the ripple did not prove successful and was unable to convincingly separate other standard data metrics, such as splay angle and deuterium order parameter. Assessing single individual lipids and their properties seems to indicate more than a two state system, for example one lipid appeared to occupy three different thickness states across a 500 ns window.

A simpler, ripple phase system was approached, DPPC, removing the complexity due to the SM tail asymmetry, the ability to hydrogen bond, and unsaturation within the lipid tail.

A new mixed, radial-angular three-particle distribution function, g_3, was applied to measure the local structure of the tails of each individual lipid across a range of temperatures spanning the ripple-fluid transition. Although lower temperature simulations than the experimental pretransition were simulated (Riske et al. 2009), the gel phase did not emerge at the larger system size (512 lipids) used in this work in agreement with recent simulations showing the gel phase (as it currently presents in simulations) might be a result of finite size effects (Walter, Ruscher, Gola, et al. 2021). Normally, separation into clusters is a complex multidimensional task requiring complex

system knowledge to select the correct metrics to capture this behaviour. g_3 requires no a priori knowledge of the possible conformations or key metrics to measure the lipid structure and was able to detect two key structural features in the DPPC tails: gauche defects and tail separation. Applying an unsupervised machine learning clustering pipeline to these local structure measurements, four distinct conformational clusters emerged, not the expected two clusters. Ordered and disordered lipids in both a splayed and linear conformation. The spatial distribution of these lipid conformations within the ripple phase major and minor arms reveal that the ripple phase does not exist with a large number of disordered lipids in coexistence with ordered lipids. Instead, the ripple phase is a coexistence of an ordered phase and a complex mixed phase (which also includes ordered lipids). The minor arm consisting of a significant portion of the same lipid conformation as the major arm helps explain why the more standard analysis of the SM was unsuccessful. The complex lipid mixture was masking key details of the individual lipids. The g_3-clustering conformational analysis is not specific to lipids and could be applied to a wide range of complex multi-conformational molecules for example polymers and proteins or complex biological systems such as mixed lipid composition lipid bilayers and lipid bilayer embedded proteins.

7.1 Future Work

Many avenues of additional work have arisen from the work presented in this thesis.

The peroxidation resistance of cell lines originating from different ages naked mole-rats and mice could be compared to better assess if the behaviour is universal across the entire lifespan of the animals. Further quantification of peroxidation damage across all systems, the model DPPC/DOPC and NMR skin and kidney lipids could be undertaken to assess if the behaviour is consistent across the different organs in each species and correlates with phase separation observed in them. The different morphologies of the phase separation within the NMR lipid supported lipid bilayers (SLBs) and the effect this has on the peroxidation could also be further assessed.

The differing behaviour between NMR brain lipid extract and NMR lung cell line lipid and model DOPC/DPPC SLBs has been shown but, as with the peroxidation, additional quantification and across the full range of organs could be undertaken.

The link between peroxidation and Alzheimer's disease (AD) has been reported in the literature so the effect of Aβ on peroxidation induced restructured SLBs could further reveal insight into the NMR resistance to neurodegenerative disease.

The work shown in chapter 6 focused on a single window of time, however this analysis can be easily extended to include many windows and allow for the analysis of the dynamics of these lipids such as the transition probability between them and to provide insight into the nature of the process of the main phase transition.

The lipid gel phase was not found in the larger DPPC systems despite simulating over 10 K below the expected pretransition (gel to ripple) temperature. An assessment of the behaviour of common forcefields ability to replicate the phase behaviour of lipid bilayers for larger numbers of lipids could be completed. In the pursuit of simulating more physiologically accurate bilayers, larger systems are required and finite size driven effects need to be understood and corrected.

The undulating ripple emerges in small 128 lipid SM systems in chapter 5, however the importance of finite size effects on the ripple phase was discussed in chapter 6, larger bilayers consisting of more lipids could be simulated and the g_3-clustering analysis workflow developed in chapter 6 could be applied to these differing tail asymmetry systems to quantify the structures identified in the chapter such as snorkelling lipids and measure any deviation from the simpler DPPC system analysed in chapter 6.

To better understand the NMR bilayer this analysis could be applied to more complex bilayers, for example, initially including mixtures of cholesterol, DPPC and SM, then building to more complete systems with a more physiologically representative complex composition. Again this should be wary of the system size as the absolute number of each type of lipid should remain high enough to be able to effectively ascertain if any behaviour is specific to individual lipid types, such as if the lipid tail asymmetry or unsaturation allows for a more diverse range of conformations as expected based on the SM results.

Once a better understanding of the complex membrane is complete, bilayers interacting with Aβ or consisting of peroxidated lipids can then be analysed with the same workflow to quantify and induced conformational changes within the lipids and to gain further insight and elucidate a better understanding of the experimental results shown in chapter 3 and 4.

Bibliography

Abraham, M. J. et al. (2015). "GROMACS: High performance molecular simulations through multi-level parallelism from laptops to supercomputers". *SoftwareX* 1-2, pp. 19–25. DOI: 10.1016/j.softx.2015.06.001.

Akabori, K. and Nagle, J. F. (2015). "Structure of the DMPC lipid bilayer ripple phase". *Soft Matter* 11 (5), pp. 918–926. DOI: 10.1039/C4SM02335H.

Alves, G. et al. (2008). "Epidemiology of Parkinson's disease". *Journal of Neurology* 255.SUPPL. 5, pp. 18–32. DOI: 10.1007/s00415-008-5004-3.

Amaro, M. et al. (2016). "GM1 Ganglioside Inhibits β-Amyloid Oligomerization Induced by Sphingomyelin". *Angewandte Chemie - International Edition* 55.32, pp. 9411–9415. DOI: 10.1002/anie.201603178.

Andersen, H. C. (1980). "Molecular dynamics simulations at constant pressure and/or temperature". *The Journal of Chemical Physics* 72.4, pp. 2384–2393. DOI: 10.1063/1.439486.

Andziak, B., O'Connor, T. P., and Buffenstein, R. (2005). "Antioxidants do not explain the disparate longevity between mice and the longest-living rodent, the naked mole-rat". *Mechanisms of Ageing and Development* 126.11, pp. 1206–1212. DOI: 10.1016/j.mad.2005.06.009.

Andziak, B. and Buffenstein, R. (2006). "Disparate patterns of age-related changes in lipid peroxidation in long-lived naked mole-rats and shorter-lived mice". *Aging Cell* 5.6, pp. 525–532. DOI: 10.1111/j.1474-9726.2006.00246.x.

Andziak, B., O'Connor, T. P., et al. (2006). "High oxidative damage levels in the longest-living rodent, the naked mole-rat". *Aging Cell* 5.6, pp. 463–471. DOI: 10.1111/j.1474-9726.2006.00237.x.

Arimon, M. et al. (2015). "Oxidative stress and lipid peroxidation are upstream of amyloid pathology". *Neurobiology of Disease* 84, pp. 109–119. DOI: 10.1016/j.nbd.2015.06.013.

Arsov, Z. et al. (2018). "Phase behavior of palmitoyl and egg sphingomyelin". *Chemistry and Physics of Lipids* 213, pp. 102–110. DOI: 10.1016/j.chemphyslip.2018.03.003.

Attwood, S. J., Choi, Y., and Leonenko, Z. (2013). "Preparation of DOPC and DPPC Supported Planar Lipid Bilayers for Atomic Force Microscopy and Atomic Force Spectroscopy". *International Journal of Molecular Sciences* 14.2, pp. 3514–3539. DOI: 10.3390/ijms14023514.

Ayala, A., Muñoz, M. F., and Argüelles, S. (2014). "Lipid Peroxidation: Production, Metabolism, and Signaling Mechanisms of Malondialdehyde and 4-Hydroxy-2-Nonenal". *Oxidative Medicine and Cellular Longevity* 2014. Ed. by K. V. Ramana, p. 360438. DOI: 10.1155/2014/360438.

Azouz, M. et al. (2019). "Membrane domain modulation of Aβ1–42 oligomer interactions with supported lipid bilayers: an atomic force microscopy investigation". *Nanoscale* 11 (43), pp. 20857–20867. DOI: 10.1039/C9NR06361G.

Banerjee, S. et al. (2020). "Interaction of Aβ42 with Membranes Triggers the Self-Assembly into Oligomers". *International Journal of Molecular Sciences* 21.3. DOI: 10.3390/ijms21031129.

Bárcena, C. et al. (2018). "Methionine Restriction Extends Lifespan in Progeroid Mice and Alters Lipid and Bile Acid Metabolism". *Cell Reports* 24.9, pp. 2392–2403. DOI: 10.1016/j.celrep.2018.07.089.

Batzli, K. M. and Love, B. J. (2015). "Agitation of amyloid proteins to speed aggregation measured by ThT fluorescence: A call for standardization". *Materials Science and Engineering: C* 48, pp. 359–364. DOI: 10.1016/j.msec.2014.09.015.

Bauer, P., Hess, B., and Lindahl, E. (2022). *GROMACS 2022 Manual*. DOI: 10.5281/zenodo.6103568.

Berendsen, H. J. C. et al. (1984). "Molecular dynamics with coupling to an external bath". *The Journal of Chemical Physics* 81.8, pp. 3684–3690. DOI: 10.1063/1.448118.

Biltonen, R. L. and Lichtenberg, D. (1993). "The use of differential scanning calorimetry as a tool to characterize liposome preparations". *Chemistry and Physics of Lipids* 64.1, pp. 129–142. DOI: 10.1016/0009-3084(93)90062-8.

Blennow, K., Leon, M. J. de, and Zetterberg, H. (2006). "Alzheimer's disease". *Lancet* 368.9533, pp. 387–403. DOI: 10.1016/S0140-6736(06)69113-7.

Brookmeyer, R. et al. (2018). "Forecasting the prevalence of preclinical and clinical Alzheimer's disease in the United States". *Alzheimer's and Dementia* 14.2, pp. 121–129. DOI: 10.1016/j.jalz.2017.10.009.

Brown, A. M. and Bevan, D. R. (2017). "Influence of sequence and lipid type on membrane perturbation by human and rat amyloid β-peptide (1–42)". *Archives of Biochemistry and Biophysics* 614, pp. 1–13. DOI: 10.1016/j.abb.2016.11.006.

Brügger, B. (2014). "Lipidomics: Analysis of the Lipid Composition of Cells and Subcellular Organelles by Electrospray Ionization Mass Spectrometry". *Annual Review of Biochemistry* 83.1, pp. 79–98. DOI: 10.1146/annurev-biochem-060713-035324.

Buchoux, S. (2016). "FATSLiM: a fast and robust software to analyze MD simulations of membranes". *Bioinformatics* 33.1, pp. 133–134. DOI: 10.1093/bioinformatics/btw563.

Buffenstein, R. and Yahav, S. (1991). "Is the naked mole-rat Hererocephalus glaber an endothermic yet poikilothermic mammal?" *Journal of Thermal Biology* 16.4, pp. 227–232. DOI: 10.1016/0306-4565(91)90030-6.

Buffenstein, R. and Jarvis, J. U. M. (2002). "The Naked Mole Rat–A New Record for the Oldest Living Rodent". *Science of Aging Knowledge Environment* 2002.21, pe7–pe7. DOI: 10.1126/sageke.2002.21.pe7.

Buffenstein, R. (2008). "Negligible senescence in the longest living rodent, the naked mole-rat: Insights from a successfully aging species". *Journal of Comparative Physiology B: Biochemical, Systemic, and Environmental Physiology* 178.4, pp. 439–445. DOI: 10.1007/s00360-007-0237-5.

Buffenstein, R., Lewis, K. N., et al. (2020). "Probing Pedomorphy and Prolonged Lifespan in Naked Mole-Rats and Dwarf Mice". *Physiology* 35.2, pp. 96–111. DOI: 10.1152/physiol.00032.2019.

Buslaev, P. et al. (2016). "Principal Component Analysis of Lipid Molecule Conformational Changes in Molecular Dynamics Simulations". *Journal of Chemical Theory and Computation* 12.3, pp. 1019–1028. DOI: 10.1021/acs.jctc.5b01106.

Bussi, G., Donadio, D., and Parrinello, M. (2007). "Canonical sampling through velocity rescaling". *The Journal of Chemical Physics* 126.1, p. 014101. DOI: 10.1063/1.2408420.

Butterfield, D. and Lauderback, C. M. (2002). "Lipid peroxidation and protein oxidation in Alzheimer's disease brain: potential causes and consequences involving amyloid

β-peptide-associated free radical oxidative stress". *Free Radical Biology and Medicine* 32.11, pp. 1050–1060. DOI: 10.1016/S0891-5849(02)00794-3.

Calandrini, V. et al. (2011). "nMoldyn - Interfacing spectroscopic experiments, molecular dynamics simulations and models for time correlation functions". *JDN* 12, pp. 201–232. DOI: 10.1051/sfn/201112010.

Calhoon, E. A., Ro, J., and Williams, J. B. (2015). "Perspectives on the membrane fatty acid unsaturation/pacemaker hypotheses of metabolism and aging". *Chemistry and Physics of Lipids* 191, pp. 48–60. DOI: 10.1016/j.chemphyslip.2015.08.008.

Canale, C. et al. (2018). "Amyloid and membrane complexity: The toxic interplay revealed by AFM". *Seminars in Cell & Developmental Biology* 73, pp. 82–94. DOI: 10.1016/j.semcdb.2017.08.046.

Capone, R. et al. (2012). "Probing Structural Features of Alzheimer's Amyloid-β Pores in Bilayers Using Site-Specific Amino Acid Substitutions". *Biochemistry* 51.3, pp. 776–785. DOI: 10.1021/bi2017427.

Cappella, B. and Dietler, G. (1999). "Force-distance curves by atomic force microscopy". *Surface Science Reports* 34.1, pp. 1–104. DOI: 10.1016/S0167-5729(99)00003-5.

Castellani, R. J., Plascencia-Villa, G., and Perry, G. (2019). "The amyloid cascade and Alzheimer's disease therapeutics: theory versus observation". *Laboratory Investigation* 99.7, pp. 958–970. DOI: 10.1038/s41374-019-0231-z.

Castro, M. A., Hadziselimovic, A., and Sanders, C. R. (2019). "The vexing complexity of the amyloidogenic pathway". *Protein Science* 28.7, pp. 1177–1193. DOI: 10.1002/pro.3606.

Chen, W. et al. (2018). "Determination of the Main Phase Transition Temperature of Phospholipids by Nanoplasmonic Sensing". en. *Sci. Rep.* 8.1, pp. 1–11. DOI: 10.1038/s41598-018-33107-5.

Chen, Z. and Zhong, C. (2014). "Oxidative stress in Alzheimer's disease". *Neuroscience Bulletin* 30.2, pp. 271–281. DOI: 10.1007/s12264-013-1423-y.

Chishti, M. et al. (2001). "Early-onset Amyloid Deposition and Cognitive Deficits in Transgenic Mice Expressing a Double Mutant Form of Amyloid Precursor Protein 695*". *Journal of Biological Chemistry* 276.24, pp. 21562–21570. DOI: 10.1074/jbc.M100710200.

Chiti, F. and Dobson, C. M. (2006). "Protein Misfolding, Functional Amyloid, and Human Disease". *Annual Review of Biochemistry* 75.1, pp. 333–366. DOI: 10.1146/annurev.biochem.75.101304.123901.

Chong, P. L. and Choate, D. (Mar. 1989). "Calorimetric studies of the effects of cholesterol on the phase transition of C(18):C(10) phosphatidylcholine." *Biophysical journal* 55.3, pp. 551–556. DOI: 10.1016/S0006-3495(89)82848-6.

Cohen, S. I. A. et al. (2013). "Proliferation of amyloid-β42 aggregates occurs through a secondary nucleation mechanism". *Proceedings of the National Academy of Sciences* 110.24, pp. 9758–9763. DOI: 10.1073/pnas.1218402110.

Connelly, L. et al. (2012). "Effects of Point Substitutions on the Structure of Toxic Alzheimer's β-Amyloid Channels: Atomic Force Microscopy and Molecular Dynamics Simulations". *Biochemistry* 51.14, pp. 3031–3038. DOI: 10.1021/bi300257e.

Cowan, C. and Mudher, A. (2013). "Are Tau Aggregates Toxic or Protective in Tauopathies?" *Frontiers in Neurology* 4. DOI: 10.3389/fneur.2013.00114.

Crescenzi, O. et al. (2002). "Solution structure of the Alzheimer amyloid β-peptide (1–42) in an apolar microenvironment". *European Journal of Biochemistry* 269.22, pp. 5642–5648. DOI: 10.1046/j.1432-1033.2002.03271.x.

Cummings, J. L., Morstorf, T., and Zhong, K. (2014). "Alzheimer's disease drug-development pipeline: few candidates, frequent failures". *Alzheimer's Research & Therapy* 6.4, p. 37. DOI: 10.1186/alzrt269.

Dammann, P. et al. (2019). "Comment on 'Naked mole-rat mortality rates defy gompertzian laws by not increasing with age'". *eLife* 8, pp. 6–11. DOI: 10.7554/eLife.45415.

Davies, M. et al. (2022). "Elucidating lipid conformations in the ripple phase: Machine learning reveals four lipid populations". *Biophysical Journal*. DOI: 10.1016/j.bpj.2022.11.024.

Davies, S. and Guo, L. (2014). "Lipid peroxidation generates biologically active phospholipids including oxidatively N-modified phospholipids". *Chemistry and Physics of Lipids* 181, pp. 1–33. DOI: 10.1016/j.chemphyslip.2014.03.002.

Davis, C. H. and Berkowitz, M. L. (2010). "A molecular dynamics study of the early stages of amyloid-β(1–42) oligomerization: The role of lipid membranes". *Proteins: Structure, Function, and Bioinformatics* 78.11, pp. 2533–2545. DOI: 10.1002/prot.22763.

Davis, J. H., Clair, J. J., and Juhasz, J. (2009). "Phase Equilibria in DOPC/DPPC-d62/Cholesterol Mixtures". *Biophysical Journal* 96.2, pp. 521–539. DOI: 10.1016/j.bpj.2008.09.042.

De Waal, E. M. et al. (2013). "Elevated protein carbonylation and oxidative stress do not affect protein structure and function in the long-living naked-mole rat: A proteomic approach". *Biochemical and Biophysical Research Communications* 434.4, pp. 815–819. DOI: 10.1016/j.bbrc.2013.04.019.

Doktorova, M. et al. (2020). "Molecular Structure of Sphingomyelin in Fluid Phase Bilayers Determined by the Joint Analysis of Small-Angle Neutron and X-ray Scattering Data". *The Journal of Physical Chemistry B* 124.25, pp. 5186–5200. DOI: 10.1021/acs.jpcb.0c03389.

Drolle, E. et al. (2014). "Atomic force microscopy to study molecular mechanisms of amyloid fibril formation and toxicity in Alzheimer's disease". *Drug Metabolism Reviews* 46.2, pp. 207–223. DOI: 10.3109/03602532.2014.882354.

Eaton, P. and West, P. (2010). *Atomic force microscopy*. Oxford university press. ISBN: 9780199570454. DOI: 10.1093/acprof:oso/9780199570454.001.0001.

Edrey, Y. H., Medina, D. X., et al. (2013). "Amyloid beta and the longest-lived rodent: the naked mole-rat as a model for natural protection from Alzheimer's disease". *Neurobiology of Aging* 34.10, pp. 2352–2360. DOI: 10.1016/j.neurobiolaging.2013.03.032.

Edrey, Y. H., Oddo, S., et al. (2014). "Oxidative damage and amyloid-β metabolism in brain regions of the longest-lived rodents". *Journal of Neuroscience Research* 92.2, pp. 195–205. DOI: 10.1002/jnr.23320.

Engberg, O. et al. (2020). "Sphingomyelin Acyl Chains Influence the Formation of Sphingomyelin- and Cholesterol-Enriched Domains". *Biophysical Journal* 119.5, pp. 913–923. DOI: 10.1016/j.bpj.2020.07.014.

Epand, R. M. et al. (2015). "Membrane curvature modulation of protein activity determined by NMR". *Biochimica et Biophysica Acta (BBA) - Biomembranes* 1848.1, Part B, pp. 220–228. DOI: 10.1016/j.bbamem.2014.05.004.

Essmann, U. et al. (1995). "A smooth particle mesh Ewald method". *The Journal of Chemical Physics* 103.19, pp. 8577–8593. DOI: 10.1063/1.470117.

Fagan, A. M. et al. (2002). "Human and Murine ApoE Markedly Alters Aβ Metabolism before and after Plaque Formation in a Mouse Model of Alzheimer's Disease". *Neurobiology of Disease* 9.3, pp. 305–318. DOI: 10.1006/nbdi.2002.0483.

Fatafta, H. et al. (2020). "Role of Oxidized Gly25, Gly29, and Gly33 Residues on the Interactions of Aβ1–42 with Lipid Membranes". *ACS Chemical Neuroscience* 11.4, pp. 535–548. DOI: 10.1021/acschemneuro.9b00558.

Ferri, C. P. et al. (2005). "Global prevalence of dementia: a Delphi consensus study". *The Lancet* 366.9503, pp. 2112–2117. DOI: 10.1016/S0140-6736(05)67889-0.

Fischer, V., Siddiqi, A., and Yusufaly, Y. (1990). "Altered angioarchitecture in selected areas of brains with Alzheimer's disease". *Acta neuropathologica* 79.6, pp. 672–679. DOI: 10.1007/bf00294246.

Fowler, P. W. et al. (2016). "Roles of Interleaflet Coupling and Hydrophobic Mismatch in Lipid Membrane Phase-Separation Kinetics". *Journal of the American Chemical Society* 138.36, pp. 11633–11642. DOI: 10.1021/jacs.6b04880.

Frankel, D. et al. (2020). "Cholesterol-rich naked mole-rat brain lipid membranes are susceptible to amyloid beta-induced damage in vitro". *Aging* 12.21, pp. 22266–22290. DOI: 10.18632/aging.202138.

Frenkel, D. and Smit, B. (2002). Second Edition. San Diego: Academic Press, pp. 589–617. ISBN: 978-0-12-267351-1. DOI: 10.1016/B978-012267351-1/50032-8.

Gao, Q., Wu, G., and Lai, K. W. C. (2020). "Cholesterol Modulates the Formation of the Aβ Ion Channel in Lipid Bilayers". *Biochemistry* 59.8, pp. 992–998. DOI: 10.1021/acs.biochem.9b00968.

Girotti, A. W. and Korytowski, W. (2019). "Cholesterol Peroxidation as a Special Type of Lipid Oxidation in Photodynamic Systems". *Photochemistry and Photobiology* 95.1, pp. 73–82. DOI: 10.1111/php.12969.

Goate, A. (2006). "Segregation of a missense mutation in the amyloid β-protein precursor gene with familial Alzheimer's disease". *Journal of Alzheimer's Disease* 9.SUPPL. 3, pp. 341–347. DOI: 10.3233/jad-2006-9s338.

Goldstein, R. E. and Leibler, S. (1988). "Model for Lamellar Phases of Interacting Lipid Membranes". *Physical Review Letters* 61 (19), pp. 2213–2216. DOI: 10.1103/PhysRevLett.61.2213.

Gompertz, B. (1825). "On the nature of the function expressive of the law of human mortality, and on a new mode of determining the value of life contingencies." *Philosophical Transactions of the Royal Society of London* 115, pp. 513–583. DOI: 10.1098/rstl.1825.0026.

Gong, J.-S. et al. (2002). "Amyloid β-protein affects cholesterol metabolism in cultured neurons: Implications for pivotal role of cholesterol in the amyloid cascade". *Journal of Neuroscience Research* 70.3, pp. 438–446. DOI: 10.1002/jnr.10347.

Gosche, K. M. et al. (2002). "Hippocampal volume as an index of Alzheimer neuropathology". *Neurology* 58.10, pp. 1476–1482. DOI: 10.1212/WNL.58.10.1476.

Gowers, R. J. et al. (2016). "MDAnalysis: A Python Package for the Rapid Analysis of Molecular Dynamics Simulations". *Proceedings of the 15th Python in Science Conference*. Ed. by S. Benthall and S. Rostrup, pp. 98–105. DOI: 10.25080/Majora-629e541a-00e.

Greenough, M. A., Camakaris, J., and Bush, A. I. (2013). "Metal dyshomeostasis and oxidative stress in Alzheimer's disease". *Neurochemistry International* 62.5, pp. 540–555. DOI: 10.1016/j.neuint.2012.08.014.

Grimm, M. O. et al. (2016). "Oxidized Docosahexaenoic Acid Species and Lipid Peroxidation Products Increase Amyloidogenic Amyloid Precursor Protein Processing". *Neurodegenerative Diseases* 16.1-2, pp. 44–54. DOI: 10.1159/000440839.

Gunn, A. P. et al. (2016). "Amyloid-β Peptide Aβ3pE-42 Induces Lipid Peroxidation, Membrane Permeabilization, and Calcium Influx in Neurons". *Journal of Biological Chemistry* 291.12, pp. 6134–6145. DOI: 10.1074/jbc.M115.655183.

Gupta, R., Muralidhara, H. S., and Davis, H. T. (2001). "Structure and Phase Behavior of Phospholipid-Based Micelles in Nonaqueous Media". *Langmuir* 17.17, pp. 5176–5183. DOI: 10.1021/la0103721.

Habchi, J. et al. (2018). "Cholesterol catalyses Aβ42 aggregation through a heterogeneous nucleation pathway in the presence of lipid membranes". *Nature Chemistry* 10.6, pp. 673–683. DOI: 10.1038/s41557-018-0031-x.

Halford, R. W. and Russell, D. W. (2009). "Reduction of cholesterol synthesis in the mouse brain does not affect amyloid formation in Alzheimer's disease, but does extend lifespan". *Proceedings of the National Academy of Sciences*. DOI: 10.1073/pnas.0813349106.

Harayama, T. and Riezman, H. (2018). "Understanding the diversity of membrane lipid composition". *Nature Reviews Molecular Cell Biology* 19.5, pp. 281–296. DOI: 10.1038/nrm.2017.138.

Hardy, G. J., Nayak, R., and Zauscher, S. (2013). "Model cell membranes: Techniques to form complex biomimetic supported lipid bilayers via vesicle fusion". *Current Opinion in Colloid & Interface Science* 18.5, pp. 448–458. DOI: 10.1016/j.cocis.2013.06.004.

Hardy, J. A. and Higgins, G. A. (1992). "Alzheimer's Disease: The Amyloid Cascade Hypothesis". *Science* 256.5054, pp. 184–185. DOI: 10.1126/science.1566067.

Hardy, J. and Selkoe, D. J. (2002). "The Amyloid Hypothesis of Alzheimer's Disease: Progress and Problems on the Road to Therapeutics". *Science* 297.5580, pp. 353–356. DOI: 10.1126/science.1072994.

Hebert, L. E. et al. (2013). "Alzheimer disease in the United States (2010–2050) estimated using the 2010 census". *Neurology* 80.19, pp. 1778–1783. DOI: 10.1212/WNL.0b013e31828726f5.

Heimburg, T. (2000). "A Model for the Lipid Pretransition: Coupling of Ripple Formation with the Chain-Melting Transition". *Biophysical Journal* 78.3, pp. 1154–1165. DOI: 10.1016/S0006-3495(00)76673-2.

Hellstrand, E., Sparr, E., and Linse, S. (2010). "Retardation of Aβ Fibril Formation by Phospholipid Vesicles Depends on Membrane Phase Behavior". *Biophysical Journal* 98.10, pp. 2206–2214. DOI: 10.1016/j.bpj.2010.01.063.

Holmes, C. et al. (2008). "Long-term effects of Aβ42 immunisation in Alzheimer's disease: follow-up of a randomised, placebo-controlled phase I trial". *The Lancet* 372.9634, pp. 216–223. DOI: 10.1016/S0140-6736(08)61075-2.

Holmes, D. J. (2004). "Naturally Long-Lived Animal Models for the Study of Slow Aging and Longevity". *Annals of the New York Academy of Sciences* 1019.1, pp. 483–485. DOI: 10.1196/annals.1297.088.

Holtze, S. et al. (2018). "The microenvironment of naked mole-rat burrows in East Africa". *African Journal of Ecology* 56.2, pp. 279–289. DOI: 10.1111/aje.12448.

Hong, S. et al. (2014). "Soluble Aβ oligomers are rapidly sequestered from brain ISF in vivo and bind GM1 ganglioside on cellular membranes". *Neuron* 82.2, pp. 308–319. DOI: 10.1016/j.neuron.2014.02.027.

Hoppe, H. et al. (1992). "Surface Reconstruction from Unorganized Points". *SIGGRAPH Compututer Graphics* 26.2, pp. 71–78. DOI: 10.1145/142920.134011.

Huang, H.-Y. et al. (2002). "Effects of vitamin C and vitamin E on in vivo lipid peroxidation: results of a randomized controlled trial". *The American Journal of Clinical Nutrition* 76.3, pp. 549–555. DOI: 10.1093/ajcn/76.3.549.

Huang, J. et al. (2017). "CHARMM36m: an improved force field for folded and intrinsically disordered proteins". *Nature Methods* 14.1, pp. 71–73. DOI: 10.1038/nmeth.4067.

Huet, A. and Derreumaux, P. (2006). "Impact of the mutation A21G (Flemish Variant) on Alzheimer's β-amyloid dimers by molecular dynamics simulations". *Biophysical Journal* 91.10, pp. 3829–3840. DOI: 10.1529/biophysj.106.090993.

Hulbert, A. J., Faulks, S. C., and Buffenstein, R. (Oct. 2006). "Oxidation-Resistant Membrane Phospholipids Can Explain Longevity Differences Among the Longest-Living Rodents and Similarly-Sized Mice". *The Journals of Gerontology: Series A* 61.10, pp. 1009–1018. DOI: 10.1093/gerona/61.10.1009.

Inestrosa, N. C. et al. (2005). "Human-like rodent amyloid-β-peptide determines Alzheimer pathology in aged wild-type Octodon degu". *Neurobiology of Aging* 26.7, pp. 1023–1028. DOI: 10.1016/j.neurobiolaging.2004.09.016.

Israelachvili, J. N., Mitchell, D., and Ninham, B. W. (1977). "Theory of self-assembly of lipid bilayers and vesicles". *Biochimica et Biophysica Acta (BBA) - Biomembranes* 470.2, pp. 185–201. DOI: 10.1016/0005-2736(77)90099-2.

Ivanova, V. P. and Heimburg, T. (2001). "Histogram method to obtain heat capacities in lipid monolayers, curved bilayers, and membranes containing peptides". *Physical Review E* 63 (4), p. 041914. DOI: 10.1103/PhysRevE.63.041914.

Johnson, J. E. and Johnson, F. B. (May 2014). "Methionine Restriction Activates the Retrograde Response and Confers Both Stress Tolerance and Lifespan Extension to Yeast, Mouse and Human Cells". *PLOS ONE* 9.5, pp. 1–12. DOI: 10.1371/journal.pone.0097729.

Jorgensen, W. L. et al. (1983). "Comparison of simple potential functions for simulating liquid water". *The Journal of Chemical Physics* 79.2, pp. 926–935. DOI: 10.1063/1.445869.

Kamal, M. A. et al. (2011). "Theory of the asymmetric ripple phase in achiral lipid membranes". *Europhysics Letters* 95.4, p. 48004. DOI: 10.1209/0295-5075/95/48004.

Karran, E. and De Strooper, B. (2016). "The amyloid cascade hypothesis: are we poised for success or failure?" *Journal of Neurochemistry* 139.S2, pp. 237–252. DOI: 10.1111/jnc.13632.

Keller, J. N., Hanni, K. B., and Markesbery, W. R. (2000). "Possible involvement of proteasome inhibition in aging: Implications for oxidative stress". *Mechanisms of Ageing and Development* 113.1, pp. 61–70. DOI: 10.1016/S0047-6374(99)00101-3.

Kelley, A. S. et al. (2015). "The Burden of Health Care Costs for Patients With Dementia in the Last 5 Years of Life". *Annals of Internal Medicine* 163.10, p. 729. DOI: 10.7326/M15-0381.

Khakbaz, P. and Klauda, J. B. (2018). "Investigation of phase transitions of saturated phosphocholine lipid bilayers via molecular dynamics simulations". *Biochimica et*

Biophysica Acta (BBA) - Biomembranes 1860.8, pp. 1489–1501. DOI: 10.1016/j.bbamem.2018.04.014.

Knowles, T. P., Vendruscolo, M., and Dobson, C. M. (2014). "The amyloid state and its association with protein misfolding diseases". *Nature Reviews Molecular Cell Biology* 15.6, pp. 384–396. DOI: 10.1038/nrm3810.

Koppaka, V. and Axelsen, P. H. (2000). "Accelerated accumulation of amyloid β proteins on oxidatively damaged lipid membranes". *Biochemistry* 39.32, pp. 10011–10016. DOI: 10.1021/bi000619d.

Kotarek, J. and Moss, M. (2010). "Impact of phospholipid bilayer saturation on amyloid-β protein aggregation intermediate growth: A quartz crystal microbalance analysis". *Analytical Biochemistry* 399.1, pp. 30–38. DOI: 10.1016/j.ab.2009.12.016.

Kriegel, H.-P., Schubert, E., and Zimek, A. (2017). "The (black) art of runtime evaluation: Are we comparing algorithms or implementations?" *Knowledge and Information Systems.* 52.2, pp. 341–378. DOI: 10.1007/s10115-016-1004-2.

Krupa, P., Quoc Huy, P. D., and Li, M. S. (2019). "Properties of monomeric Aβ42 probed by different sampling methods and force fields: Role of energy components". *The Journal of Chemical Physics* 151.5, p. 055101. DOI: 10.1063/1.5093184.

Kumar-Singh, S. et al. (2005). "Dense-core plaques in Tg2576 and PSAPP mouse models of Alzheimer's disease are centered on vessel walls". *American Journal of Pathology* 167.2, pp. 527–543. DOI: 10.1016/S0002-9440(10)62995-1.

Kunjathoor, V. V. et al. (2004). "β-Amyloid promotes accumulation of lipid peroxides by inhibiting CD36-mediated clearance of oxidized lipoproteins". *Journal of Neuroinflammation* 1, pp. 1–12. DOI: 10.1186/1742-2094-1-23.

Lam, A. R. et al. (2008). "Effects of the arctic (E22→G) mutation on amyloid β-protein folding: Discrete molecular dynamics study". *Journal of the American Chemical Society* 130.51, pp. 17413–17422. DOI: 10.1021/ja804984h.

Lee, B. P., Pilling, L. C., et al. (2016). "Changes in the expression of splicing factor transcripts and variations in alternative splicing are associated with lifespan in mice and humans". *Aging Cell* 15.5, pp. 903–913. DOI: 10.1111/acel.12499.

Lee, B. P., Smith, M., et al. (2020). "Negligible senescence in naked mole rats may be a consequence of well-maintained splicing regulation". *GeroScience*, pp. 633–651. DOI: 10.1007/s11357-019-00150-7.

Lee, J., Kim, Y. H., et al. (2017). "Amyloid β Ion Channels in a Membrane Comprising Brain Total Lipid Extracts". *ACS Chemical Neuroscience* 8.6, pp. 1348–1357. DOI: 10.1021/acschemneuro.7b00006.

Lee, J., Cheng, X., et al. (2016). "CHARMM-GUI Input Generator for NAMD, GROMACS, AMBER, OpenMM, and CHARMM/OpenMM Simulations Using the CHARMM36 Additive Force Field". *Journal of Chemical Theory and Computation* 12.1, pp. 405–413. DOI: 10.1021/acs.jctc.5b00935.

Lenz, O. and Schmid, F. (2007). "Structure of Symmetric and Asymmetric "Ripple" Phases in Lipid Bilayers". *Physical Review Letters* 98 (5), p. 058104. DOI: 10.1103/PhysRevLett.98.058104.

Leoni, V., Solomon, A., and Kivipelto, M. (July 2010). "Links between ApoE, brain cholesterol metabolism, tau and amyloid β-peptide in patients with cognitive impairment". *Biochemical Society Transactions* 38.4, pp. 1021–1025. DOI: 10.1042/BST0381021.

Lewis, K. N., Andziak, B., et al. (2013). "The Naked Mole-Rat Response to Oxidative Stress: Just Deal with It". *Antioxidants & Redox Signaling* 19.12, pp. 1388–1399. DOI: 10.1089/ars.2012.4911.

Lewis, K. N., Rubinstein, N. D., and Buffenstein, R. (2018). "A window into extreme longevity; the circulating metabolomic signature of the naked mole-rat, a mammal that shows negligible senescence". *GeroScience* 40.2, pp. 105–121. DOI: 10.1007/s11357-018-0014-2.

Li, J. K., Sullan, R. M. A., and Zou, S. (2011). "Atomic Force Microscopy Force Mapping in the Study of Supported Lipid Bilayers". *Langmuir* 27.4, pp. 1308–1313. DOI: 10.1021/la103927a.

Lindberg, D. J. et al. (2017). "Lipid membranes catalyse the fibril formation of the amyloid-β (1–42) peptide through lipid-fibril interactions that reinforce secondary pathways". *Biochimica et Biophysica Acta (BBA) - Biomembranes* 1859.10, pp. 1921–1929. DOI: 10.1016/j.bbamem.2017.05.012.

Lippa, C. F. et al. (1996). "Familial and sporadic Alzheimer's disease: Neuropathology cannot exclude a final common pathway". *Neurology* 46.2, pp. 406–412. DOI: 10.1212/WNL.46.2.406.

Liu, J., Tian, M., and Shen, L. (2020). "Surface effects on the degree of twist in amyloid fibril structures". *Chemical Communications* 56 (21), pp. 3147–3150. DOI: 10.1039/C9CC10079B.

Lubensky, T. C. and MacKintosh, F. C. (1993). "Theory of "Ripple" Phases of Lipid Bilayers". *Physical Review Letters* 71 (10), pp. 1565–1568. DOI: 10.1103/PhysRevLett.71.1565.

Lührs, T. et al. (2005). "3D structure of Alzheimer's amyloid-β(1-42) fibrils". *Proceedings of the National Academy of Sciences* 102.48, pp. 17342–17347. DOI: 10.1073/pnas.0506723102.

Maaten, L. van der and Hinton, G. (2008). "Visualizing Data using t-SNE". *Journal of Machine Learning Research* 9.86, pp. 2579–2605.

Magalhães, J. P. de, Costa, J., and Church, G. M. (2007). "An Analysis of the Relationship Between Metabolism, Developmental Schedules, and Longevity Using Phylogenetic Independent Contrasts". *The Journals of Gerontology: Series A* 62.2, pp. 149–160. DOI: 10.1093/gerona/62.2.149.

Malmos, K. G. et al. (2017). "ThT 101: a primer on the use of thioflavin T to investigate amyloid formation". *Amyloid* 24.1, pp. 1–16. DOI: 10.1080/13506129.2017.1304905.

Mari, S. A. et al. (2018). "Reversible Cation-Selective Attachment and Self-Assembly of Human Tau on Supported Brain Lipid Membranes". *Nano Letters* 18.5, pp. 3271–3281. DOI: 10.1021/acs.nanolett.8b01085.

Mayeux, R. and Stern, Y. (2012). "Epidemiology of Alzheimer Disease". *Cold Spring Harbor Perspectives in Medicine* 2.8, a006239–a006239. DOI: 10.1101/cshperspect.a006239.

Milhiet, P.-E. et al. (2002). "AFM Detection of GPI Protein Insertion into DOPC/DPPC Model Membranes". *Single Molecules* 3.2-3, pp. 135–140. DOI: 10.1002/1438-5171(200206)3:2/3<135::AID-SIMO135>3.0.CO;2-O.

Mitchell, T. W., Buffenstein, R., and Hulbert, A. (2007). "Membrane phospholipid composition may contribute to exceptional longevity of the naked mole-rat (Heterocephalus glaber): A comparative study using shotgun lipidomics". *Experimental Gerontology* 42.11, pp. 1053–1062. DOI: 10.1016/j.exger.2007.09.004.

Möller, H.-J. and Graeber, M. B. (1998). "The case described by Alois Alzheimer in 1911". *European Archives of Psychiatry and Clinical Neuroscience* 248.3, pp. 111–122. DOI: 10.1007/s004060050027.

Mrdenovic, D. et al. (2019). "Size-Dependent Interaction of Amyloid β Oligomers with Brain Total Lipid Extract Bilayer - Fibrillation Versus Membrane Destruction". *Langmuir*. DOI: 10.1021/acs.langmuir.9b01645.

Munro, D. et al. (2019). "The exceptional longevity of the naked mole-rat may be explained by mitochondrial antioxidant defenses". *Aging Cell* 18.3, e12916. DOI: 10.1111/acel.12916.

Munro, S. (2003). "Lipid Rafts: Elusive or Illusive?" *Cell* 115.4, pp. 377–388. DOI: 10.1016/S0092-8674(03)00882-1.

Nagle, J. F. (1980). "Theory of the Main Lipid Bilayer Phase Transition". *Annual Review of Physical Chemistry* 31.1, pp. 157–196. DOI: 10.1146/annurev.pc.31.100180.001105.

Nunomura, A. et al. (2001). "Oxidative Damage Is the Earliest Event in Alzheimer Disease". *Journal of Neuropathology & Experimental Neurology* 60.8, pp. 759–767. DOI: 10.1093/jnen/60.8.759.

O'Brien, R. J. and Wong, P. C. (2011). "Amyloid Precursor Protein Processing and Alzheimer's Disease". *Annual Review of Neuroscience* 34.1, pp. 185–204. DOI: 10.1146/annurev-neuro-061010-113613.

Oddo, S. et al. (2003). "Triple-transgenic model of Alzheimer's Disease with plaques and tangles: Intracellular Aβ and synaptic dysfunction". *Neuron* 39.3, pp. 409–421. DOI: 10.1016/S0896-6273(03)00434-3.

Oliveira, M. C. et al. (2021). "Lipid Oxidation: Role of Membrane Phase-Separated Domains". *Journal of Chemical Information and Modeling* 61.6, pp. 2857–2868. DOI: 10.1021/acs.jcim.1c00104.

Orr, M. E. et al. (2015). "Sustained high levels of neuroprotective, high molecular weight, phosphorylated tau in the longest-lived rodent". *Neurobiology of Aging* 36.3, pp. 1496–1504. DOI: 10.1016/j.neurobiolaging.2014.12.004.

Owen, M. C. et al. (2018). "Physiologically-relevant levels of sphingomyelin, but not GM1, induces a β-sheet-rich structure in the amyloid-β(1-42) monomer". *Biochimica et Biophysica Acta (BBA) - Biomembranes* 1860.9, pp. 1709–1720. DOI: 10.1016/j.bbamem.2018.03.026.

Pannuzzo, M. et al. (2013). "Analytical model and multiscale simulations of Aβ peptide aggregation in lipid membranes: Towards a unifying description of conformational transitions, oligomerization and membrane damage". *Physical Chemistry Chemical Physics* 15.23, pp. 8940–8951. DOI: 10.1039/c3cp44539a.

Parrinello, M. and Rahman, A. (1981). "Polymorphic transitions in single crystals: A new molecular dynamics method". *Journal of Applied Physics* 52.12, pp. 7182–7190. DOI: 10.1063/1.328693.

Pedregosa, F. et al. (2011). "Scikit-learn: Machine learning in Python". *Journal of Machine Learning Research* 12, pp. 2825–2830.

Pencer, J. et al. (2005). "Bilayer thickness and thermal response of dimyristoylphosphatidylcholine unilamellar vesicles containing cholesterol, ergosterol and lanosterol: A small-angle neutron scattering study". *Biochimica et Biophysica Acta (BBA) - Biomembranes* 1720.1, pp. 84–91. DOI: 10.1016/j.bbamem.2005.10.017.

Pérez, V. I. et al. (2009). "Protein stability and resistance to oxidative stress are determinants of longevity in the longest-living rodent, the naked mole-rat". *Proceedings of the National Academy of Sciences of the United States of America* 106.9, pp. 3059–3064. DOI: 10.1073/pnas.0809620106.

Piggot, T. J., Allison, J. R., et al. (2017). "On the Calculation of Acyl Chain Order Parameters from Lipid Simulations". *Journal of Chemical Theory and Computation* 13.11, pp. 5683–5696. DOI: 10.1021/acs.jctc.7b00643.

Piggot, T. J., Piñeiro, Á., and Khalid, S. (2012). "Molecular Dynamics Simulations of Phosphatidylcholine Membranes: A Comparative Force Field Study". *Journal of Chemical Theory and Computation* 8.11, pp. 4593–4609. DOI: 10.1021/ct3003157.

Pobandt, T. and Knecht, V. (2014). "Free energy of lipid bilayer defects affected by Alzheimer's disease-associated amyloid-β42 monomers". *Journal of Physical Chemistry B* 118.13, pp. 3507–3516. DOI: 10.1021/jp410477x.

Powell, J. L. (2010). "The power of global aging". *Ageing International* 35.1, pp. 1–14. DOI: 10.1007/s12126-010-9051-6.

Przedborski, S., Vila, M., and Jackson-Lewis, V. (2003). "Neurodegeneration: What is it and where are we?" *Journal of Clinical Investigation* 111.1, pp. 3–10. DOI: 10.1172/JCI200317522.

Puglielli, L., Tanzi, R. E., and Kovacs, D. M. (2003). "Alzheimer's disease: The cholesterol connection". *Nature Neuroscience* 6.4, pp. 345–351. DOI: 10.1038/nn0403-345.

Qiang, W., Yau, W.-M., and Schulte, J. (2015). "Fibrillation of β amyloid peptides in the presence of phospholipid bilayers and the consequent membrane disruption". *Biochimica et Biophysica Acta (BBA) - Biomembranes* 1848.1, Part B, pp. 266–276. DOI: 10.1016/j.bbamem.2014.04.011.

Raffy, S. and Teissié, J. (Apr. 1999). "Control of Lipid Membrane Stability by Cholesterol Content". *Biophysical Journal* 76.4, pp. 2072–2080. DOI: 10.1016/S0006-3495(99)77363-7.

Ramos, A. P., Bouwstra, J. A., and Lafleur, M. (2020). "Very Long Chain Lipids Favor the Formation of a Homogeneous Phase in Stratum Corneum Model Membranes". *Langmuir* 36.46, pp. 13899–13907. DOI: 10.1021/acs.langmuir.0c02305.

Relini, A., Marano, N., and Gliozzi, A. (2014). "Probing the interplay between amyloidogenic proteins and membranes using lipid monolayers and bilayers". *Advances in Colloid and Interface Science* 207.1, pp. 81–92. DOI: 10.1016/j.cis.2013.10.015.

Riske, K. A. et al. (2009). "Lipid bilayer pre-transition as the beginning of the melting process". *Biochimica et Biophysica Acta (BBA) - Biomembranes* 1788.5, pp. 954–963. DOI: 10.1016/j.bbamem.2009.01.007.

Roychaudhuri, R. et al. (2015). "Role of Species-Specific Primary Structure Differences in Aβ42 Assembly and Neurotoxicity". *ACS Chemical Neuroscience* 6.12, pp. 1941–1955. DOI: 10.1021/acschemneuro.5b00180.

Ruby, J. G., Smith, M., and Buffenstein, R. (2019). "'Naked mole-rat mortality rates defy gompertzian laws by not increasing with age'". *eLife* 8, pp. 1–18. DOI: 10.7554/eLife.47047.

Sanchez-Roman, I. et al. (2012). "Effects of aging and methionine restriction applied at old age on ROS generation and oxidative damage in rat liver mitochondria". *Biogerontology* 13.4, pp. 399–411. DOI: 10.1007/s10522-012-9384-5.

Sanguanini, M. et al. (2020). "Complexity in Lipid Membrane Composition Induces Resilience to Aβ42 Aggregation". *ACS Chemical Neuroscience* 11.9, pp. 1347–1352. DOI: 10.1021/acschemneuro.0c00101.

Schmidt, M. L. and Davis, J. H. (2017). "Liquid Disordered–Liquid Ordered Phase Coexistence in Lipid/Cholesterol Mixtures: A Deuterium 2D NMR Exchange Study". *Langmuir* 33.8, pp. 1881–1890. DOI: 10.1021/acs.langmuir.6b02834.

Schneider, J. et al. (2000). "Atomic Force Microscope Image Contrast Mechanisms on Supported Lipid Bilayers". *Biophysical Journal* 79.2, pp. 1107–1118. DOI: 10.1016/S0006-3495(00)76364-8.

Schubert, E. et al. (2017). "DBSCAN Revisited, Revisited: Why and How You Should (Still) Use DBSCAN". *ACM Transactions Database Systems* 42.3. DOI: 10.1145/3068335.

Scott, D. W. (1992). "Kernel Density Estimators". *Multivariate Density Estimation*. John Wiley & Sons, Ltd. Chap. 6, pp. 125–193. ISBN: 9780470316849. DOI: 10.1002/9780470316849.ch6.

Selkoe, D. J. (1991). "The molecular pathology of Alzheimer's disease". *Neuron* 6.4, pp. 487–498. DOI: 10.1016/0896-6273(91)90052-2.

Sherman, P. W. and Jarvis, J. U. (2002). "Extraordinary life spans of naked mole-rats (Heterocephalus glaber)". *Journal of Zoology* 258.3, pp. 307–311. DOI: 10.1017/S0952836902001437.

Sivanesam, K. and Andersen, N. (2019). "Pre-structured hydrophobic peptide β-strands: A universal amyloid trap?" *Archives of Biochemistry and Biophysics* 664, pp. 51–61. DOI: 10.1016/j.abb.2019.01.032.

Small, S. A. and Duff, K. (2008). "Linking Aβ and Tau in Late-Onset Alzheimer's Disease: A Dual Pathway Hypothesis". *Neuron* 60.4, pp. 534–542. DOI: 10.1016/j.neuron.2008.11.007.

Smith, P., Owen, D. M., et al. (2021). "Asymmetric glycerophospholipids impart distinctive biophysical properties to lipid bilayers". *Biophysical Journal* 120.9, pp. 1746–1754. DOI: 10.1016/j.bpj.2021.02.046.

Smith, P., Quinn, P. J., and Lorenz, C. D. (2020). "Two Coexisting Membrane Structures Are Defined by Lateral and Transbilayer Interactions between Sphingomyelin and Cholesterol". *Langmuir* 36.33, pp. 9786–9799. DOI: 10.1021/acs.langmuir.0c01237.

Smith, S. O. et al. (1994). "Rotational Resonance NMR Determination of Intra- and Intermolecular Distance Constraints in Dipalmitoylphosphatidylcholine Bilayers". *Biochemistry* 33.20, pp. 6327–6333. DOI: 10.1021/bi00186a036.

Smondyrev, A. M. and Berkowitz, M. L. (1999). "Structure of Dipalmitoylphosphatidylcholine/Cholesterol Bilayer at Low and High Cholesterol Concentrations: Molecular Dynamics Simulation". *Biophysical Journal* 77.4, pp. 2075–2089. DOI: 10.1016/S0006-3495(99)77049-9.

Sodt, A. J., Pastor, R. W., and Lyman, E. (2015). "Hexagonal Substructure and Hydrogen Bonding in Liquid-Ordered Phases Containing Palmitoyl Sphingomyelin". *Biophysical Journal* 109.5, pp. 948–955. DOI: 10.1016/j.bpj.2015.07.036.

Stone, M. B. et al. (2017). "Protein sorting by lipid phase-like domains supports emergent signaling function in B lymphocyte plasma membranes". *eLife* 6, e19891. DOI: 10.7554/eLife.19891.

Sukhomlinov, S. V. and Müser, M. H. (2020). "A mixed radial, angular, three-body distribution function as a tool for local structure characterization: Application to

single-component structures". *The Journal of Chemical Physics* 152.19, p. 194502. DOI: 10.1063/5.0007964.

Sukhomlinov, S. V. and Müser, M. H. (2021). "Stress Anisotropy Severely Affects Zinc Phosphate Network Formation". *Tribology Letters* 69.3, p. 89. DOI: 10.1007/s11249-021-01462-6.

Sun, L. and Böckmann, R. A. (2018). "Membrane phase transition during heating and cooling: molecular insight into reversible melting". *European Biophysics Journal* 47.2, pp. 151–164. DOI: 10.1007/s00249-017-1237-3.

Sun, W. J. et al. (1996). "Structure of the ripple phase in lecithin bilayers". *Proceedings of the National Academy of Sciences* 93.14, pp. 7008–7012. DOI: 10.1073/pnas.93.14.7008.

Swerdlow, R. H., Burns, J. M., and Khan, S. M. (2014). "The Alzheimer's disease mitochondrial cascade hypothesis: Progress and perspectives". *Biochimica et Biophysica Acta (BBA) - Molecular Basis of Disease* 1842.8, pp. 1219–1231. DOI: 10.1016/j.bbadis.2013.09.010.

Swerdlow, R. H. and Khan, S. M. (2004). "A "mitochondrial cascade hypothesis" for sporadic Alzheimer's disease". *Medical Hypotheses* 63.1, pp. 8–20. DOI: 10.1016/j.mehy.2003.12.045.

Tardieu, A., Luzzati, V., and Reman, F. (1973). "Structure and polymorphism of the hydrocarbon chains of lipids: A study of lecithin-water phases". *Journal of Molecular Biology* 75.4, pp. 711–733. DOI: 10.1016/0022-2836(73)90303-3.

Todd, S. et al. (2013). "Survival in dementia and predictors of mortality: A review". *International Journal of Geriatric Psychiatry* 28.11, pp. 1109–1124. DOI: 10.1002/gps.3946.

Torre, J. C. de la (2004). "Is Alzheimer's disease a neurodegenerative or a vascular disorder? Data, dogma, and dialectics". *Lancet Neurology* 3.3, pp. 184–190. DOI: 10.1016/S1474-4422(04)00683-0.

Torre, J. C. de la (2008). "Pathophysiology of Neuronal Energy Crisis in Alzheimer's Disease". *Neurodegenerative Diseases* 5.3-4, pp. 126–132. DOI: 10.1159/000113681.

Truong, P. M. et al. (2014). "Effect of Taiwan mutation (D7H) on structures of amyloid-β peptides: Replica exchange molecular dynamics study". *Journal of Physical Chemistry B* 118.30, pp. 8972–8981. DOI: 10.1021/jp503652s.

Vahed, M. et al. (2019). "The initial stage of structural transformation of Aβ42 peptides from the human and mole rat in the presence of Fe2+ and Fe3+: Related to

Alzheimer's disease". *Computational Biology and Chemistry* 83, p. 107128. DOI: 10.1016/j.compbiolchem.2019.107128.

van Meer, G., Voelker, D. R., and Feigenson, G. W. (2008). "Membrane lipids: Where they are and how they behave". *Nature Reviews Molecular Cell Biology* 9.2, pp. 112–124. DOI: 10.1038/nrm2330.

Varma, V. R. et al. (2018). "Brain and blood metabolite signatures of pathology and progression in Alzheimer disease: A targeted metabolomics study". *PLOS Medicine* 15.1, pp. 1–31. DOI: 10.1371/journal.pmed.1002482.

Venable, R. M. et al. (July 2014). "CHARMM All-Atom Additive Force Field for Sphingomyelin: Elucidation of Hydrogen Bonding and of Positive Curvature". *Biophysical Journal* 107.1, pp. 134–145. DOI: 10.1016/j.bpj.2014.05.034.

Villemagne, V. L. et al. (2011). "Longitudinal assessment of Aβ and cognition in aging and Alzheimer disease". *Annals of Neurology* 69.1, pp. 181–192. DOI: 10.1002/ana.22248.

Vries, A. H. de et al. (2005). "Molecular structure of the lecithin ripple phase". *Proceedings of the National Academy of Sciences* 102.15, pp. 5392–5396. DOI: 10.1073/pnas.0408249102.

Walsh, D. M. and Selkoe, D. J. (2007). "Aβ oligomers - A decade of discovery". *Journal of Neurochemistry* 101.5, pp. 1172–1184. DOI: 10.1111/j.1471-4159.2006.04426.x.

Walt, S. van der et al. (2014). "scikit-image: image processing in Python". *PeerJ* 2, e453. DOI: 10.7717/peerj.453.

Walter, V., Ruscher, C., Benzerara, O., et al. (2020). "A machine learning study of the two states model for lipid bilayer phase transitions". *Physical Chemistry Chemical Physics* 22 (34), pp. 19147–19154. DOI: 10.1039/D0CP02058C.

Walter, V., Ruscher, C., Gola, A., et al. (2021). "Ripple-like instability in the simulated gel phase of finite size phosphocholine bilayers". *Biochimica et Biophysica Acta (BBA) - Biomembranes* 1863.11, p. 183714. DOI: 10.1016/j.bbamem.2021.183714.

Wang, Z. et al. (2004). "Image quality assessment: from error visibility to structural similarity". *IEEE Transactions on Image Processing* 13.4, pp. 600–612. DOI: 10.1109/TIP.2003.819861.

Wassall, S. R. and Stillwell, W. (2009). "Polyunsaturated fatty acid–cholesterol interactions: Domain formation in membranes". *Biochimica et Biophysica Acta (BBA) - Biomembranes* 1788.1, pp. 24–32. DOI: 10.1016/j.bbamem.2008.10.011.

Watanabe-Nakayama, T. et al. (2020). "High-Speed Atomic Force Microscopy Reveals the Structural Dynamics of the Amyloid-β and Amylin Aggregation Pathways". *International Journal of Molecular Sciences* 21.12. DOI: 10.3390/ijms21124287.

Weiner, M. D. and Feigenson, G. W. (2019). "Molecular Dynamics Simulations Reveal Leaflet Coupling in Compositionally Asymmetric Phase-Separated Lipid Membranes". *The Journal of Physical Chemistry B* 123.18, pp. 3968–3975. DOI: 10.1021/acs.jpcb.9b03488.

Wolfe, K. J. and Cyr, D. M. (2011). "Amyloid in neurodegenerative diseases: Friend or foe?" *Seminars in Cell & Developmental Biology* 22.5, pp. 476–481. DOI: 10.1016/j.semcdb.2011.03.011.

Yuyama, K. and Yanagisawa, K. (2010). "Sphingomyelin accumulation provides a favorable milieu for GM1 ganglioside-induced assembly of amyloid β-protein". *Neuroscience Letters* 481.3, pp. 168–172. DOI: 10.1016/j.neulet.2010.06.080.

Zhang, Y. J. et al. (2012). "Intra-membrane oligomerization and extra-membrane oligomerization of amyloid-β peptide are competing processes as a result of distinct patterns of motif interplay". *Journal of Biological Chemistry* 287.1, pp. 748–756. DOI: 10.1074/jbc.M111.281295.

Zhu, L. et al. (2015). "Phospholipid dysregulation contributes to ApoE4-associated cognitive deficits in Alzheimer's disease pathogenesis". *Proceedings of the National Academy of Sciences*. DOI: 10.1073/pnas.1510011112.

Ziolek, R. M. et al. (2021). "Unsupervised Learning Unravels the Structure of Four-Arm and Linear Block Copolymer Micelles". *Macromolecules* 54.8, pp. 3755–3768. DOI: 10.1021/acs.macromol.0c02523.

Appendix A.

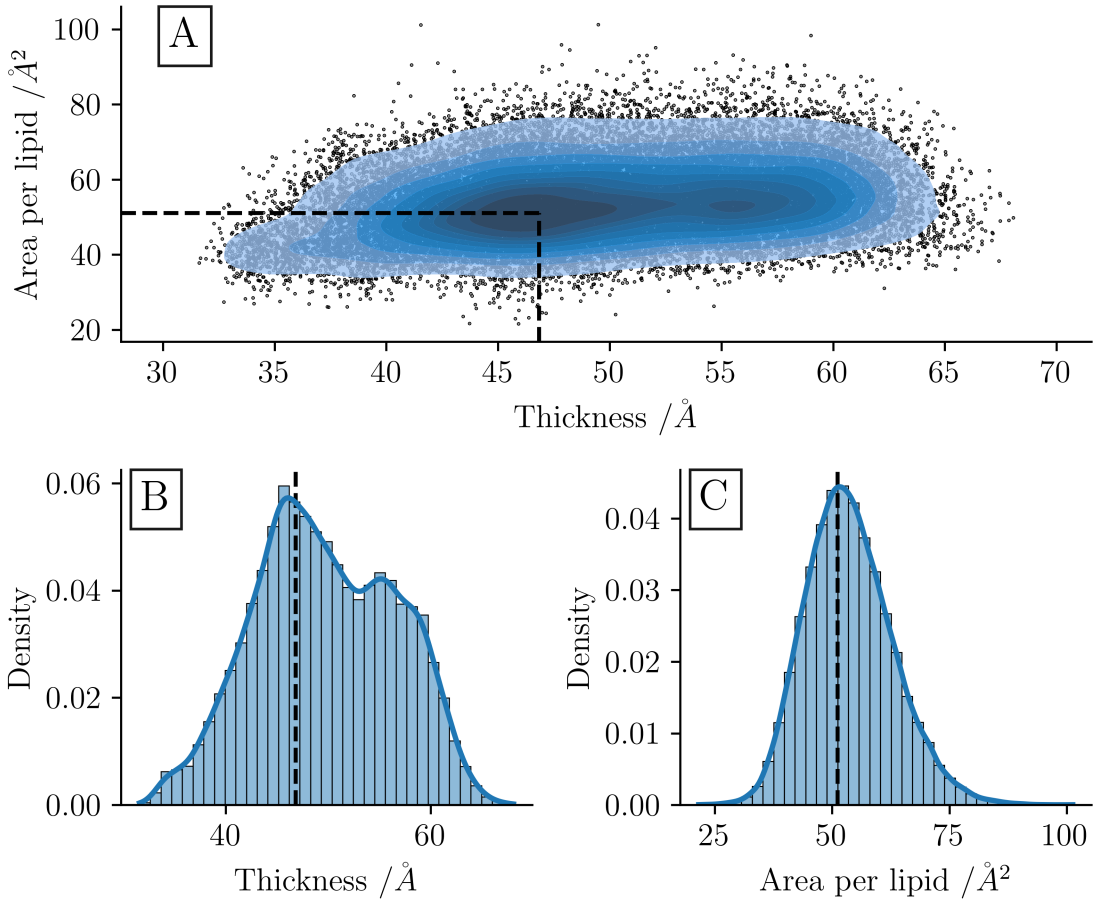

Figure A.1: Lipid coupled thickness and area per lipid for the SM24 systems. Scatter plot of bilayer thickness and area per lipid (A) and individual histograms of the thickness (B) and area per lipid (C) showing the bimodal thickness and unimodal area per lipid. The black dashed lines indicate the most probabable value in each case.

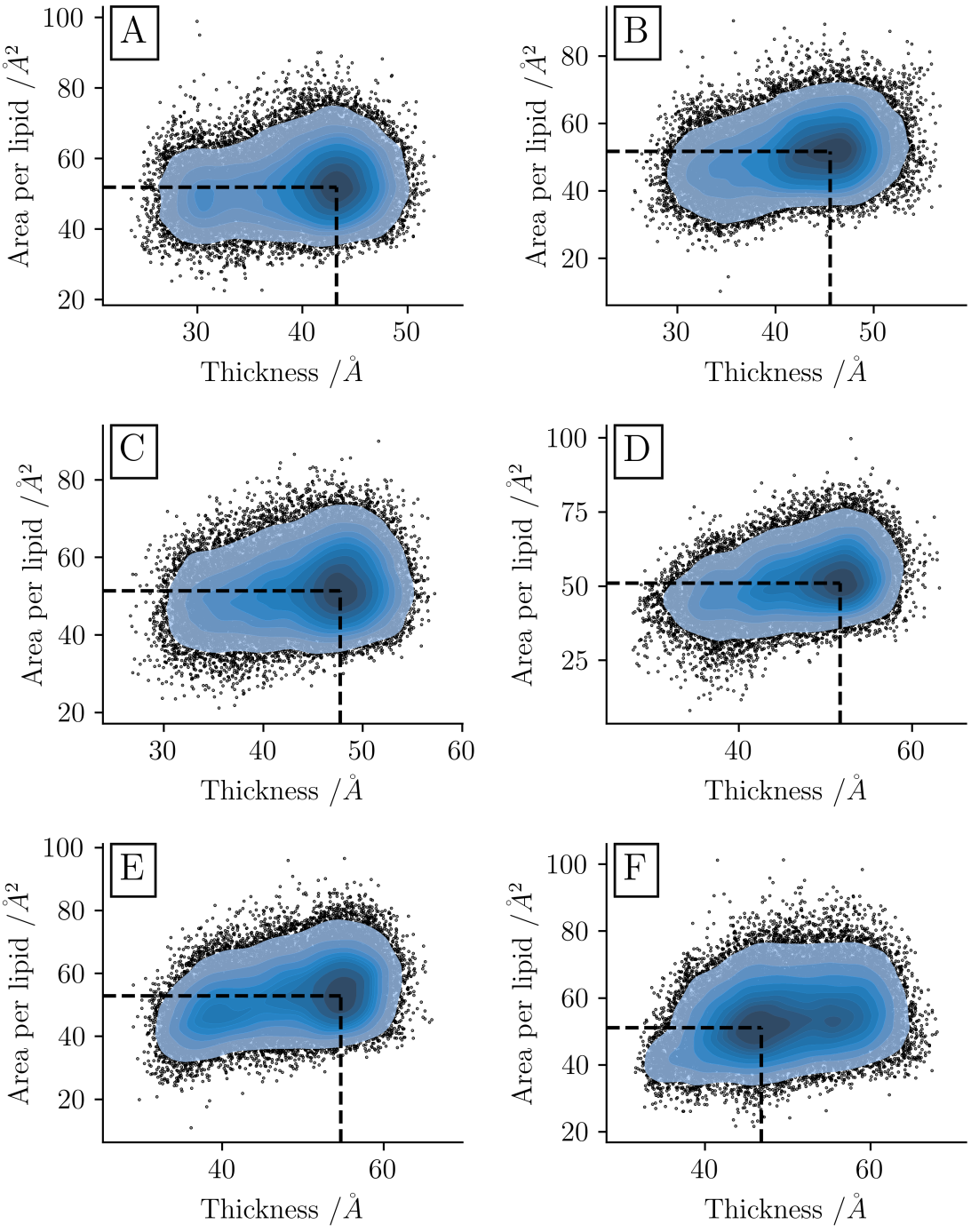

Figure A.2: Scatter plot of thickness vs area per lipid for each acyl-chain length sphingomyelin. 14 (A), 16 (B), 18 (C), 20 (D), 22 (E) and 24 (F). Bimodal distributions can be seen in SM14, SM22 and SM24 where the tail asymmetry is higher.